UNIVERSITY OF SOUTHAMPTON

A spectroscopic analysis of three cataclysmic variable stars

Eduardo Unda-Sanzana

Submitted for the degree of Doctor of Philosophy

DEPARTMENT OF PHYSICS AND ASTRONOMY
FACULTY OF SCIENCE

February 16, 2005

UNIVERSITY OF SOUTHAMPTON

ABSTRACT

FACULTY OF SCIENCE
DEPARTMENT OF PHYSICS AND ASTRONOMY

Doctor of Philosophy

A spectroscopic analysis of three cataclysmic variable stars

by Eduardo Unda-Sanzana

Cataclysmic variable stars (CVs) are binary systems in which matter is transferred from a low mass star to a white dwarf via an accretion disc. My thesis is a spectroscopic study of three of these objects: U Gem, GD 552 and GY Cnc.

I present high-resolution optical spectra of U Gem taken during quiescence. For U Gem, the radial velocity semi-amplitude of the white dwarf, K_1, is accurately known thanks to a direct observation by Long et al. (1999). I find that even with these data the optical measurements are seriously distorted compared to the known value, which is not recovered to better than $\sim$ 20%. Doppler tomograms show emission at low velocity, close to the centre of mass, and a transient and sharp absorption feature is seen in the Balmer lines close to eclipse. I suggest that stellar prominences may explain part of these features. I study two features detected in He II4686.75 Å. They seem to be produced in the bright spot. The narrower feature has a velocity close to that of the accretion disc in the impact region. I present evidence of weak spiral structure, which may support explanations for "spiral shocks" based upon 3-body effects. I apply a method of isophote fitting to search for evidence of stream-disc overflow, but fail to uncover any. I detect evidence of irradiation of the mass donor with shielding by the disc: I estimate an H/R ratio between 0.15 and 0.20.

For GD 552 I present spectroscopy taken with the aim of detecting emission from the mass donor. I fail to do so at a level which allows me to rule out the presence of a near-main-sequence star donor. Given GD 552's orbital period of 103 minutes, this suggests instead that it may be a system that has evolved through the $\sim$ 80-minute orbital period minimum of CVs and now has a brown dwarf mass donor.

Finally, I give a first look at high-resolution data for GY Cnc whose dynamical parameters make it a near-perfect twin of U Gem. I find several surprising features: the bright spot is completely absent from the Balmer lines, although visible in other lines; emission from the secondary star seems to arise from the whole of its Roche lobe; and low velocity emission is detected near the centre of mass as in U Gem. I argue that GY Cnc provides further evidence of the presence of prominence-like structures on CVs.

Contents

List of Figures

List of Tables

Acknowledgements

I acknowledge the support given by PPARC (UK) and Fundación Andes (Chile) under the program Gemini PPARC-Andes during my research. Key support was also given by the Astronomy Group at the Universidad de Concepción (Chile); I am specially grateful towards Ronald Mennickent and Rodrigo Mundaca (RASTRO) for their kind help. NASA's ADS Bibliographic Services, the Hartley Library collections and the Starlink resources are great tools who endured nearly abusive use during my research. Sincere thanks go to Simon Harris and Mike Hill for all their help.

While I hold myself responsible for all the imprecisions this work certainly includes, I acknowledge the patience of all the people who struggled to keep them at a minimum, against my tenacious efforts as to the contrary. At different stages Luisa Morales-Rueda, Rachel North and Danny Steeghs gave invaluable help and ideas. Tom Marsh, my supervisor, deserves special attention in this section. During the long time it took for my thesis to be ready, he was patient and understanding beyond all measure. Much of what is of value in this work is due to his guidance.

My officemates, Luisa, Rachel, Silas and Nick were remarkably good sufferers of the ways of a person who had a hard time adjusting to the English ways but whom, with time, deeply learnt to appreciate and share most of them. In this process Luisa honoured me with a friendship for which I feel happy and proud. I am also indebted to some people who made my time en England something worth to remember and to miss, in difficult times replenishing of sense the whole experience. Raakhi Sunak, David Anthony, Pete Fisher, Andrew Harmer and Sofía Araujo are some of them.

Last in this list but first in my heart, I want to acknowledge the loving support of Soledad Martínez Labrín, whom, as always, in many ways coauthored this work. I am certain that without her there would be no stars to write about.

Chapter 1

The CV scenario

1.1 Why observe CVs?

Cataclysmic variable stars (CVs) are systems where accretion processes have observable effects in time scales of just days or weeks, their light being believed to be produced mainly by that mechanism. In addition to being interesting objects in themselves, the importance of studying CVs lies largely in the manageability of the time scales of these accretion processes in terms of human time scales. We know that accretion is at the heart of many phenomena in the Universe (e.g. active galactic nucleii) but the very long time scales involved make it impossible for us to study directly how accretion drives these phenomena. Enter CVs. We can study the time evolution of CVs at many wavelengths, and thus we can test our theories about accretion (see, for instance, Warner 1995).

Although this method of studying accretion can in turn provide a better understanding of many other objects, this requires a good knowledge about the CVs' basic parameters, for these are the basis used to support or rule out more complex models and, therefore, theories. In this sense, the information we can gather from a single system is very limited by instrumental and natural constraints. Instead, our knowledge about CVs is mainly statistical, and thus both quality and quantity of results are important. My thesis aims to add to both aspects of research on CVs.

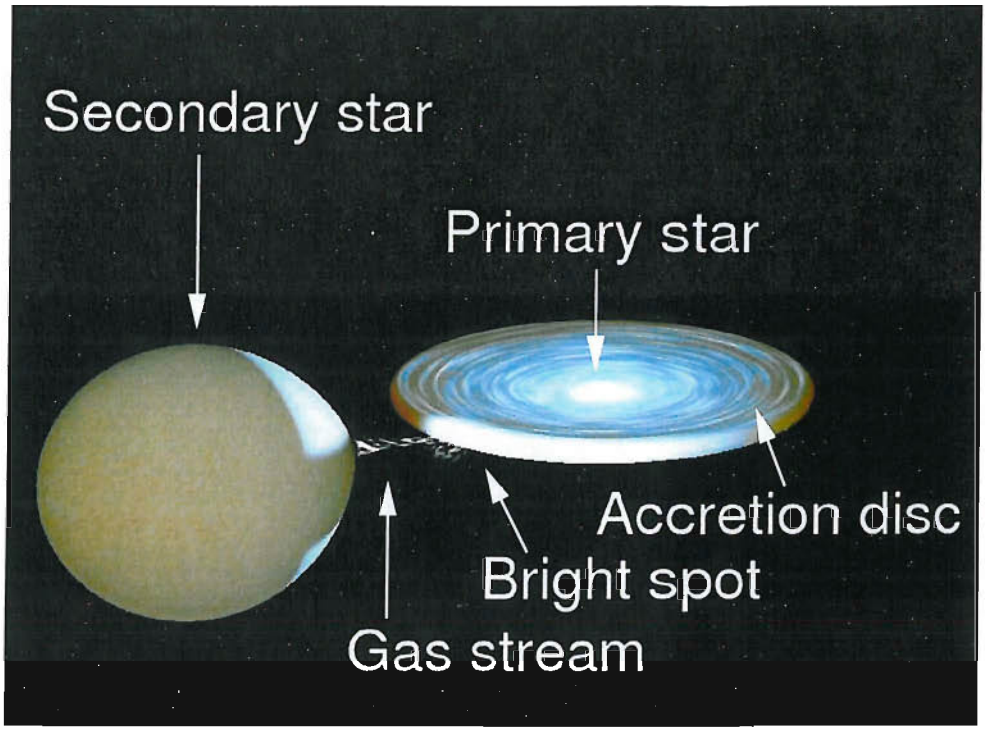

Figure 1.1: The standard components of a CV.

1.2 What CVs are

CVs are semi-detached binary systems which periodically undergo non-destructive cataclysms. Their orbital periods (P_{orb}) range from 78 min to $\sim$ 5 days, although the large majority have $P_{orb} \leq 12$ hours. Their standard components are a white dwarf (also called accretor or primary star); a late type main-sequence star (also called mass donor or secondary star); an accretion disc that surrounds the primary star; and a stream of gas that connects the secondary star with the accretion disc. The point where the stream of gas impacts the accretion disc is usually a very bright feature and so it receives the appropriate name of bright spot (see Figure 1.1). Gravity in a CV is well described by the Roche potential:

$$\Phi(\mathbf{r}) = -\frac{GM_1}{|\mathbf{r}-\mathbf{r_1}|} - \frac{GM_2}{|\mathbf{r}-\mathbf{r_2}|} - \frac{1}{2}(\omega \bigwedge \mathbf{r})^2 \qquad (1.1)$$

where ω is the angular velocity vector, $\mathbf{r_1}$ and $\mathbf{r_2}$ are the position vectors of the

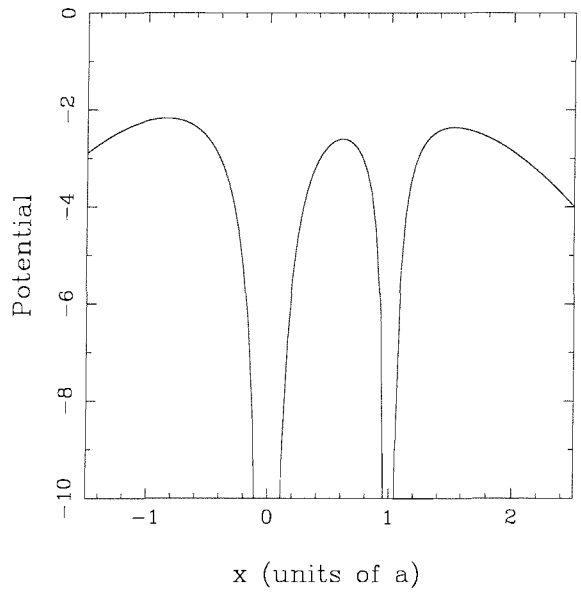

Figure 1.2: The Roche potential along a line through the centres of the stars.

stars and M_1, M_2 are the star masses. Roche potential assumes: synchronous rotation, circular orbits, 2 point masses and a rotating frame of reference. The first two terms in Equation 1.1 correspond to the potential of the two point masses, which for stars is generally a good approximation because their mass is often sufficiently centrally condensed. Circular orbits and synchronous rotation are also good approximations on energetic grounds (if the rotation is not synchronous a general and slightly more complicated form of the potential must be used). The last term in Equation 1.1 is the centrifugal potential which arises due to the use of the co-rotating frame of the binary. The angular velocity, ω is measured with respect to the inertial frame.

In Figure 1.2 I display how the Roche potential varies along the line joining the centres of the stars. There are two potential wells in the position of the component stars. Between them there is a saddle point which is called the Lagrangian point. According to the Roche model, there is one equipotential surface, called a Roche lobe, surrounding each of the component stars. While the primary star is a compact object that can be treated as a point mass at the centre of its Roche lobe, the secondary star overfills its Roche lobe. Matter is then able to flow from the secondary star to the primary star (hence the names mass donor and accretor) via the Lagrangian point.

The gas stream arising from the Lagrangian point does not fall directly on to the surface of the primary star. Rather, it intersects itself, creating a ring of gas at what is called the circularisation radius. Friction acts between the blobs of material flowing at this radius, dissipating energy and making the ring expand both inwards and outwards in order to conserve angular momentum. A disc is thus produced. The inner edge of this disc just touches the primary star's surface. The outer edge of the disc becomes limited in radius by the gravitational action of the secondary star. Therefore, matter just leaving the Lagrangian point finds empty space until it impacts at the outer edge of the disc. Then it travels through the disc, spiralling inwards and finally accreting onto the surface of the primary star.

The spatial scale of CVs is well known. Using Kepler's Third Law we find that the short orbital periods imply that the stars in a CV must be very close to each other, about $1\,R_\odot$. Furthermore, by filling its Roche lobe, the mass donor suffers a deformation which makes it energetically unsustainable to maintain a rotational period different from the orbital period, so we can conclude that it displays synchronous rotation (also called tidal locking). For CVs, the majority of white dwarfs have masses (M_1) in the range $0.5 - 1.0\,M_\odot$, their typical radius being $0.01\ R_\odot$ (Warner 1995). The secondary stars are larger but less massive. From their transits in eclipsing systems we know that their radii are in the range $\sim 0.3 - 0.9\,R_\odot$; if we assume they are main-sequence stars, we can estimate their masses (M_2) to be in the range $0.2 - 0.8\,M_\odot$ (Allen, 2000).

To progress beyond these estimates, a more rigorous approach is needed. Kepler's Third Law can be written as:

$$a^3 = \frac{G}{4\pi^2}\,(M_1 + M_2)\,P_{orb}^2 \tag{1.2}$$

where a is the separation of the two stars. If we call a_1 and a_2 respectively the distances of the primary and the secondary star to the system's mass centre, then:

$$a = a_1\left(\frac{M_1 + M_2}{M_2}\right) \tag{1.3}$$

$$a = a_2\left(\frac{M_1 + M_2}{M_1}\right) \tag{1.4}$$

and also:

$$K_1 = \frac{2\pi a_1}{P_{orb}}\sin i \tag{1.5}$$

$$K_2 = \frac{2\pi a_2}{P_{orb}}\sin i \tag{1.6}$$

where i is the inclination angle of the system (from 0° when it is perpendicular to the line of sight, to 90° when it is parallel to it). K_1 and K_2 are the orbital velocities of the stars as seen from Earth for a system inclination i. Combining all the previous equations we can write:

$$\frac{(M_2 \sin i)^3}{(M_1 + M_2)^2} = \frac{P_{orb} K_1^3}{2\pi G}, \tag{1.7}$$

and

$$\frac{(M_1 \sin i)^3}{(M_1 + M_2)^2} = \frac{P_{orb} K_2^3}{2\pi G}. \tag{1.8}$$

Besides, it can easily be proved that:

$$\frac{K_1}{K_2} = \frac{M_2}{M_1} \tag{1.9}$$

The term on the right of the equation is usually called the mass ratio and denoted by q. Being the easiest parameter to measure, P_{orb} is normally available. Equations 1.7, 1.8 and 1.9 can then be readily solved in terms of M_1 and M_2 if K_1, K_2 and i are measured. The reliable measurement of these quantities is the main theme of Chapter 3.

1.3 Who is who?

The CVs' cataclysms (or eruptions, or outbursts) are observed as modulations in the lightcurves of the systems. It is possible to draw a classification of CVs based on lightcurves, and refined by spectroscopic observations. For non-magnetic CVs:

Dwarf novae (DN) The brightness of these systems temporarily increases by about 2 to 5 magnitudes in what is called an outburst. Outbursts typically last $\sim 2-20$ days, recurring in periods ranging from tens of days to several decades. Outbursts are understood as instabilities that take place in the accretion disc, and whose consequence is to enhance accretion on to the surface of the primary star (and thus to increase the system's brightness). The accretion disc, which in outburst is hot and large, shrinks between outbursts, reaching a cool state called quiescence. The DN group is further subdivided into groups with the following prototypes:

SU UMa In addition to outbursts, these systems exhibit superoutbursts, which are both longer (about 5 times) and brighter (by about 0.7 magnitudes) than regular outbursts.

Z Cam These systems exhibit a mixture of outbursts and standstills, remaining for long periods at $\sim$ 0.7 magnitudes below their maximum brightness. The standstills can last from tens of days to years, and no outbursts are seen meanwhile.

U Gem All the systems that are neither SU UMa nor Z Cam.

Classical novae (CN) These systems have only been observed to erupt once. The change in their brightnesses ranges from 6 to $\sim$ 19 magnitudes. The outburst in a CN is produced by a thermonuclear runaway which originates in accreted hydrogen-rich material on the surface of the primary star.

Recurrent novae (RN) These are systems which originally were classified as CN but then a new outburst was observed. Ejection of a shell from the primary stars's surface is observed in spectroscopic data from RN, separating them from the DN.

Nova-likes (NL) These are all of the non-eruptive CVs, i.e. pre-novae, post-novae and some Z Cam DN for which no outbursts have been observed, possibly because their recurrence periods are much larger than our observation baseline. They are classified as CVs on spectroscopic grounds.

Magnetic CVs are classified in two groups, based on the effect the white dwarf's magnetic field has on the formation of the accretion disc:

Polars No disc is formed, so the material donated by the secondary accretes onto the poles of the white dwarf, following magnetic field lines.

Intermediate polars The disc is truncated at the inner edge where the magnetic field is strong enough.

In this thesis I will focus on non-magnetic systems, so the following sections largely ignore magnetic effects in CVs' spectra.

1.4 CVs' spectra

The spectrum of a CV is the combination of the spectra of its individual components. The key challenge when dealing with CV spectra is finding a way to reliably separate contributions from its many components. This is why observation in many different wavelengths is so important. While a particular component peaks at some wavelengths, it can become nearly undetectable at some others. Thus, by comparison, we can get an approximate idea of the individual contributions in complex cases. Still, it is useful to have some idea of what to expect in each case:

Primary star A white dwarf is a hot star ($T > 12000$K) which closely agrees with the emission predicted for a blackbody. It peaks at blue and UV wavelengths. Hydrogen or helium near the surface of the star is capable of absorbing photons emitted from the star's core, producing broad absorption lines in its continuum.

Secondary star Due to its lower temperature, the spectra from the mass donor peaks at red and infrared wavelengths. The low temperature allows molecules to survive in the stellar atmosphere. These molecules absorb photons producing a complex pattern of dips thanks to their many degrees of freedom. Most of these dips are produced by titanium oxide (TiO).

Accretion disc It dominates at the optical and blue wavelengths, displaying many line features. During the quiescence, double-peaked emission lines are observed, whilst broad absorption can be seen during outburst.

Bright spot It contributes narrow emission detected in Balmer lines and some other lines produced at high energies (e.g. Helium).

Further features in CV spectra arise as products of the irradiation of CVs' components. Notably, this happens often in the case of the secondary star's face, tidally locked on to the primary star. Portions of the accretion disc and prominences on the secondary star are also possible sources of emission due to irradiation.

The components from "standard" CVs described above are readily recognisable in most systems, but some CVs display puzzling variations on the theme. Chapter

5 shows a dramatic example of a system which, although similar in many respects to U Gem, contains striking differences in the spectral signature of components such as the bright spot and the secondary star.

1.4.1 Features from accretion discs

The temperature in an accretion disc is far from constant, either spatially or in time, so this is the hardest component to model in CV spectra. At their outer edge, accretion discs can be relatively cool (5000 K), while at the inner edge they can reach $\sim$ 30000 K (Collier 2001). Therefore, accretion discs cannot be treated as homogeneous entities. Instead, they can be approached as the addition of smaller ones in which some properties remain homogeneous (e.g. isothermal concentric annuli). This gives a good approximation to the shape of the continuum produced by the disc, but its spectral lines require further modelling.

The alternating presence of emission and absorption features in accretion discs suggests that their conditions change. In particular, emission features are expected when the material is optically thin and absorption features when it is optically thick. Mixtures of features, which are often observed, mean that optical conditions in different parts of the disc can sometimes be different too.

The distinctive signature of an accretion disk is the presence of double-peaked emission lines, which are produced by Doppler effect. With respect to the observer, any accretion disc in a CV whose orbital plane is not perfectly perpendicular to the line of sight will offer a receding side and a preceding one. Each of these sides, however, is a collection of emitting regions whose central emission wavelengths will suffer different Doppler displacements according to their velocity around the white dwarf. The whole effect is to produce a double-peaked profile around the wavelength at rest (plus a further displacement blueward or redward due to the motion of the mass centre of the system). The peaks are generated because at any phase there will be a Doppler shift that will be shared by a maximum subsection of the disc, with the shifts being larger and smaller for smaller areas. This is better illustrated in Figure 1.3. Due to the rotation of the disc, a single point will have a chance to be affected by different Doppler shifts as it completes an orbit. If spectra from a CV are plotted as a trailed sequence, the emission from a unique region is then observed

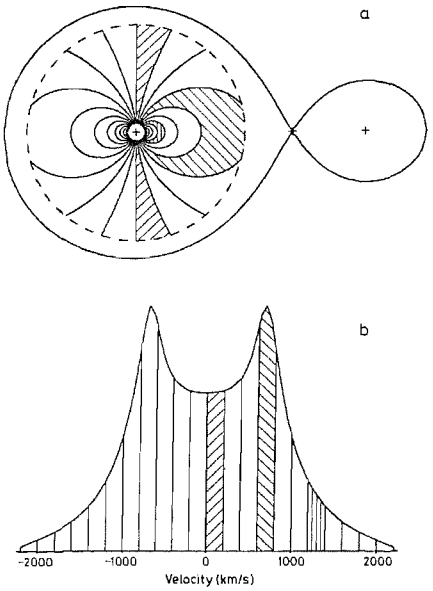

Figure 1.3: Origin of the double peaks on a CV. Patterned regions match areas on the accretion disc (a) and the spectral profile section (b) where they add their emission to. From Horne & Marsh (1986).

as a wave. Due to its shape, this is called an s-wave. Much work goes in attempting to reconstruct the original aspect of the system by observing its s-waves. A good review of the many techniques is given in Boffin et al. (2001). I apply some of these techniques in Chapters 3, 4 and 5.

Another important feature seen in the spectra of accretion discs is the presence of eclipses. When systems have large inclinations, $i >\sim 70°$, the secondary star obscures part of the disc or even the white dwarf. This is detected as a diagonal band of lower emission (because of the region of the disc that has been obscured and which is thus subtracted from the profile) observed near phase 0, when the secondary star is in inferior conjunction with respect to the white dwarf. For slightly lower inclinations the white dwarf is not eclipsed, but the bright spot can be. We talk then of grazing eclipses. The presence of eclipses of any kind helps to constrain the inclination angle of the system. In section 3.2.3 I display trailed spectra which, although richer in features, are excellent illustrations of the expected spectroscopic aspect of an accretion disc in an eclipsing system.

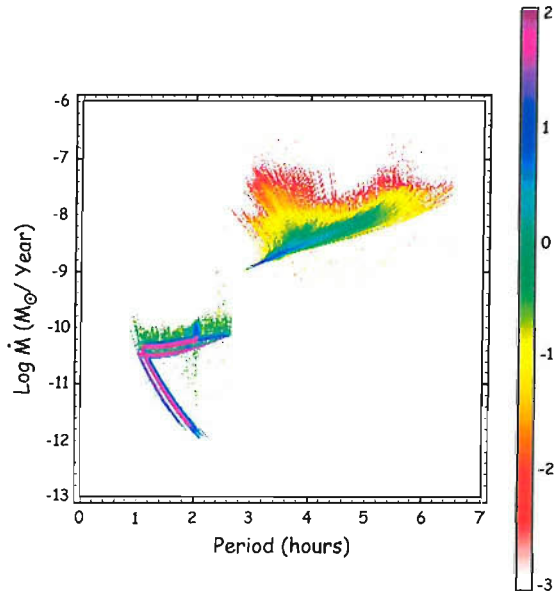

Figure 1.4: Evolution of CVs in terms of mass transference and orbital period. The scale on the right side represents the logarithm of the number of current-epoch CVs at a particular location in the plotted plane. From Howell, Nelson & Rappaport (2001).

1.5 CVs evolve

Figure 1.4 was produced by Howell, Nelson & Rappaport (2001) in the context of a population synthesis study of CVs. It is not factual data but agrees qualitatively very well with the current state of CV observations. If we collapse the data in Figure 1.4 onto its abscissa, we can extract information about the distribution of orbital periods in CVs. This is often presented in the form of an histogram, as in Ritter & Kolb (1998). Three conclusions are immediate by doing this exercise:

1. There is an orbital period cutoff at $\sim$ 12 hours.
2. There is a pronounced lack of systems between $\sim 2 - 3$ hours.
3. There is an orbital period minimum at $\sim$ 78 minutes.

From Equation 1.2 we know that, for any set of masses, Kepler's Third Law tells us that larger orbital periods require larger separations. However, large separations

imply that the secondary star must fill a large Roche lobe, which in turn requires a large mass. For stability reasons the secondary star in a CV must be less massive than the primary star, otherwise the process of transferring matter from one to the other would be a runaway one, and the binary system would not last more than a few years. As the primary star in a CV is a white dwarf, with a mass constrained by the Chandrasekhar limit to be $\leq 1.4\,M_{\odot}$, the mass of the secondary suffers this constraint as well. Therefore, the separation of the two stars and hence the orbital period are limited too, which explains the presence of the long period cutoff.

The lack of systems between $\sim 2-3$ hours is often called the period gap. This feature is currently understood as a transition region between two regimes of angular momentum loss. Let's come back to consider the runaway process mentioned above. When it takes place, the transfer of matter is so intense that matter overfills both Roche lobes. This configuration is called the common envelope phase. Once mass transfer has stopped, the outer shells of the envelope are driven away by the rotation of the binary. Depending on the separation of the pair of stars after this process takes place, the system could become a detached binary or a CV. Binary systems can become CVs at any orbital period, but, to keep matter flowing between the stars, CVs must evolve from long to short periods. This decreases the binary separation and allows the secondary star to stay in contact with its Roche lobe, contact which, to conserve angular momentum, is briefly lost after matter is transferred to the primary. Evolution to shorter periods is possible thanks to a very slow loss of angular momentum from the system, which is explained either by gravitational radiation or by magnetic braking. The latter is the prevalent mechanism for CVs whose period is ≥ 3 hours, but it switches off when the period descends to that value (the reasons to this being poorly understood but probably related to changes in the properties of the mass donor's internal dynamo at such a period). The secondary star then goes through a process of adjustment in which it contracts and matter stops being transferred. Gravitational radiation, much less effective than magnetic braking, shrinks the separation of the stars very slowly until the mass donor resumes contact with its lobe. This happens when the period is ~ 2 hours. From then onwards, the loss of angular momentum is driven by gravitational radiation, which gives to lower mass transfer rates than before.

As the system evolves to shorter periods, the mass of the secondary star is continuously decreasing, as it is fed to the primary star. At some point the mass of the

secondary star is so low that its gas pressure is no longer able to support the star and it reaches a degenerate state. This happens when the orbital period is $\sim$ 78 minutes. In this new state the mass donor slowly expands as its matter decreases. This reaction helps the gravitational radiation mechanism so that the contact of the secondary star with its Roche lobe is restablished earlier and with the star at a larger size than it would have had if the star had kept shrinking instead of expanding. The system evolves then to longer periods, resulting in a minimum period as noted before. The upper branch in Figure 1.4 shows CVs evolving towards the period minimum, while the lower branch corresponds to CVs evolving from it. This will be a key theme in Chapter 4.

M_2 cannot but continue decreasing with time. At some stage its mass will be so low that gravitational radiation will no longer be an effective mechanism to extract angular momentum from the system. Also, its brightness will have decreased dramatically. This makes such systems very hard to detect and understandably they are enormously under-represented in catalogs. However, theoretical models indicate that most stars should be below the period gap and a very important fraction should have already reached the period minimum and be evolving towards longer periods (note colour scale in Figure 1.4).

1.6 Aims of this work

In this work I examine spectra from three objects. The dwarf nova U Gem, the first one, is interesting in many ways because there is a lot of information already known about it. It displays grazing eclipses, which means we can have an estimate of the inclination angle and of the size of the mass donor. More importantly, all the components of the system have been observed by spectroscopic methods. The bright spot, the secondary star and the accretion disc are readily observed in optical spectroscopy, which provides good constraints over the dynamical parameters of the system. The primary star has also been observed in UV spectroscopy, which allowed Long and Gilliland (1999) to directly measure the white dwarf's velocity. Yet, the data I present in this work provides refinement to several parameters, and opens up discussion over features reported for the first time.

The second object I examine is GD 552, a nova-like. I present evidence that GD 552 is a post-period-bounce system. There is a dramatic defficiency of post-period-bounce CVs in current catalogs, and this could well be one of the first CVs for which clear evidence is presented about it reaching such an evolutionary phase. This is important because theory predicts that a majority of systems should have reached this stage.

The third object, GY Cnc, is a dwarf nova which was chosen as a comparison with U Gem. It is remarkably similar in many aspects, but preliminary spectroscopic evidence suggested that there were fundamental differences too. Chapter 5 is a first look at high resolution data of GY Cnc.

Chapter 2

Data acquisition and reduction

The data used in the thesis were acquired in several different runs that took place in the Isaac Newton Group (ING) of telescopes. This group, located on the island of La Palma, Canary Islands (Spain), offers three telescopes of which two were used: the 2.5-m Isaac Newton Telescope (INT hereafter) and the 4.2-m William Herschel Telescope (WHT hereafter). The latter is particularly well suited for observation of CVs due to the availability of the ISIS spectrograph, which allows one to carry out double-beam spectroscopy, enabling research based on simultaneous observation of several different wavelengths.

In this chapter I present details of the data obtained and the procedures applied in their reduction.

2.1 Datasets

2.1.1 U Gem and GY Cnc data

The observations were taken in October 1990 and January 2001 at La Palma in the Canary Islands (see Tables 2.1 and 2.2 for details).

In the case of U Gem, in 1990 the INT was used in conjunction with the Inter-

mediate Dispersion Spectrograph (IDS) to acquire one dataset. In 2001, the WHT was used with the double-beamed high-resolution ISIS spectrograph. Two datasets, covering different wavelength ranges and spanning 4 nights, were acquired during the 2001 session. In the case of GY Cnc, only the WHT/ISIS was used to acquire data during part of two nights in 2001.

The general observing procedures were common to all the observing runs, namely: the region of the CCD affected by vignetting was located and excluded from being used for data; a binning factor was decided to establish a good compromise between the readout time and the noise added to the data; a noise test was performed on every CCD in order to estimate the readout noise and the gain (see Section 2.2.1).

During the observations of U Gem, the slit was oriented at a position angle of 150.6° in order to include a star nearby to U Gem that could be used to correct for slit loses. For GY Cnc the slit was analogously oriented at an angle of 101.3°.

The spectrophotometric standard HD19445 and one featureless star were observed during the nights with best seeing (~0.7") for flux calibration and to remove the effect of telluric lines on the red data (Bessell 1999).

Flat-fields and comparison arc spectra were taken approximately every 60 minutes. In the case of the 2001 data, these calibration frames were acquired independently for the red and the blue datasets.

The weather was clear throughout most of our run with seeing of order 1" for most of it.

2.1.2 GD 552 data

The observations were taken in January and August 2001 at La Palma (see Table 2.2 for details). In January 2001, the INT was used with the IDS to acquire one dataset. Another dataset obtained in January 2001 used the WHT and ISIS. In August 2001 only the WHT/ISIS was used.

The spectrophotometric standard HD19445 was observed for flux calibration and to remove the effect of telluric lines on the red data (Bessell 1999). Flat-fields

Table 2.1: Summary of U Gem data used in the analysis. All the 2001 were made with the WHT/ISIS, while the 1990 observations were made with the INT/IDS. In this table MD stands for 'mean dispersion'. FWHM is the full width at half maximum of the lines in which blending seemed most unlikely. T is the mean exposure time per frame and DT is the average dead time between exposures. N is the number of spectra collected per night per arm.

CCD	Grating	Date	Start - End (UT)	Orbits covered	λ range (Å)	MD (Å pixel^{-1})	FWHM (Å)	T/DT (s)	N
EEV12	H2400B	12/13 Jan 2001	22:14-05:32	1.719	4618-4985	0.21	0.42	120/12	182
TEK4	R1200R	12/13 Jan 2001	22:14-05:32	1.719	6343-6751	0.40	0.80	50/6	419
EEV12	H2400B	13/14 Jan 2001	21:08-03:54	1.594	4618-4985	0.21	0.42	120/12	176
TEK4	R1200R	13/14 Jan 2001	21:08-03:54	1.594	6343-6751	0.40	0.80	50/6	410
EEV12	H2400B	14/15 Jan 2001	21:44-02:07	1.032	4618-4985	0.21	0.42	120/12	112
TEK4	R1200R	14/15 Jan 2001	21:44-02:07	1.032	6343-6751	0.40	0.80	50/6	259
EEV12	H2400B	15/16 Jan 2001	21:22-04:49	1.755	4618-4985	0.21	0.42	120/12	191
TEK4	R1200R	15/16 Jan 2001	21:22-04:49	1.755	6343-6751	0.40	0.80	50/6	442
GEC 385x578	13	09/10 Feb 1990	22:03-04:03	1.413	6722-6517	0.36	0.72	150/35	105
GEC 385x578	13	12/13 Feb 1990	22:40-03:57	1.244	6722-6517	0.36	0.72	150/35	96

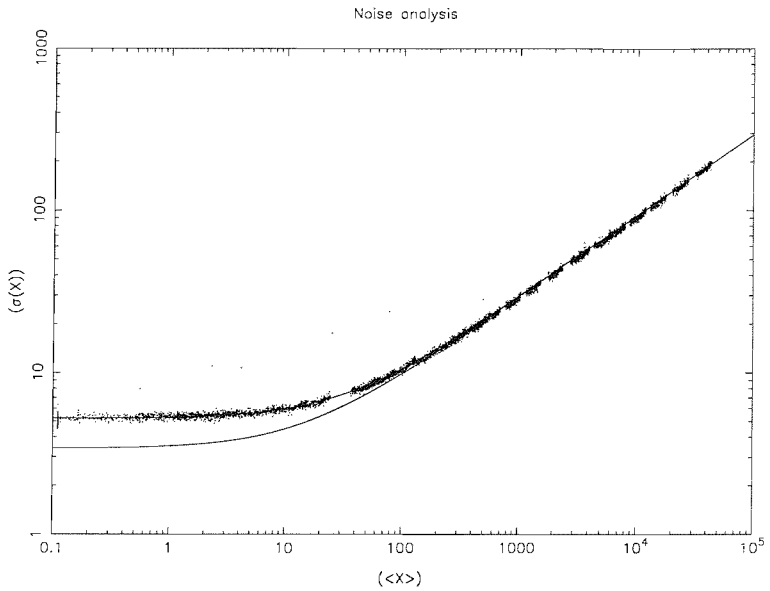

Figure 2.1: Comparison of nominal and calculated values for readout and gain in the CCD used for observing U Gem in 2001, blue arm.

and comparison arc spectra were taken at regular intervals (every $\sim$ 60 min). The weather was good during all the observing runs, with no clouds and a typical seeing of 1 arcsecond.

2.2 Common reduction procedures

2.2.1 Noise test

For the purposes of extracting data of scientific value from CCD images, the electronics of the CCDs are mainly characterised by two parameters: the gain and the readout noise. The gain defines how the charge collected in the individual CCD pixels will be assigned a number that can be digitally stored. The readout is the noise introduced in the data by the act of reading the CCD charge and transforming it into digital data. This noise is partly produced by statistical reasons (i.e. due to the counting process that takes place in the CCD) and partly due to spurious electrons added by the electronic components.

CCD frames acquired in professional observatories always report nominal values

Table 2.2: Summary of GD 552 and GY Cnc data used in the analysis. Abbreviations are used as in Table 2.1.

GD 552

Telescope/ Instrument	CCD/Grating	Date	Start - End (UT)	Orbits covered	λ range (Å)	MD (Å pixel^{-1})	FWHM (Å)	T/DT (s)	N
INT/IDS	EEV10/R1200B	12/13 Jan 2001	19:48-22:06	1.343	6318-6719	0.39	0.78	300/30	26
WHT/ISIS	EEV12/H2400B	12/13 Jan 2001	19:52-21:13	0.788	4618-4985	0.21	0.42	300/12	32
WHT/ISIS	EEV12/R1200B	13/14 Aug 2001	23:28-05:34	2.979	4301-4962	0.22	0.69	290/16	61
WHT/ISIS	TEK4/R316R	13/14 Aug 2001	23:35-05:34	2.911	7306-8814	1.48	3.43	300/5	63

GY Cnc

Telescope/ Instrument	CCD/Grating	Date	Start - End (UT)	Orbits covered	λ range (Å)	MD (Å pixel^{-1})	FWHM (Å)	T/DT (s)	N
WHT/ISIS	EEV12/H2400B	13/14 Jan 2001	04:04-06:54	1.594	4618-4985	0.21	0.42	300/20	27
WHT/ISIS	TEK4/R1200R	13/14 Jan 2001	04:04-06:54	1.594	6338-6746	0.40	0.80	100/7	76
WHT/ISIS	EEV12/H2400B	14/15 Jan 2001	02:10-06:34	1.032	4618-4985	0.21	0.42	300/20	39
WHT/ISIS	TEK4/R1200R	14/15 Jan 2001	02:10-06:34	1.032	6338-6746	0.40	0.80	100/7	134

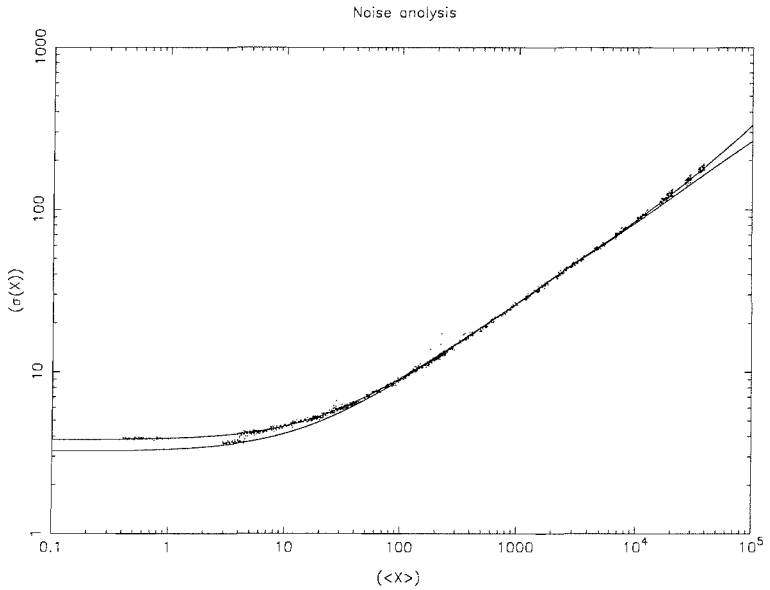

Figure 2.2: Comparison of nominal and calculated values for readout and gain in the CCD used for observing U Gem in 2001, red arm.

for gain and readout, but these are not always reliable. Readout, for instance, is sensitive to temperature variations in the equipment. If significant time has transpired since the tests were done, the response of the equipment to their own internal electrical currents could have changed and the readout value could be quite different too. It is a good idea, then, to perform a fresh test of these parameters when possible. I will refer to this as a "noise test".

A noise test is performed by acquiring a series of flat fields with different count levels. A bias level is removed, and a mean flat field is applied to remove large scale variations from every frame (see Sections 2.2.2 and 2.2.4). Then, a computer algorithm works on boxes of pixels whose size is defined at will. Inside each box, the number of counts in each pixel is subtracted from the average number of counts from its 8 neighbors. An average of the absolute values of these differences, $\langle X \rangle$, is computed and the standard devation, $\sigma(X)$, is calculated assuming gaussian statistics. This procedure is more robust against outliers than the usual root mean square approach.

Two numbers, $\langle X \rangle$ and $\sigma(X)$, are obtained from this procedure for each box. As every frame is divided into lots of boxes (depending on the choice of size), eventually one obtains many points representing the counts in different regions of the CCD.

Ideally they would all be the same but this is hardly ever the case; still, they often make a cloud with decreasing dispersion for large values of $\langle X \rangle$. You can plot these clouds, one for each frame, and fit a model to them. The model I used is:

$$Noise = \sqrt{Readout^2 + \frac{Counts}{Gain} + (Counts \times Grain)^2} \tag{2.1}$$

where "*Grain*" is a small number (often very close to zero) that describes imperfect flat fielding.

Figures 2.1 and 2.2 show a comparison between the model fitted according to the test described above (the line that consistently goes through the points) and the nominal values reported for the CCDs in 2001 (the line that deviates).

2.2.2 Debiassing

CCDs assign a digital value to unexposed pixels. This bias must be subtracted from the data to be analysed. To do this, the bias level can be computed either from unexposed frames (bias frames) or from regions of the CCD, real or simulated (the "overscan"), which are not exposed during the acquisition of the data. Once this level is reliably measured (ideally averaging the unexposed regions from many frames), then the debiassing process consists just in subtracting this value from each frame.

2.2.3 The 2001 pattern noise

The ISIS spectrograph allows the simultaneous acquisition of data on two different wavelength ranges. The beam of light is split and each arm is acquired in a different CCD. I found that the TEK CCD, used for the red dataset, introduced a spurious pattern of noise on the bias frames and, reasonably, on the data as well. The bottom pannel in Figure 2.3 shows an example of the pattern, which is typically due to electronic pick-up noise.

I realised that the shape of the pattern noise evolved with time, making it risky to attempt any removal of it. However, this noise occured at such a low level ($\leq$10 counts) that it seemed that the only necessary precaution was to keep the fact of

its existence in mind, judging carefully any result that could be dependent on such small variations in flux. None of the results presented in this work is sensitive to this problem.

2.2.4 Flat fielding and data extraction

CCDs respond inhomogeneously to photons. Also, the combination of a CCD with the spectrograph and other devices (e.g. dichroics) produce a pixel-to-pixel sensitivity that changes over both long and short scales of the frames, and so a procedure must be devised to avoid introducing spurious variations in the science frames. One difficulty in devising such a procedure lies in the fact that the instruments and the detectors also have different responses to different light conditions. Thus, if you want to account for sensitivity variations affecting the data, you need to measure those variations in conditions as similar as possible to the ones you deal with while observing. Images from the sky during twilight contain information that correlates better the quantum efficiency of the detector with wavelength than it is possible to achieve with dome lamps (e.g. Howell, 2000), so a good technique is to measure the pixel-to-pixel variations using a large bunch of twilight frames. However, if the sensitivity varies during the night, flat fields must be taken during the night-time. These must be taken with artificial light (tungsten light internal to the spectrograph) which unfortunately does not necessarily illuminate the slit correctly.

The best of the two approaches can be combined, though. It is possible to use the internal flats to account for short time scale variations of sensitivity, but correcting these by a considering the response observed in twilight frames. The resulting frame is called a balance frame. To construct the balance frame, the two nearest flats to a science frame were interpolated and a linear fit was applied to its collapse in the spatial direction. The interpolated flat was divided then by the fit. Next, an average spatial profile of the flat was calculated and divided out of it. The average spatial profile from a twilight frame was then multiplied onto the flat. Finally, the flat was inverted and normalised to 1. This balance frame is then multiplied onto the science frame.

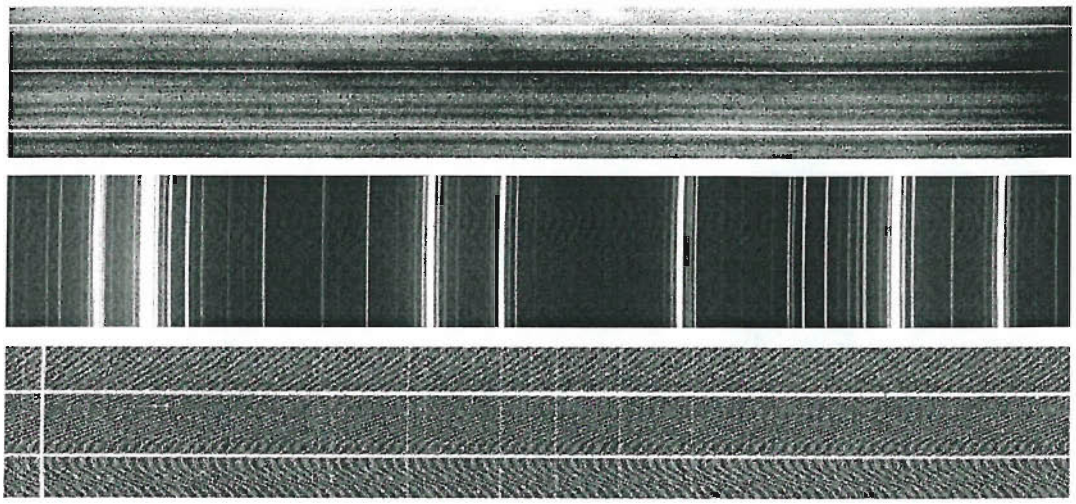

Figure 2.3: Typical frames used in the data reductions. From top to bottom: balance frame, arc, and one typical science frame for U Gem 2001, red arm. The top two images are saturated at 90% of their peak level. The bottom figure is saturated at 50% of its peak level.

2.2.5 Optimal extraction

The debiassed and flat-fielded data can be extracted by using optimal extraction, described in Horne (1986) and Marsh (1989). According to this algorithm, first a spatial profile is constructed. Then, the extraction consists of averaging a number of columns or rows where the spectrum lies (columns in my case), weighting this average by the spatial profile. What this ensures is that columns containing less signal, and that are therefore noisier, will add less to the total average. Overall, this improves the signal to noise ratio of the extracted spectra.

2.2.6 Wavelength calibration

During the observing run, calibration lamps are observed regularly to produce arc frames. This can be later used to produce a wavelength scale for each science frame by interpolating the two nearest arc frames. This process requires a two step approach. First, the spectral lines detected in each arc frame are identified by comparison with standard catalogs. This defines a wavelength scale that usually is not linear. In my case the data was calibrated using Cu-Ne and Cu-Ar lamps, and

much care was taken in selecting lines with no blends.

The second stage consists of the interpolation of these arc scales which is done on the basis of the time difference between the acquisition of the science and the arc frame. A final check performed on this process is the calculation of the drift of the wavelength scales along the night. In general you expect it to be smooth but for the case of programmed telescope motions or accidental vibrations.

2.2.7 Flux calibration and telluric correction

My data are spectra from three CVs. The fluxes of spectroscopic data must be calibrated by comparison with the fluxes measured in standard stars. This is done again as a two stage process. The first part requires observation of a standard star for which tabulated data (flux versus wavelength) exists. The observations of this standard star are then compared to the data in the table, and factors are derived to make them match. The counts in the data are left untouched, but a parallel scale is created which contains the information about flux. In the second stage these factors are introduced in the science frames, providing them with a flux scale calculated according their count scales and the flux factors.

If the data are affected by telluric absorption, then it is possible to attempt some degree of correction by using a telluric template. This is a spectrum profile of a standard star which has been normalised and set equal to 1 outside the range affected by telluric absorption. This template is then roughly used as a factor to multiply science frames by, but its performance is far from perfect. I have tried to avoid overanalysing regions intensely affected by this problem in my thesis.

2.2.8 Additional procedures

Whenever possible, a comparison star was included in the slit. Also, one frame was acquired opening the slit much more than in regular observations, when the run was nearest the zenith. This is done to correct as much as possible for the flux that is lost due to the use of a narrow slit. The observation is taken close to the zenith to reduce the effect of atmospheric distortion as much as possible.

In this case, the extraction of data was done for both the CV and the comparison star. Then, the continua in the comparison star spectra were fitted with constants. These constants were normalised dividing by the constant fitted to the spectra obtained with the wide slit. Finally, the CV spectra were divided by these normalised constants.

For the August 2001 datasets no comparison star was observed, so I simply normalised the continua of these spectra. Additionally, all the datasets were cleaned of cosmic rays before proceeding with the analyses.

2.3 What next?

After the procedures described in Section 2.2 were completed, the datasets were ready to be analysed. The analysis is explained in detail in Chapters 3, 4 and 5. Basically, first you have the option of working with the data "as is" at this stage, which is useful, for instance, for producing average profiles giving an idea of the relative flux intensities from different spectral lines and of the shape and intensity of the continuum. Then you can fit a low-order polynomial to the continua and subtract these fits from the profiles. This is useful, for example, to study the variation in the intensity of the lines with orbital phase.

If no comparison star was included in the slit, then the correction described in Section 2.2.8 cannot be applied. In this case, the best one can do is normalise the dataset using a fit to the continua. This had to be done for the GD 552 datasets, as I will show in Chapter 4.

Chapter 3

U Gem

3.1 Introduction

Theoretical models of the evolution of cataclysmic variable stars (CVs) make predictions about the distributions of their physical parameters such as orbital period, mass ratio and the individual masses of the two stars. If we can measure these, we can test the (many) assumptions that go into the theory, many of which are of interest in the broader context of binary star evolution. The same parameters are needed in gaining an accurate understanding of the accretion processes which dominate these stars. Unfortunately, it is probably fair to say that the only reliable physical parameter for the majority of cataclysmic variable stars is the orbital period, with perhaps the spectral type of the donor star coming a rather distant second. In this ranking, the masses of the white dwarf and quasi-main-sequence components are so uncertain that they are often barely mentioned in the context of evolution, with good reason. First, as for most binary stars, it is extremely hard to measure orbital inclinations. However, even the mass ratios of cataclysmic variable stars are poorly measured, and this is due in large part to the difficulty of measuring the radial velocity of the accreting white dwarfs.

In most CVs, one cannot see the white dwarf at optical wavelengths which are dominated by emission from the accreting material. Instead we use the accreting matter as a proxy for the white dwarf by measuring the radial velocities of the

optical emission lines. Restricting ourselves to non-magnetic systems, the emission lines are formed in the accretion disc, and often have the classic double-peaked form expected for Doppler-shifting from the surface of a keplerian disc. The high-velocity wings of the emission lines therefore form close to the white dwarf where we can expect flow to be axi-symmetric. If so, these wings will trace the motion of the white dwarf. At least, this is the idea behind very many studies of these systems. It has long been clear however that this method fails in practice: in those systems in which one has independent knowledge of the orbital phase, the emission line radial velocities invariably fail to match expectations (Stover 1981). Nevertheless, it is common to continue using the semi-amplitudes for mass determination, perhaps because there has not been any direct evidence for the magnitude of the distortion. This changed when Long & Gilliland (1999) were able to measure the radial velocity semi-amplitude of the white dwarf in U Gem from direct measurements of narrow metal lines from its surface. In this case, the phase agreed perfectly with that expected from observations of the mass donor and measurements of the eclipse in this partially-eclipsing system. Long & Gilliland (1999) measured $K_1 = 107.1 \pm 2.1\,\mathrm{km\,s^{-1}}$. I believe that the direct nature of this measurement makes it the most accurate to date for any CV, and it gives us the chance to see just what the nature of the distortion of the emission line measurements is in one system at least. (The one other case is AE Aqr (Welsh et al. 1995) in which pulsations from the white dwarf yield a good estimate of K_1, but this is a very unusual CV and not suited to testing the general method of measuring K_1 from line emission.)

U Gem is interesting from several other points of view: it is a double-lined, partially-eclipsing system, and is one of the brightest dwarf novae. It has prominent emission from the gas stream/disc impact region which has a velocity in-between that of a keplerian disc and a ballistic stream (Marsh et al. 1990). Finally, during outburst it has shown spiral shocks (Groot 2001). We will see that the new data have something to tell us on all of these issues.

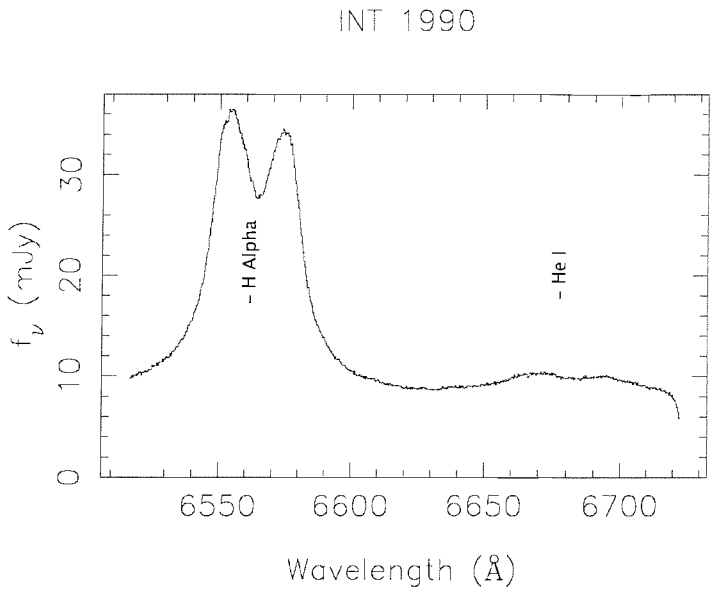

Figure 3.1: Average flux-calibrated spectrum for the U Gem dataset acquired with the INT/IDS in 1990.

3.2 Results

3.2.1 Average spectra

Figures 3.1, 3.2 and 3.3 show the average spectrum for each available dataset. U Gem shows broad Balmer (Hα, Hβ) and Fe II 4923.92 Å (hereafter Fe II). He I 6678.149 Å (hereafter He I) and the high excitation line He II 4685.750 Å (hereafter He II) are also present, producing narrower profiles. Next to Fe II 4923.92 there is emission at an unidentified wavelength (Fe II 5018.44 Å?), which, as we will see later, introduces some contamination in Fe II.

The B-band profiles, like the 1990 ones, show double-peaked structure usually seen in hydrogen-dominated CVs, commonly attributed to the presence of a rotating accretion disc around the compact member of a binary system. However, the 2001 R-band profiles exhibit a central stationary component which is reminiscent of similar features seen in a handful of other systems. I discuss this component in detail in Section 3.2.4.2.

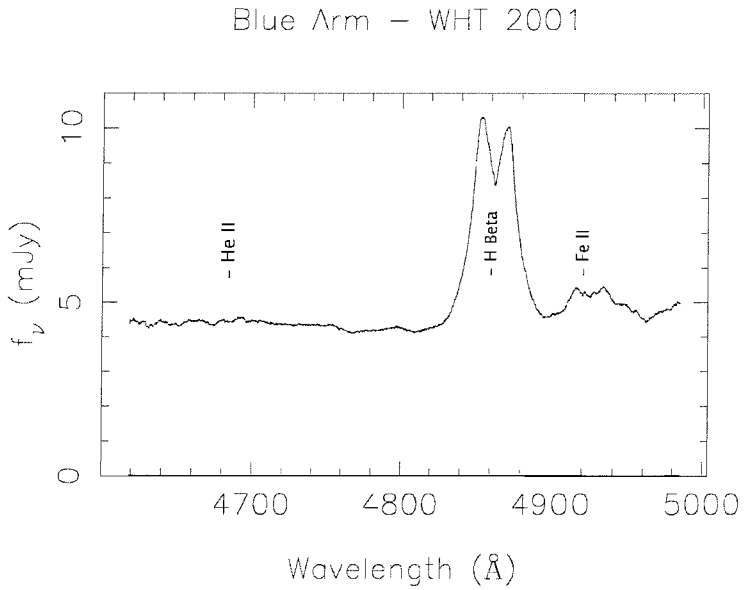

Figure 3.2: Average flux-calibrated spectrum for the U Gem dataset acquired with the blue arm of the WHT/ISIS in 2001.

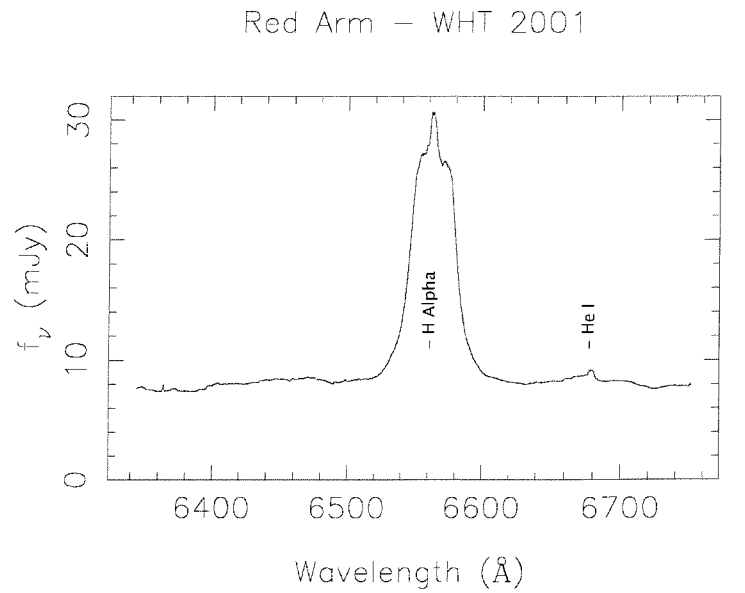

Figure 3.3: Average flux-calibrated spectrum for the dataset acquired with red arm of the WHT/ISIS in 2001.

3.2.2 Light curves

I selected regions of the 2001 data from the continuum in which emission lines were not present (6400-6480 Å, 4620-4650 Å and 4720-4470 Å). Having done so I computed light curves of the continuum by summing the flux in those ranges. Then I subtracted a constant fit to the continuum and defined wavelength ranges centred on the emission lines. In units of velocity the ranges extended from -2000 to 2000 km s^{-1} around each line, with the exception of Fe II, in which the range was -1500 to 1500 km s^{-1} in order to prevent contamination from the wings of Hβ, and He II, in which I used -650 to 650 km s^{-1} due to the narrowness of the emission. In Figure 3.4 I show the resulting light curves. Appropriate flux scales were used for each light curve in order to improve visualization of the features.

Now I try to interpret the features observed in Figure 3.4 proceeding from top to bottom.

Both the blue and the red continuum light curves display smooth, moderately deep, narrow eclipses just after phase 0. As is well-known, this is is the eclipse of the gas stream/disc impact region, or "bright-spot" at the edge of the disc. U Gem is insufficiently inclined for the white dwarf to be eclipsed.

The light curves of Hα and Hβ show broad humps around phases 0.25 and 0.75. Although reminiscent of ellipsoidal modulations produced by the Roche deformation of the mass donor, we will see later that the mass donor does not contribute sufficient flux for this to be the case, and it is more likely that these humps are caused by variations in the strength of emission from the bright-spot. The light curves also display a shallow eclipse roughly centred around phase 0, and extending symmetrically $\sim$0.1 in phase to both sides. This is produced by the mass donor passing in front of the outer part of the accretion disc.

In He II the eclipse occurs slightly after phase 0; we will see later that He II is dominated by emission from the bright-spot. The peak of light near phase 0.9 is congruous with the orbital humps detected in the continua.

The light curve of He I and Fe IIare strongly modulated, with the peak flux at phase 0.3-0.4 caused by an increase in the contribution of the bright-spot, as we will see later.

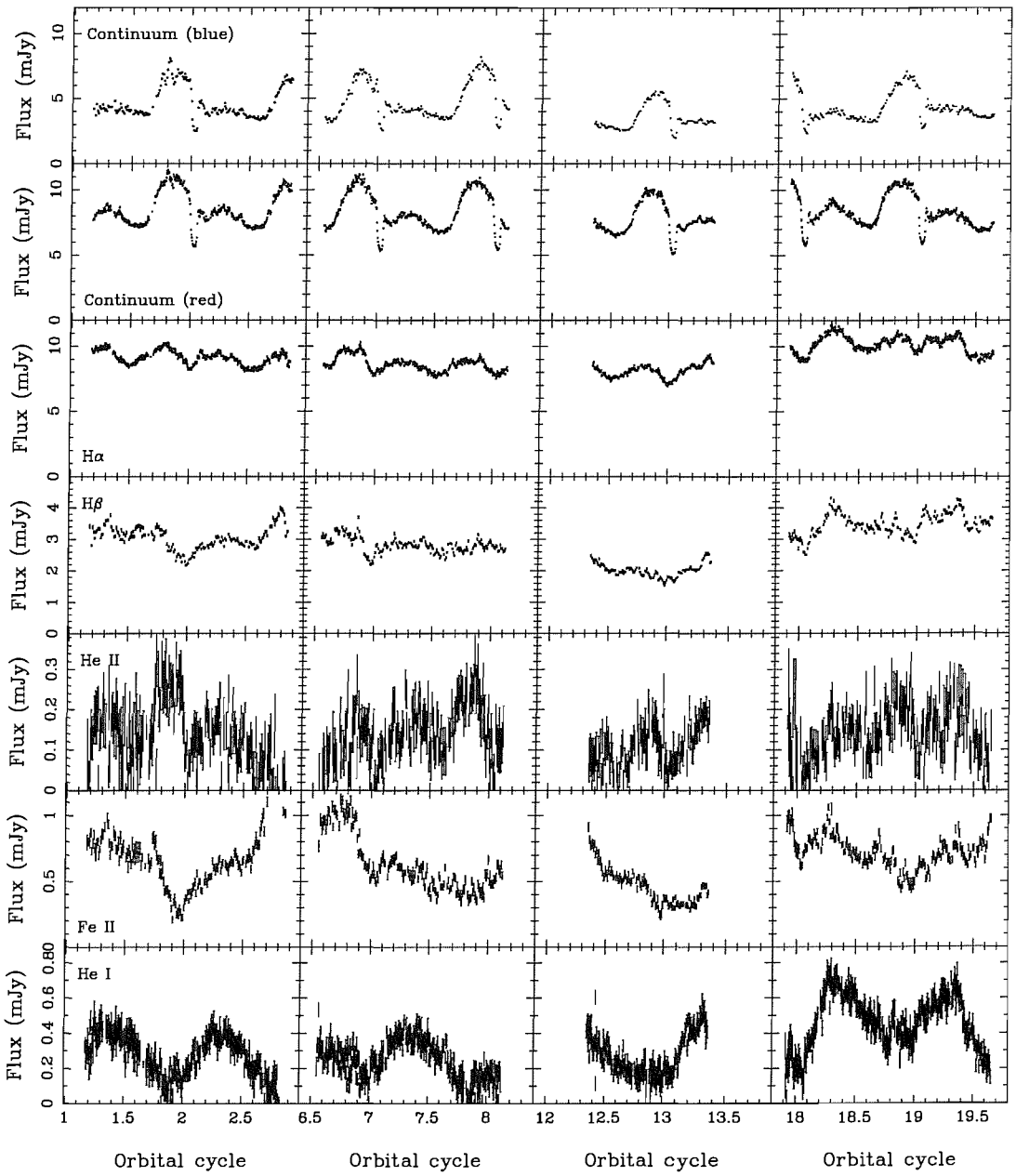

Figure 3.4: Continuum and emission light curves of the 2001 WHT/ISIS data. Cycle 0 has been set to the cycle 80740 according to the ephemeris used in this paper.

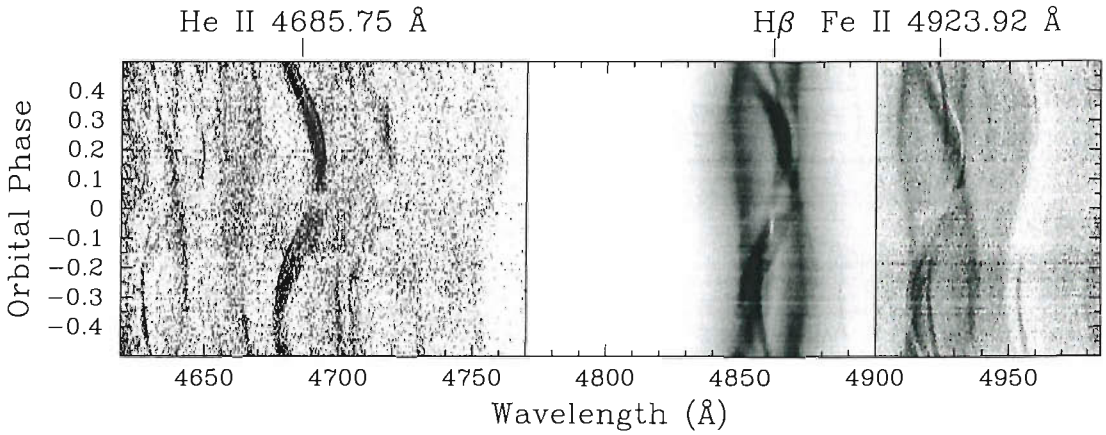

Figure 3.5: The blue data taken in January 2001, binned into 100 bins of orbital phase. As the detected features show emission of very different strengths from each other, a common frame for visualisation is difficult to achieve. I divided the whole dataset producing one panel for each wavelength and then I normalised the colour scale from the continuum level to a maximum intensity in each panel. The maximum plotted levels are: 0.5 mJy (He II), 7.0 mJy (H β) and 2.0 mJy (Fe II).

3.2.3 Trailed spectra

Figures 3.5 and 3.6 show average trailed spectra corresponding to the 2001 dataset. In Figure 3.10 I display the trailed spectra for the 1990 dataset. Emission lines of He II, H β and Fe II, H α and He I are visible. The trailed spectra show a remarkably rich mix of features, some of them well-known from earlier work on U Gem and related systems, but others seen here for the first time. I start by describing the more-or-less standard features visible in the trails.

3.2.3.1 Standard features

Double-peaked emission from the disc is visible in most lines as a pair of parallel lines executing sinusoidal motion with orbital phase. Emission from the mass donor is seen as a sinusoid of larger amplitude, roughly in anti-phase with the disc emission, and modulated in strength with phase, being weakest near the eclipse at phase zero. This is evidence that this emission is concentrated on the side of the donor facing the white dwarf and accretion disc; it is most clearly seen in the light of Fe II (Fig. 3.5). Yet another sinusoid comes from the stream/disc impact region. It has a somewhat

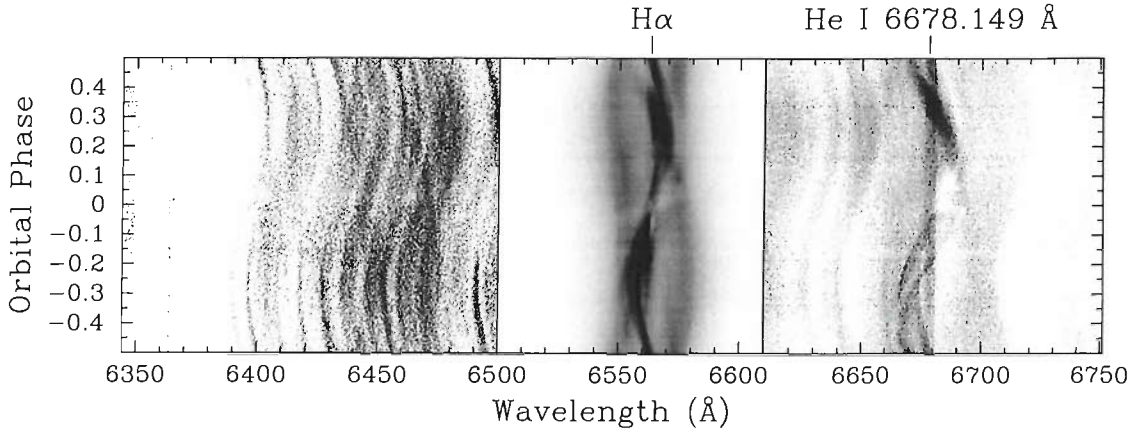

Figure 3.6: The red data taken in January 2001. The technique of visualisation is the one described for the blue data. I used 200 bins of orbital phase this time. Also, I reserved a panel to show part of the continua of the spectra. The maximum plotted levels are: 1.0 mJy (continuum), 28.0 mJy (Hα) and 2.0 mJy (He I).

similar path to the donor star emission, but has a higher amplitude and is advanced in phase compared to the donor. It can be seen in Hβ for instance as a feature moving to the right (red) of line centre around phase zero (Fig. 3.5).

The effect of the partial eclipse on the lines is relatively subtle in many lines, but is seen clearly in Hα as a region of low flux running diagonally between the double-peaks from the lower-left towards the upper-right between phases 0.95 and 0.05. This is the effect of eclipsing Doppler-shifted emission from a prograde rotating disc (Greenstein & Kraft 1959; Young & Schneider 1980); I use it in Section 3.2.5 to measure the orbital inclination of U Gem.

3.2.3.2 Low-velocity absorption and emission

In the 2001 dataset, in both Hα and Hβ (but most obviously in Hβ, see Figure 3.7) a narrow absorption feature appears at line centre immediately before eclipse (phase 0.91 to 0.98). Although it has not been seen before, this could be a result of the improved data quality rather than a true change of structure, yet the latter is certainly possible.

Also in Hα, but even more clearly in He I , there is emission of low, almost zero, semi-amplitude at line centre. I refer to this as "the low-velocity emission".

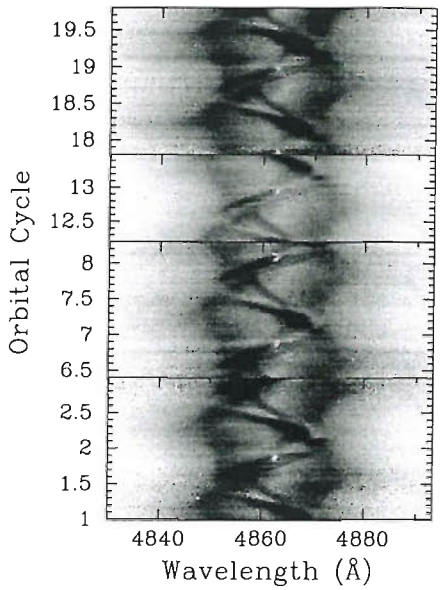

Figure 3.7: The 2001 Hβ data without phase-binning. Cycle 0 has been set to the cycle 80740 according to the ephemeris used in this paper.

Such emission is hard to understand because there is no part of the system that is stationary in this manner. Figures 3.8 and 3.9 show actual line profiles in which I have highlighted these intriguing features at certain orbital phases in which they are seen reasonably isolated.

The 1990 dataset, although noisier, shows some significant differences from the more recent data (see Figure 3.10). Most significantly, the double peaks of Hα are more in-filled in the 2001 data. This is seen for example in the average spectra (compare Figure 3.1 and 3.3), which reveal an extra peak between the accretion disc's characteristic double peak. This suggests that the low velocity emission was not present in 1990. It is more difficult to conclude whether the narrow absorption prior to eclipse was absent too. The lower signal-to-noise and resolution of the 1990 data make it hard to be sure of this (Fig. 3.10). If so, this would give some support to an association of these features (see Section 3.2.4.3).

3.2.3.3 Low-level structure in the continuum

The continuum seen in Figure 3.6 shows a mass of lines at a low level of flux. In several of these lines a modulation is seen resembling the one produced by the mass

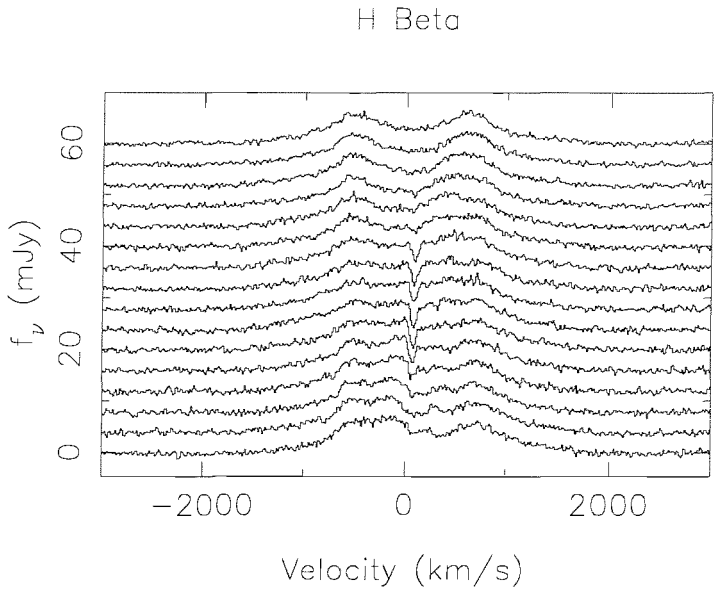

Figure 3.8: Hβ from orbital phase 0.89 to 0.01. The absorption is seen as a series of dips near zero velocity in the profiles.

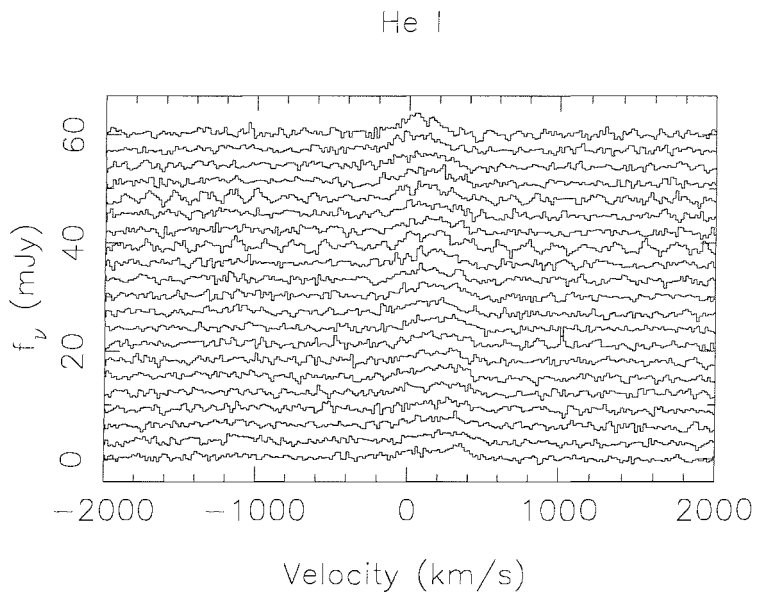

Figure 3.9: He I from orbital phase 0.25 to 0.35. The emission is seen as a stationary bulge near zero velocity in the profiles.

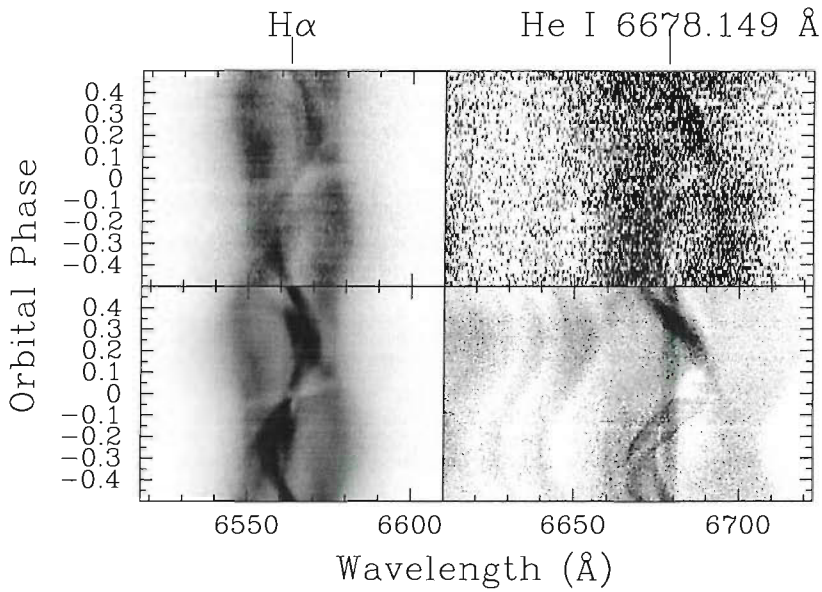

Figure 3.10: The two upper panels show the data taken in 1990. The visualisation is done as explained for previous images but using only 60 orbital phase bins. The maximum plotted levels are: 37.0 mJy (H α) and 2.0 mJy (He I). The two bottom panels replicate data already presented in Figure 3.6, in order to allow a direct comparison of the two datasets. The maximum plotted levels for the bottom panels are as in Figure 3.6.

donor's orbital motion, so I attempted to track the source of the lines. To improve the S/N of this region I phase binned the spectra in 50 phases. Then I selected one of the spectra as a template and did a cross-correlation with the set of phase binned data, backprojecting later. This technique, called skew-mapping, is widely used for detecting the presence of weak features from the mass donor in the spectra of CVs but can be more generally used to track the source of any given set of features against a suitable template (Smith, Dhillon & Marsh 1998). The result of this procedure, displayed in Figure 3.11, allowed us to estimate that the emission was produced in a region centred around (0, 200) $\mathrm{km\,s^{-1}}$. Now I phase binned the spectra in 200 phases and removed the sinusoidal velocity (0, 200) $\mathrm{km\,s^{-1}}$. I averaged the spectra and used the average as a template for cross-correlation with the 200 phase-binned spectra. The refined result was (0, 210) $\mathrm{km\,s^{-1}}$. This location in velocity coordinates coincides fairly well with the centre of the irradiated region on the mass donor's surface (see Section 3.2.4.6).

I tried to identify the peaks observed after removing the resulting sinusoidal velocity. Several of the peaks seem to match Fe II lines, which leads us to think

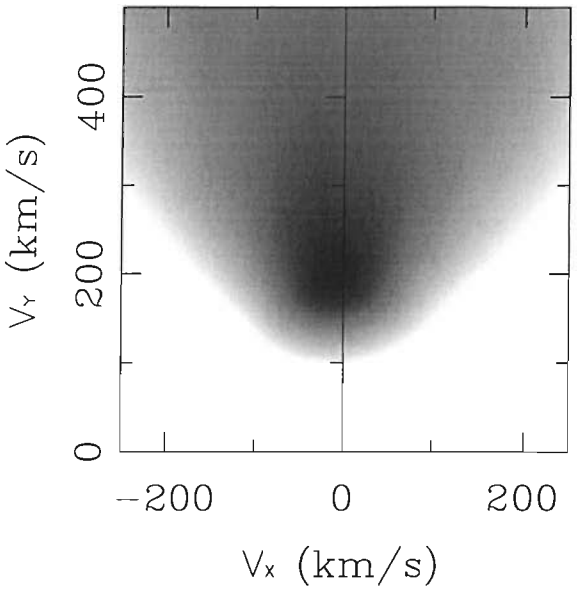

Figure 3.11: Skew-map for the continuum of U Gem.

that they are produced by irradiation of the mass donor.

3.2.3.4 Bright spot signature

The final new feature of the data is seen in the trailed spectrum of He II (Fig. 3.5). This line, which cannot be seen in the average spectrum, Fig. 3.2, as it is extremely weak, has no visible disc contribution at all, but does have an 'S'-wave. The remarkable feature is the complex structure of the 'S'-wave with a broad but also a very narrow component. I discuss these in Section 3.2.4.1 after I present Doppler maps of the data.

3.2.3.5 Flaring

The light curves discussed in Section 3.2.2 reveal some flaring, more conspicuous in H $\beta$and Fe II. I looked for matches of this behaviour in the trailed spectra, finding particularly good correspondence in the case of Balmer lines. The features are also stronger at high velocities. This indicates that the inner accretion disc is the likely source. I found no clear indication of these flares in He II or He I .

3.2.4 Doppler tomography

To understand the features present in the trailed spectra, I used Doppler tomography to study the emission lines. This technique combines all the information observed in the trailed spectra and generates a representation of the system in velocity coordinates. Due to the current lack of understanding of how the system's velocity coordinates should be translated to position coordinates, it is not possible to get a direct picture of the binary star, and so the interpretation is carried out in velocity coordinates. Though uncertain, this allows a visual separation of the contributions from different parts of the binary star (e.g. the mass donor, the bright spot, the accretion disc, etc.), and permits comparison with theoretical predictions under some rough assumptions (e.g. Keplerian regime). For a thorough presentation of the subject see Marsh & Horne (1988).

In Fig. 3.12 I present the tomograms for the 2001 dataset. From top to bottom the rows show:

1. The Doppler tomograms.
2. The observed spectra from which the tomograms were computed.
3. Data computed from the tomograms.
4. The tomograms after the symmetrical part around $(0,-107.1)\,\mathrm{km\,s^{-1}}$ was subtracted.

The velocity scales are relative to the line centres. All grey scales start from zero with uppermost levels chosen to improve the visualization of details. With the exception of the third row (from top to bottom), which is evenly saturated at 90% of the peak flux, the first column is saturated at 50%, the second at 80%, the third at 60%, the fourth at 80% and the fifth at 70%. See also Figure 3.13 for correspondence between the features observed in Doppler maps and in trailed spectra.

The spectra taken during eclipse were excluded from the computation of the maps, but they were included as a template for the calculation of fits from the tomograms. I plotted the outline of the Roche lobe of the mass donor over the tomograms. This was calculated by assuming $K_1 = 107.1\,\mathrm{km\,s^{-1}}$ and $K_2 = 294.7\,\mathrm{km\,s^{-1}}$ (Long &

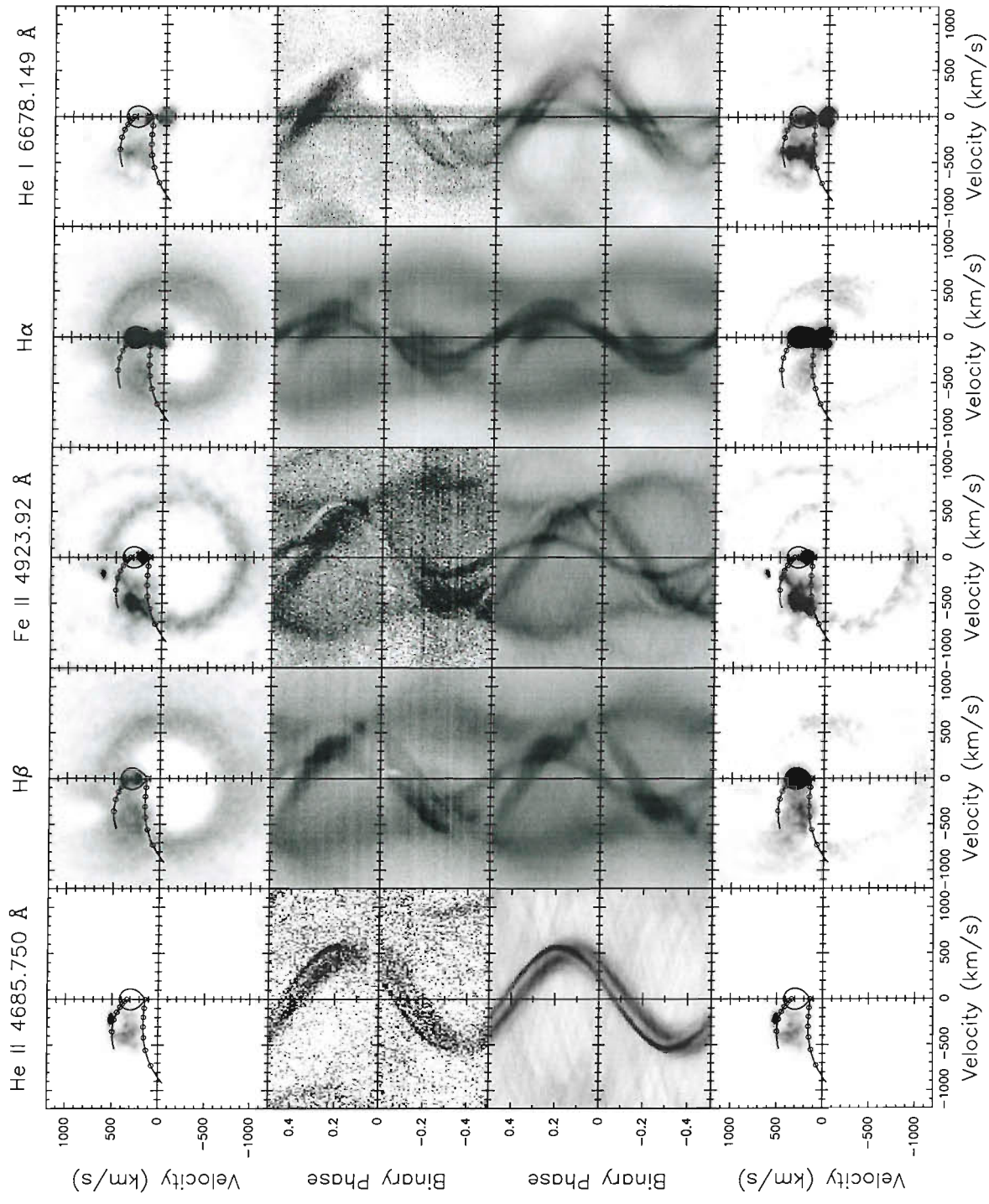

Figure 3.12: Doppler tomography.

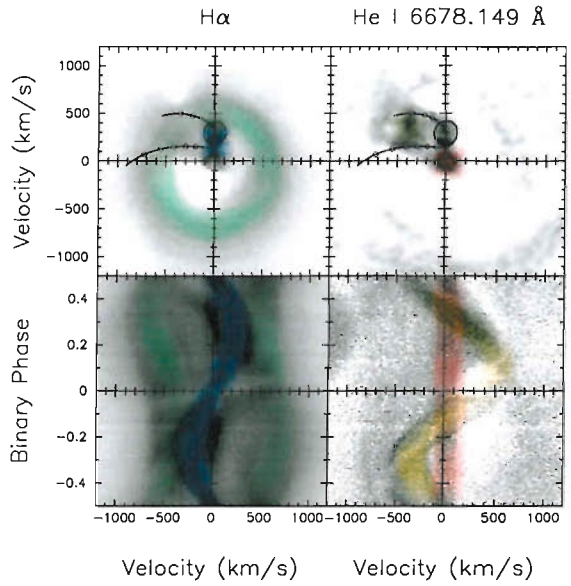

Figure 3.13: Correspondence of Doppler tomograms and trailed spectra. The colour code is as follows: orange, bright spot; red, low-velocity emission; green, accretion disc; blue, mass donor.

Gilliland 1999; Friend et al. 1990). I have already explained why K_1 is a good assumption. K_2 is a combination of the two published values (Wade 1981; Friend et al. 1990), which are consistent with each other.

I use the ephemeris of Marsh et al. (1990) updated from a recent measurement of the radial velocity of the red star (Naylor, private communication) so that zero phase occurs at TDB = 2451914.623811 ± 0.000012. This implies a correction of 0.005 in orbital phase to Marsh et al.'s (1990) ephemeris, which means the tomograms are rotated by 1.8° counterclockwise with respect to the orientation imposed by the old ephemeris.

I plot two velocity trajectories. The lowest of the two is the velocity of a ballistic gas stream. The upper one is the velocity of the disc, assuming a keplerian field for it, at positions along the stream. The distance to the white dwarf is marked on these paths by small circles at intervals of 0.1 times the distance of the inner Lagrangian point (R_{L1}). Each trajectory is plotted from $1.0R_{L1}$ to $0.3R_{L1}$ (leftmost value).

As expected from the analysis of the trailed spectra, neither the disc nor the mass donor is detected in the He II tomogram but the bright spot is resolved with

uncommon clarity. In He I the disc is almost undetectable, but both the mass donor and the bright spot have strong emission. Additionally, the He I and H α tomograms show a blob of emission around the centre of mass of the system, the tomographic equivalent of the "low velocity emission".

Both the disc and the mass donor are clearly seen in H α, H β and Fe II, the bright spot appearing with varying degrees of strength. The presence of the mass donor in these tomograms is used later for a study of disc shielding (Section 3.2.4.6).

The tomogram for Fe II displays two extra features. First, rather like He II, there is a very sharp spot seen above the path of keplerian disc velocities. Immediately below this spot there is a low region. I believe that this corresponds to the absorption line 'S'-wave seen in the trailed spectrum of this line (Fig. 3.12). It seems likely that this is the absorption equivalent of the sharp emission seen in He II. However, because this is only seen clearly over a very restricted range of phases (0.15 to 0.45), the emission spot has appeared to give a phase modulation – in other words it is likely to be an artifact and its displacement from the He II emission spot is probably not significant. I conclude that both the He II emission and Fe II absorption come from the same well-defined structure associated with the gas stream impact. The apparent spiral seen in the upper-right quadrant of the Fe II map is possibly caused by the contamination from a nearby line which can be seen on the right-hand side of the trailed spectrum.

The bottom row in Figure 3.12 shows the tomograms after I subtracted the symmetrical part around $(0,-107.1)\,\mathrm{km\,s^{-1}}$. Even after discarding the possible contamination in Fe II, we still see spiral structure in this map, and also in H α and H β. This is further discussed in Section 3.2.4.5.

3.2.4.1 Location of the bright spot

The Doppler map for He II reveals a sharp bright spot close to the velocities predicted for a keplerian disc along the path of the gas stream. In addition, a diffuse blob of emission is observed around the line connecting the sharp feature to the matching spatial point that has the velocity predicted for the stream (see Figure 3.14). This point seems to be located at $\sim 0.5 R_{L1}$. The presence of the blob of emission strongly suggests that a mixture of velocities could coexist in the bright spot, the stream

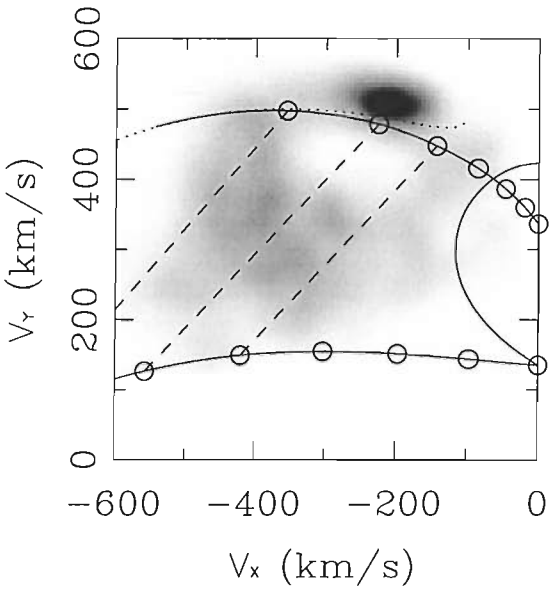

Figure 3.14: This is a closer view of the He II tomogram. The dashed lines connects the velocity of the ballistic gas stream (black lower trajectory) and the velocity on the keplerian disc along the gas stream (black upper trajectory) for the same points at distances of 0.4, 0.5 and 0.6 R_{L1} to the white dwarf (right to left). For the dotted trajectory see text.

adjusting to the velocities on the outer zones of the keplerian disc (already noted by Marsh et al. 1990). The value $\sim 0.5 R_{L1}$ (0.3 in units of the orbital separation a) is consistent with observations by Smak (1984) and is smaller than the radius of the tidally limited accretion disc (0.44a, see Warner 1995). Assuming that the position of the bright spot did not change significantly during the observations, I can use the sharp feature to estimate the bright spot's azimuthal location by treating the gas stream/disc impact point as a point co-rotating in the manner of a rigid body with the system. I conclude that the bright spot is face-on when the system reaches phase ~ 0.95, which is compatible with previous results obtained from reconstructed light curves (e.g. Smak 1971).

The fit between the sharp feature and the predicted path is not perfect, so I turn my attention to possible causes. The path for the keplerian disc velocities changes with K_2, so one possibility is that a better value of K_2 is needed, the problem being that measurements of K_2 are affected by irradiation and the corrections needed are not entirely certain (Friend et al. 1990). I calculate that $K_2 \sim 315\,\mathrm{km\,s^{-1}}$ produces a good fit, not much higher than the published values for K_2 ($283 \pm 15\,\mathrm{km\,s^{-1}}$, Wade 1981; $298 \pm 9\,\mathrm{km\,s^{-1}}$, Friend et al. 1990). Still, it is worth considering other possible

causes.

The predicted stream path is based upon circular, keplerian orbits within the disc. However, the disc should be distorted by 3-body effects, especially in its outer regions (Paczynski 1977). I therefore also computed the velocity of the keplerian disc along the path of the stream allowing for such effects. The results are plotted as the dotted line in Fig. 3.14, extending as far as the largest non-intersecting orbit at $\sim 0.6 R_{L1}$. At radii smaller than $\sim 0.4 R_{L1}$ the three body effects are negligible, but they do alter the predicted velocities in the right direction, although not by enough on their own. Now however, K_2 need only be $\sim 308\,\mathrm{km\,s^{-1}}$ to fit, which is compatible with Wade's and Friend et al.'s measurements.

Perhaps the most obvious and remarkable feature of this spot of emission is how narrow it is, being unresolved even at the resolution of $R \approx 10{,}000$. This, and the close match to the keplerian disc velocity along the stream, suggests that it must come from the disc immediately prior to the stream/disk impact region. It could only do so by irradiation from the main impact site. Somehow this does not give a corresponding feature at the ballistic stream velocity, possibly because of the lower density of the stream.

By contrast with the narrow spot of He II, all maps show a more diffuse feature which lies between the two predicted paths in the Doppler maps. As tomograms are velocity maps, sharing a location in a tomogram does not necessarily mean being in the same location in position space, so the interpretation of this broader feature must be done carefully. Marsh et al. (1990) ascribed this emission to the post-impact flow, with gas taking a velocity intermediate between that of the ballistic stream and the keplerian disc. The extraordinary feature of this emission, which was not clear at the lower resolution of Marsh et al.'s study, is that it appears to extend all the way to the secondary star (Fig. 3.12), which should not be possible because it would require the disc to extend well beyond its tidal radius. There is a similar extension to high velocities which I will return to later. I do not feel able to provide an explanation for either of these features.

3.2.4.2 Low velocity emission

In Hα and He I we see emission at low, possibly zero, velocity. In the case of Hα this emission is oddly asymmetric, displaying an elongated crescent-moon (Fig. 3.12) partly surrounding the side of the centre of mass closer to the mass donor. After subtracting the symmetrical part around (0,$-$107.1) km s^{-1} from the tomogram, the blob reveals again a crescent shape. It is worth mentioning that North et al. (2001) found a similar shape in V426 Oph's low velocity emission.

Similar low velocity emission has been reported for other systems as well. A summary of such reports is given in Table 3.1. The feature is puzzling because I find no reason for any component of the system to be at rest near the centre of mass, unless q has a extreme value, as it is the case of GP Com in which q=0.02 allows one to make the case for the white dwarf to be responsible for the emission (a claim that Morales-Rueda et al. (2003) support by convincing spectroscopic evidence). A clue to the mystery could be the fact that in all the other cases the emission is seen either at the centre of mass or a bit displaced towards the mass donor, but not otherwise. Steeghs et al. (1996) suggested that the emission was from gas that originated in the mass donor, but trapped in a prominence produced by a combination of magnetic, gravitational and centrifugal forces within the rotating binary system. The prominence would then be irradiated by the compact object and the disc, allowing its detection as a component co-rotating as a rigid body with the mass donor.

These "slingshot prominences", if similar to the prominences observed in single stars, could be located up to several radii from the magnetic star (e.g. Collier Cameron et al. 1990) but, if the prominence behaves like the ones we observe on the Sun and rapidly rotating stars (see Collier Cameron et al. 1999), I would expect them to be short-lived; in that case four nights should perhaps have shown some variation either in flux or in size, whereas in my data the feature is consistent from night to night. On the other hand, there is evidence from AB Dor (Collier Cameron et al. 1989) which suggests that loops on single stars can evolve in timescales of 2-4 days. It may therefore be reasonable then that, under certain conditions, prominences can last this long in members of binary systems too.

Table 3.1: Summary of known Doppler tomographic reports of low velocity emission. Under 'State', Q means 'quiescence', O means 'outburst', and NA means 'not applicable'. Other shorts used here are WD for 'white dwarf' and S1996 for 'Steeghs et al. (1996)'.

System	State	Lines	Suggested source	Reference
IP Peg	O	H α	Irradiated slingshot prominences	S1996
SS Cyg	O	Balmer, He I , He II	Irradiated slingshot prominences	S1996
AM Her	NA	SI IV 1394Å, NV 1239Å	As in S1996	Gänsicke et al. (1998)
GP Com	NA	He I , He II	WD (Morales-Rueda et al. 2003)	Marsh (1999)
V426 Oph	Q	H α	As in S1996	North et al.(2001)
U Gem	Q	H α, He I	As in S1996	This paper

3.2.4.3 Other features

In both H α and H β a clear absorption feature is observed prior to eclipse. The feature was constantly present during the four nights of observation in 2001, but it is not obvious in the 1990 H α data. It appears roughly between phases 0.91 to 0.98. I attempted to trace the motion of the feature but, due to the small orbital range on which it appears, my results are not reliable. It is even difficult to conclude whether it moves at all or is rather a feature at rest in the centre of mass of the system.

The Fe II trailed spectra reveals half an 'S'-wave of absorption with approximately the same amplitude as the sharp emission in the He II trailed spectra. Also in H α, He I and specially H β this absorption might be present, although it is rather diffuse.

Finally, again in Section 3.2.2, I have mentioned the presence of a hump in the light curve of He I and perhaps some other lines as well. This hump peaks around phase $\sim$0.3.

3.2.4.4 Stream-disc overflow?

With high signal-to-noise ratio and smooth disc profiles, my data are well suited to detection of stream material overflowing the disc. If it does so, it is predicted to end in a second impact, at a point near to the closest approach of the stream to the white dwarf (Livio et al. 1986; Armitage & Livio 1998). Kunze et al. (2001) specifically simulated U Gem amongst other systems, and found that more than half the stream overflowed the disc. Using the tables in Lubow (1989), we would expect the second impact to occur at $\sim 0.13\,R_{\rm L1}$, with excess emission to be expected along the path of the stream.

There is no evidence at all of any stream overflow in the data on U Gem. This can first be appreciated from the Doppler maps of Fig. 3.12. To search more rigorously, we need to subtract the smooth background from the disc. I implemented an elliptical isophote fitting procedure to do this. That this is needed is not obvious from the standard tomograms, but is clear from the radius/azimuth version shown in Fig. 3.15: here the ellipticity of the isophotes shows up as a quasi-sinusoidal isophote contours. The procedure I developed to subtract the elliptical continuum

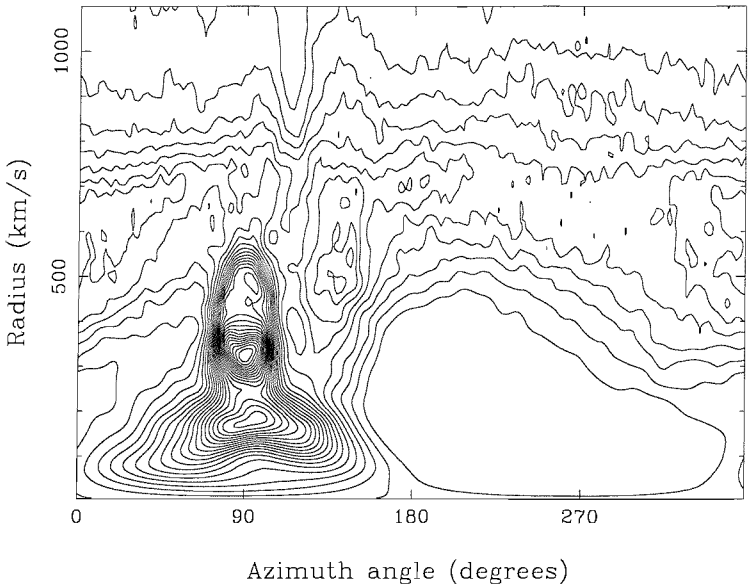

Figure 3.15: The Hα tomogram re-projected and contoured to show some isophotic levels. The radius is measured from (0, -107.1) km s^{-1}, and the azimuth angle is counted counterclockwise from the positive abscissa. If the isophotes were circular, we would see them as horizontal lines in this diagram. Instead, the contours follow the curved paths expected for elliptical isophotes.

is described in Appendix A. After performing the subtraction I obtained the tomograms seen in Fig. 3.16, which are scaled to only 3% of the peak height of the raw tomograms. There is no evidence of stream-disc overflow along the path of the stream even at this low level, suggesting that the physics put into the simulations that predict extensive stream-overflow is probably lacking in some important respect.

Fig. 3.16 does show an excess extending up and to the left of the main disc/stream impact region to well over 1000 km s^{-1}. A similar effect was seen in EX Dra (Billington & Marsh 1996) who suggested that non-kinematic broadening, such as Stark broadening, could be responsible. Whatever the explanation, this emission, although weak, will clearly have a bad effect on K_1 determination.

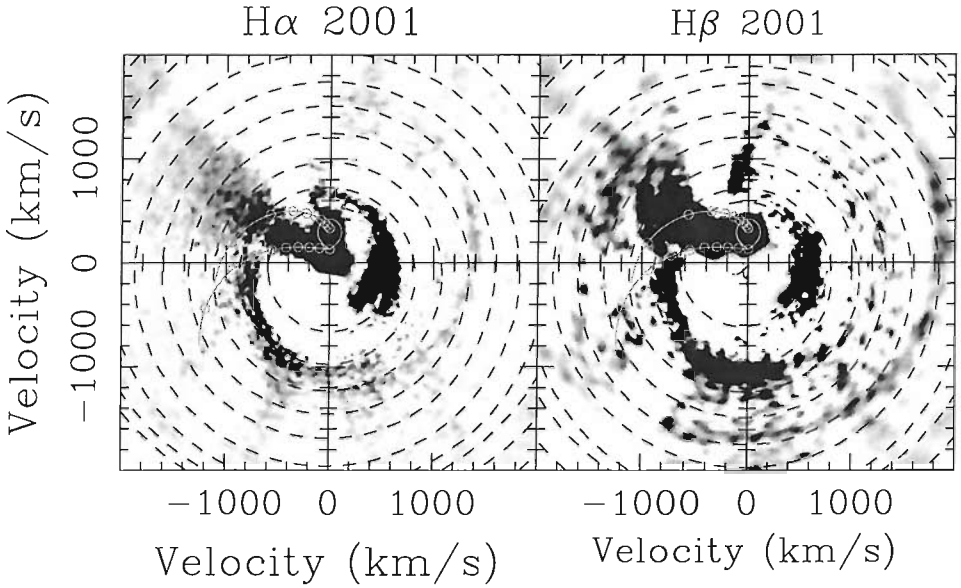

Figure 3.16: H α and H β tomograms after subtraction of an elliptical background. The ellipses used to interpolate the background are plotted with dashed lines. The grey solid lines are the keplerian disc and ballistic stream velocities for the stream path. It extends from 1.0 to $0.15R_{L1}$. The tomogram is saturated at 3 per cent of the maximum level.

3.2.4.5 Spiral shocks in quiescence

Figure 3.16 reveals the presence of spiral structure near the level of the continuum. This spiral structure has been previously reported for U Gem in outburst (Groot 2001), making it one of a handful of systems in which the phenomenon is detected. So far this phenomenon has never been reported during the quiescent state of any system. The phenomenon has been considered to be evidence of "spiral shocks" (Steeghs, Harlaftis & Horne 1998), which had been predicted in simulations of accretion discs (see Matsuda et al. 2000 for a review).

One problem with this interpretation is that it requires the presence of large or unusually hot discs. This prompted Smak (2001) and Ogilvie (2002) to propose alternatives to the spiral shocks to explain the phenomenon. Their idea was that the spiral features revealed by Doppler tomography could be explained as the consequence of 3-body effects (Paczynski 1977). Ogilvie went further to extend the model of Paczynski from 2 to 3 dimensions, allowing for a complete set of physical conditions in his model. He concluded that, due to tidal distortions, some regions of the disc would thicken, and then be irradiated by the white dwarf and inner disc.

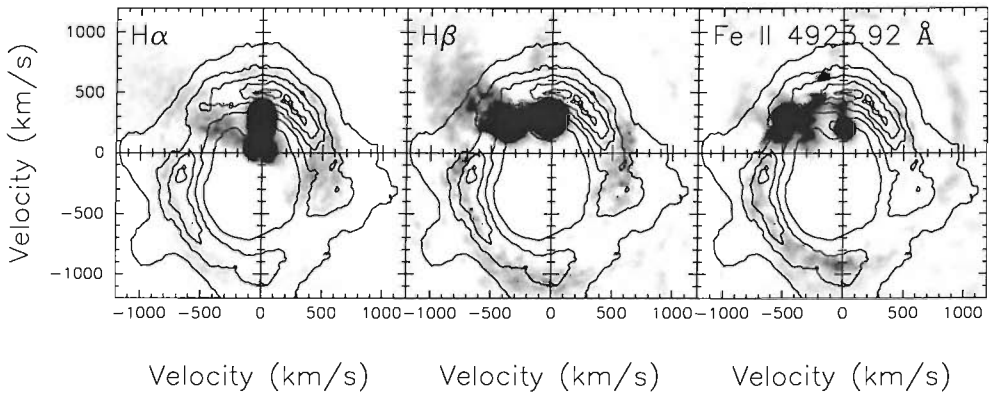

Figure 3.17: The tomograms for Balmer lines and Fe II tomograms after the symmetrical part around (0,-107.1) km s^{-1} is subtracted are plotted in this figure. The tomograms are saturated at 20 per cent of peak level. Superimposed on these tomograms I display isophotes (at 10, 30, 50, 70 and 90 per cent of the peak level) from a tomogram based on outburst observations of U Gem (Steeghs, Morales-Rueda & Groot, in preparation).

The pattern of thickening would be slightly spiral, but no waves or shocks would be involved in the process. In Doppler tomography the pattern would show up as the kind of open spiral seen in published tomograms.

Between the two competing explanations there is one possible test. As said above, the spiral shocks require a hot or a large disc to be present. This implies that the spirals would not be present during quiescence or, if present, they would be substantially different from the outburst spirals. In particular the model predicts tightly wounded up spirals for a cool and small disc. Both conditions are expected to be achieved during quiescence, and thus observations during this state are critical to evaluate the validity of the theory. The observations were taken during the quiescent state of U Gem and, as it is possible to see in Figure 3.17, we can detect weak spiral structure. To ensure that my spirals were not an artifact produced by a wrong selection of the centre of symmetry (i.e. of K_1), I took the precaution of producing Figure 3.17 in several versions, changing the assumed value for K_1 from 90 to 120 km s^{-1} without observing significant variations in the achieved shape and location of the spirals.

It should be noted that the spirals I find here are at a low level and are not related to the structures claimed by Neustroev and Borisov (1998) in U Gem. Their data shows pronounced asymmetries, but were taken with poor spectral and phase

resolution, and most importantly, without complete orbital coverage. The raw maps (e.g. Fig. 3.12) are very symmetric. I believe their claim of fairly strong spiral structure to be incorrect, and a result of the difficulty of interpreting the complex variations of U Gem with inadequate orbital coverage.

These quiescent spirals are no more wound up than the spirals previously seen in the outburst of U Gem (personal communication used in Figure 3.17, and also see Steeghs et al. 1998).

The match between the outburst and quiescent spirals is not perfect, but it is known that the spiral structure changes throughout an outburst. Thus, a qualitative comparison is what matters here. The key points to consider are that the quiescent spirals appear in the same region as the outburst ones, and that the structure shows large opening angles instead of being tightly wound as we would expect if it was produced by shocks. Although this result gives some support to Ogilvie's model, we still cannot discard the theory of shocks in favour of a pure geometrical explanation. As said above, I am pretty certain that the disc is cool during quiescence. However, simulations show that the opening angle of the spirals correlate with disc radius (Danny Steeghs, personal communication) so that a cool but large enough disc could still display open spirals. Could this be the case in U Gem? Unfortunately, the literature does not provide a clear description of the relation between disc size and opening angle of the spirals in simulations, and thus a direct comparison with U Gem is not possible. On the other hand, comparing with simulations published for other systems (e.g. Steeghs & Stehle 1999, for a system with $q = 0.3$) I observe that for a radius of $\sim$0.5a the effect of such a correlation seems to be unimportant and tightly-wound spirals are expected. I estimate the size of U Gem's quiescent disc during the observations as $\sim$0.3a (Section 3.2.4.1). Smak (1984) has shown that U Gem's disc varies from $\sim$0.28a to $\sim$0.40a, so the quiescent spirals were produced with the disc near its minimum radius. A literature search revealed that simulations (Steeghs & Stehle 1999, Makita et al. 2000, Matsuda et al. 2000) seem to support unanimously the idea that open spirals require a large and hot disc; therefore, I do not favour the idea of shocks during quiescence. Still, they could indeed play a role during outburst and some form of independent test should be devised to confirm this.

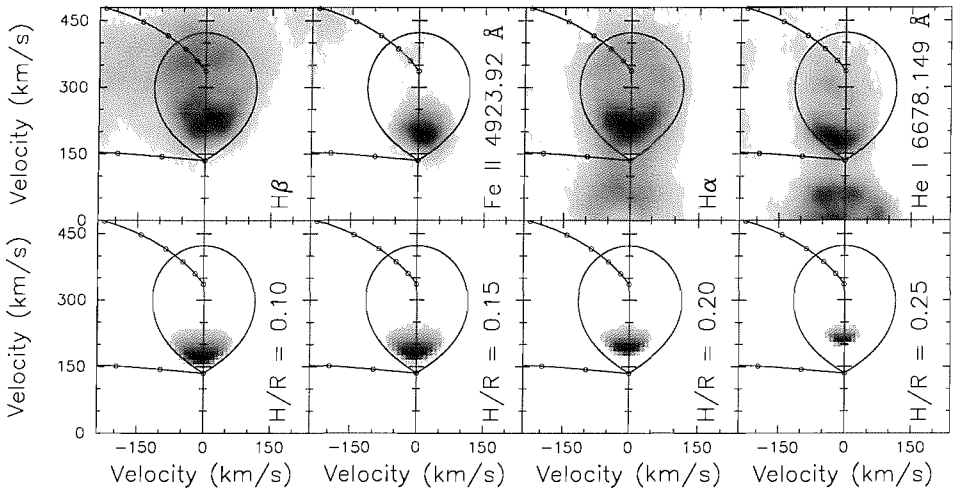

Figure 3.18: Real and simulated disc shielding. The top row is a close view of those tomograms where the mass donor is resolved. The lower portion of the Roche lobe is not fully irradiated, which is explained by shielding of the mass donor's equatorial regions due to an effective height of the disc's outer rim. The bottom row shows simulations for different H/R ratios. All the images are saturated at 100 per cent, the colour scales starting at zero flux. See text for details.

3.2.4.6 Disc shielding

A notable feature of the Fe II tomogram is the definition of the mass donor's irradiated face. This map, and also the H α, H β and He I tomograms, make it possible to quantify the disc shielding on the system, as shown in Figure 3.18. On the top row I zoom in on the Roche lobe of the mass donor. The light from the white dwarf and the inner disc that irradiates the mass donor is partially blocked in the equatorial regions of the mass donor. This blockage is caused by the outer rim of the disc having a geometrical or effective height (Harlaftis 1999; Morales-Rueda et al. 2000). In the bottom row I show simulated tomograms (not including noise) for a system with the same parameters of U Gem but with varying height-to-radius ratio (H/R) in the disc. I included some broadening in the simulations by convolving the synthetic datasets with a gaussian with FWHM 15 km s^{-1}. The simulations used a simple physics, irradiation being proportional to flux ($f = \frac{L}{4\pi d^2}$) from the white dwarf. Roche lobe geometry was used for calculation of the mass donor's shape. A region on the mass donor's surface was calculated as irradiated whenever there was a clean path between that region and the white dwarf.

Values of H/R from 0.10 to 0.25 were considered (increasing by 0.05 each time). For $H/R > 0.30$, the height completely prevents the irradiation to take place.

Comparing the simulations with the actual tomograms, I estimate that the H/R ratio for U Gem is somewhere between 0.15 and 0.20. It could be less than this if K_2 is larger than we have supposed, as suggested by the sharp spot in HeII (section 3.2.4.1). However, the values calculated here agree well with values obtained from simulations of vertical structure of accretion discs (Gawryszczak & Rozyczka 2003; Hirose et al. 1991).

3.2.5 Inclination angle

Zhang & Robinson (1987) derived an orbital inclination angle $i = 69.7°$ for U Gem from a detailed lightcurve fitting model. Other estimates of i have displayed a trend to somewhat smaller values, but mainly in the region of $65° < i < 70°$. However, in the absence of a white dwarf eclipse, the orbital inclination is rather poorly constrained by photometry alone.

In this section I use the eclipse of the emission lines, and specifically the highest velocity in the lines that is eclipsed to constrain the orbital inclination. Figure 3.19 shows simulated and real data. The top panel shows a simulated trailed spectra when i is set to 69.7°, with K_1 and K_2 set to the values declared before. The three central panels show real data after a constant fit to each column was subtracted from every image. The extension of the eclipse in these panels easily reaches 700 $\mathrm{km\,s^{-1}}$ while in the simulated data of the top panel it does not go beyond 550 $\mathrm{km\,s^{-1}}$. This hints at a larger value of i.

I used a trial and error approach to find a good match between the data and the predictions from a model considering full Roche geometry. Adopting the value $\sim$ 700 $\mathrm{km\,s^{-1}}$ for the extension of the eclipse, the outcome of the procedure is $i \sim 72°$. The simulated data displayed in the bottom panel of Figure 3.19 shows that this value produces a good agreement with the actual data.

In Appendix B I include an approximate analytic treatment of this same problem, in good agreement with the answer provided by the full Roche geometry solution.

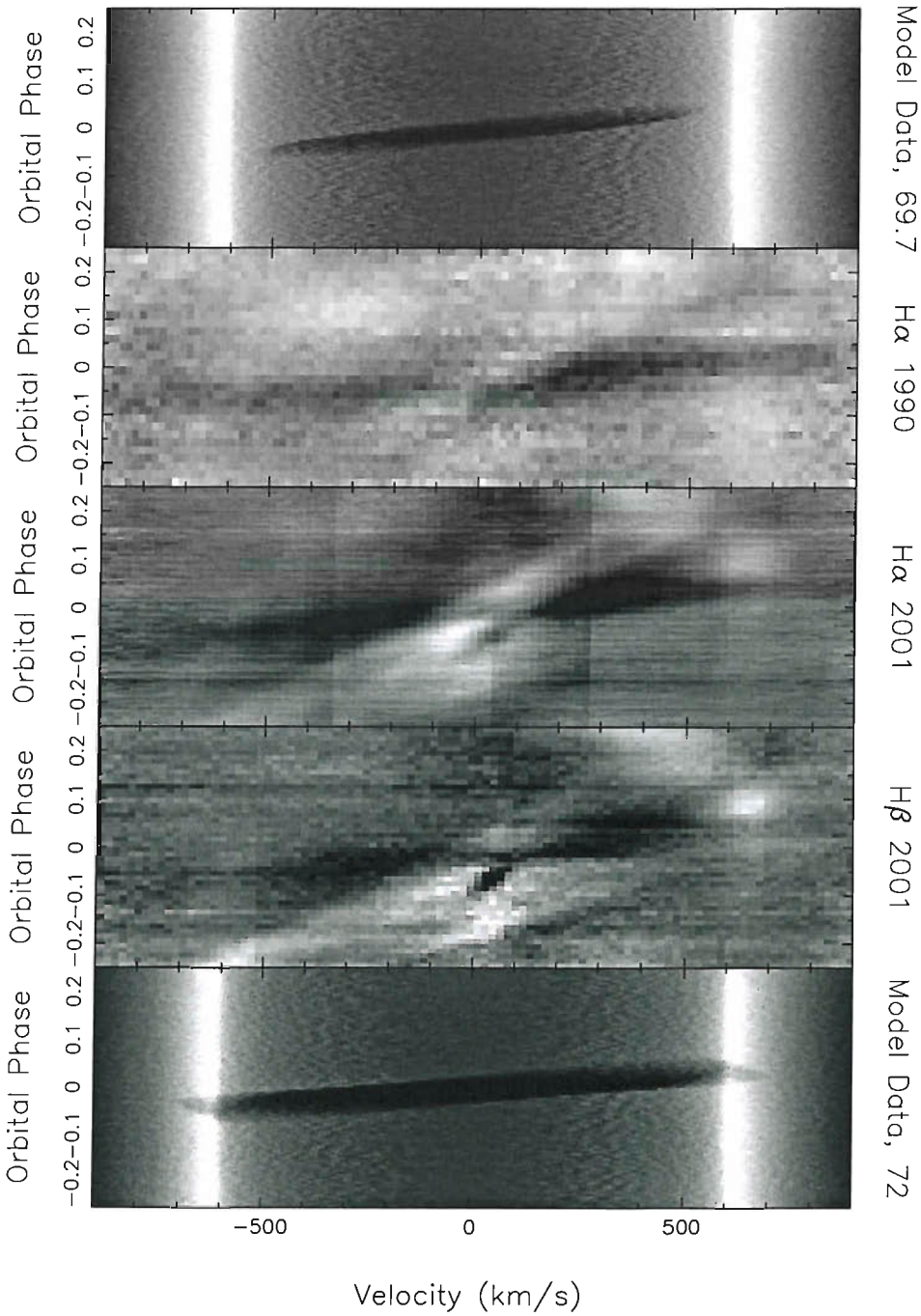

Figure 3.19: The top and bottom panel show simulated data for 69.7° and 72° respectively. The central panels show data from the Balmer lines in 1990 and 2001. The central panels were processed to improve visibility of the extension of the eclipse (see text for details). All the panels are saturated at 100 per cent.

3.2.6 Velocity of the white dwarf

As I already mentioned in the introduction, the value of K_1 for U Gem is known accurately, thanks to a direct observation of metal lines from the white dwarf's surface (Long & Gilliland, 1999). The result, 107.1 ± 2.1 km s^{-1}, can be used to test the effectiveness of the techniques already in use, which are mostly based on assuming that the emission lines originated on the accretion disc will provide information from which the motion of the white dwarf can be tracked.

I concerned myself with two traditional techniques to measure K_1: the diagnostic diagram (Shafter, Szkody & Thorstensen 1986) and the light-centre diagram (Marsh 1988), both of which commonly use the double-gaussian method (Schneider & Young 1980) to measure the radial velocities from a dataset.

The double-gaussian method is by now the standard way of measuring the line centre of a line profile. It requires solving the equation:

$$\int S(\Lambda)G(\lambda - \Lambda)d\Lambda = 0 \tag{3.1}$$

where $S(\Lambda)$ is the spectral profile and:

$$G(x) = exp(-(x-a)^2/2\sigma^2) - exp(-(x+a)^2/2\sigma^2) \tag{3.2}$$

with a the separation of the two gaussians included in $G(x)$, and σ the width of each gaussian. The results are strongly dependent on a, and thus it is common to calculate a set of results for a range of different values of a. Then, either the diagnostic diagram or the light-centre method are used to extract reliable kinematic information from these sets.

The diagnostic diagram is a technique to select a value for K_1 from a series of values obtained via the double-gaussian method for a range of different a. For each a one has a table of values of ϕ (orbital phase) and V (velocity). Then one fits:

$$V = \gamma - K\sin(2\pi(\phi - \phi_0)) \tag{3.3}$$

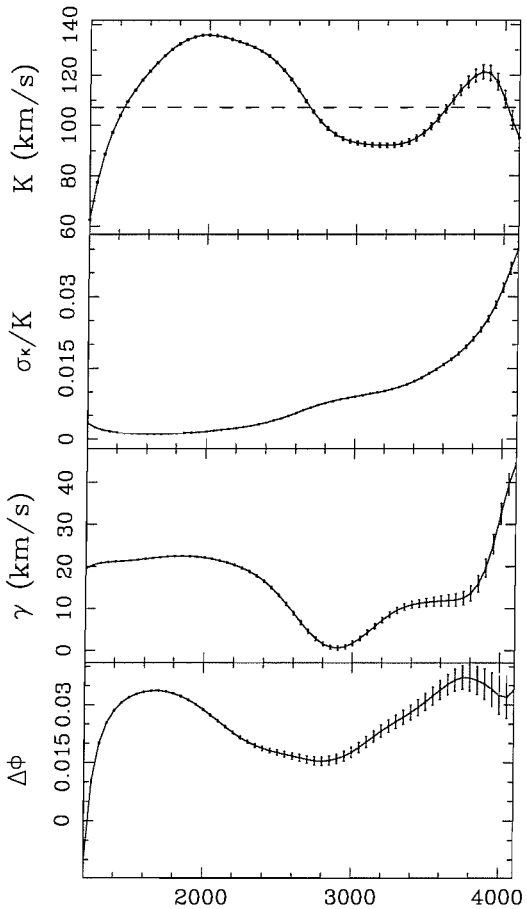

Figure 3.20: The diagnostic diagram for H α in 2001. A separation of gaussians equal to $\sim$ 3400 km s^{-1} seems appropriate to avoid most of the jump in noise close to 4000 km s^{-1} in the σ_K/K plot. This separation corresponds to a plateau in the K plot, from which the value $\sim$ 95 km s^{-1} is read for K_1. The dashed horizontal line in the top panel marks the level 107.1 km s^{-1}. Long & Gilliland's value for γ is off the plot.

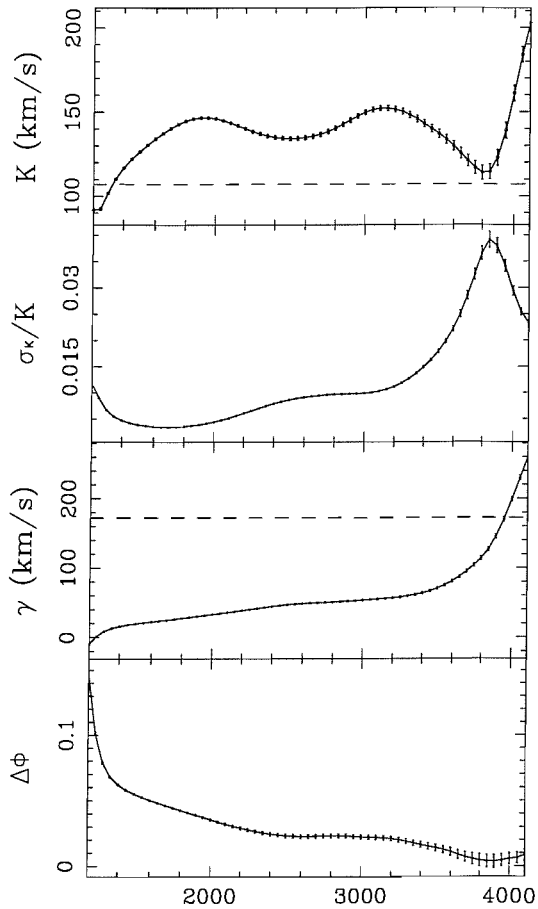

Figure 3.21: The diagnostic diagram for H β in 2001. A separation of 3000 or 3200 km s^{-1} seems appropriate in this case. This points to a value of 150 km s^{-1} for K_1. The dashed horizontal line in the top panel marks the level 107.1 km s^{-1}. The dashed horizontal line in the third panel (top to bottom) signals Long & Gilliland's value for γ (172 ± 15 km s^{-1})

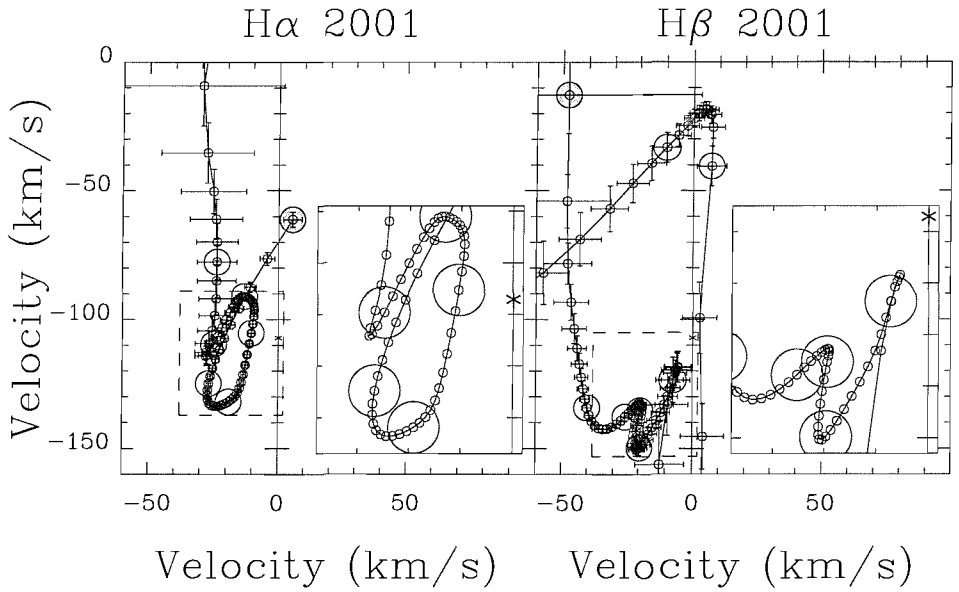

Figure 3.22: The result of applying the new method to the 2001 H α and H β datasets. See text for details of how to read the plots. A certain trend of the points in direction to (0,107.1) km s^{-1} is seen twice in the H β plot. H α shows no clear trend towards (0,107.1) km s^{-1}.

and plots K, the fractional error σ_K/K, γ and ϕ_0 against a. If the emission is dominated by the accretion disc, it is expected that K will asymptotically approach the value of K_1 and that ϕ will asymptotically approach ϕ_0 when a is large. But when a is large the noise picked by the pair of gaussians increases and the measurements are less reliable. The prescription of the diagnostic diagram is to stop when σ_K/K is seen to increase abruptly.

When using the diagnostic diagram it often happens that σ_K/K gets unnaceptably large before any asymptotic behaviour is observed for either K or ϕ. The light-centre diagram aims to deal with this problem. Once again one fits Equation 3.3 but then the plots considers pairs $(-K\sin\phi_0, -K\cos\phi_0)$. Alternatively, this can be thought of as the fitting of the orbital solution:

$$V = \gamma - K_x \sin(2\pi\phi_0) + K_y \cos(2\pi\phi_0) \tag{3.4}$$

and subsequent plotting of (K_x, K_y). It is important to note that Equations 3.3 and 3.4 are equivalent. In the light-centre diagram one expects that the plotted points will signal a trend towards $(0, K_1)$ before starting to move erratically because

of the upsurge in noise. The value of K_1 is obtained then by extrapolation of the trend towards the vertical axis.

Figures 3.20 and 3.21 show the diagnostic diagram for Hα and Hβ 2001, after measuring radial velocities with the double-gaussian method. The results are respectively 95 and 150 km s^{-1}. The plots in the diagnostic diagrams display curves that behave only partially as expected. In particular there is no simultaneous convergence towards final values in the panels (compare, for instance, top and bottom panel of Figure 3.20).

The values for γ from Figures 3.20 and 3.21 are $\sim$ 10 km s^{-1} and $\sim$ 55 km s^{-1} respectively. These values, which include both the systemic velocity we are interested in and a gravitational redshift component due to the proximity to the white dwarf, are both far from Long & Gilliland's measurement (172 ± 15 km s^{-1}). It is interesting to note that for Hβ the result can be greatly improved by using simply the criterion of picking the γ value corresponding to the the highest σ_K/K ratio. However, the discrepancy with Hα would be difficult to explain, so I regard this just as a coincidence.

I recycled the radial velocities from the previous stage, this time using the light-centre method to analyse them. The plot obtained, not reproduced here, is very similar to Figure 3.22, which is described below. The main difference occurs for the smallest and largest values of the separation of gaussians, with the figure for the light-centre method displaying a more erratic behavior than the one seen in Figure 3.22. The region close to (0,-107.1) km s^{-1} is virtually identical.

Figure 3.22 shows the application of a new method for performing the analysis of radial velocities. The method is explained in detail in Appendix C, but it suffices to say that it combines in one process the measuring of radial velocities as directed by Schneider & Young (1980), and the fitting of an orbital solution for the construction of a light-centre diagram and is designed to be more robust in the presence of noise than if the two steps are carried out separately as is usually the case.

I used a small x to mark the point with coordinates (0,-107.1) km s^{-1}. The points in the diagrams are results for different separations of two gaussians with a FWHM of 100 km s^{-1}. The first separation is 1200 km s^{-1} and is marked with a large grey circle. Subsequent separations differ from each other by 100 km s^{-1} and are marked

with small circles. Every 500 km s^{-1} I plotted a large white circle centred on the small circle marking the point; this was done to facilitate the reading of the plot. In both panels an additional window with a closer view was added to highlight the region close to (0,-107.1) km s^{-1}. In the smaller windows I omitted the uncertainty bars.

The plot for Hα does not reveal a clear trend towards (0,-107.1) km s^{-1}, although it happens twice to a certain degree in Hβ. The points of closest approximation to (0,-107.1) km s^{-1} are (-10.5,-105.3) km s^{-1} in Hα for a separation of 2700 km s^{-1}, and (-5.4,-118.4) km s^{-1} in Hβ for a separation of 3850 km s^{-1}. Of course the problem remains that this would not be obvious were I not to know K_1 beforehand.

As said above, the comparison with the normal light-centre technique does not yield significant differences in this case. The new method is designed to be robust in the presence of noise by treating all spectra simultaneously rather than each one on its own. What it cannot do is to remove real asymmetries in the data such as are evident in Fig. 3.16. The extension of these asymmetries to very high velocity is a major problem for the emission line method for measuring K_1.

3.3 Summary of my findings

I have presented high spectral resolution and signal-to-noise optical spectra of U Gem with the aim of testing the use of the broad emission lines in tracing the motion of the accreting white dwarf in cataclysmic variable stars. U Gem is particularly suited to this task because the true motion of its white dwarf has been measured from *HST* spectra by Long & Gilliland (1999). My data reveal a number of subtle effects for which I can offer only tentative explanations. These include low velocity absorption and emission that I suggest imply the presence of prominences on the mass donor star. Judging by their duration, the physics underlying the presence of such prominences might be different to what we have learnt from single stars.

The comparison of performance of the techniques for measuring K_1 is disheartening. My observations are of high time and spectral resolution, and U Gem is one of the brightest dwarf novae, and has strong lines. Nevertheless, my measurements of K_1 range from 80 to $\sim$ 150 km s^{-1} and contain not a hint that the correct value

was the 107 $\mathrm{km\,s^{-1}}$ measured by Long & Gilliland (1999). Neither the diagnostic diagram (Shafter et al 1986) nor the light centre technique (Marsh 1988) were of any help. The root cause of the problem appears to be the bright-spot which causes an asymmetry that extends to large velocities in Doppler maps, violating the usual assumption of a trend towards symmetry at high velocity. Why this should be the case is not clear.

A search for disc asymmetries revealed, on one hand, that there is no evidence of stream overflow taking place in U Gem. On the other hand, I found interesting evidence of weak spiral structure on the disc, similar to what has been reported for the system during outburst. This is the first reliable detection of this kind of phenomena in quiescence and provides preliminary support for Ogilvie's and Smak's explanation for spiral structure.

I confirmed U Gem to have complex structure in the region of the gas stream/impact region. My data reveals extended emission that lies between the velocity expected for the ballistic gas stream directly and the velocity of the keplerian disc along the gas stream.

Further discussion of these findings is left to Chapter 6.

Chapter 4

GD 552

4.1 Introduction

GD 552 is a blue, high proper motion star (0.18″/yr) discovered by Giclas et al. (1970). It was first observed spectroscopically by Greenstein & Giclas (1978), who found that it is a cataclysmic variable star (CV). GD 552's proper motion and position close to the plane of the Galaxy (galactic latitude 4°), combined with its blue colour all suggest that it is relatively close by. Greenstein & Giclas (1978) suggest a distance of $\sim 70\,\mathrm{pc}$ which gives a transverse motion which is reasonable for a member of Galactic disk, and combined with its magnitude $V = 16.5$, suggests $M_V \sim 12.5$, the equivalent of a $0.6\,M_\odot$ white dwarf with a temperature of only 9000 K. The probable low luminosity of GD 552, which is of central importance to this chapter, is backed up by an absence of any observed outbursts, suggesting that it may very rarely or never have outbursts.

The main spectroscopic study of GD 552 so far has been carried out by Hessman & Hopp (1990) (hereafter HH1990) who determined the orbital period of GD 552 of 102.7 min. They observed an extreme Balmer decrement (H α:H β= 6.2:1.0), indicative of a cool, optically thin disc, another indication of low luminosity. HH1990 measured the white dwarf's projected orbital velocity to be $K_1 = 17 \pm 4\,\mathrm{km\,s^{-1}}$. This is a very low value suggestive of a low inclination system, since for edge-on systems with orbital periods similar to GD 552 K_1 is typically $\sim 60 - 80\,\mathrm{km\,s^{-1}}$. However,

the emission lines from the accretion disc seemed to suggest a moderately inclined system as they display clearly separated double-peaks (which come from the outer disc) with velocities of $\pm 450\,\mathrm{km\,s^{-1}}$ which can be compared to typical peak velocities of $\sim 600\,\mathrm{km\,s^{-1}}$ for edge-on systems. To solve this conundrum, HH1990 suggested that the white dwarf in GD 552 is unusually massive – close to the Chandrasekhar limit in fact – allowing a low orbital inclination ($\sim 20°$) and therefore the small K_1 value at the same time as large disc velocities. HH1990 were forced to their model because they assumed that the companion to the white dwarf had to be a main-sequence star. Since the companion fills its Roche lobe, Roche geometry and the orbital period uniquely specifies its density ($36.5\,\mathrm{g\,cm^{-3}}$), which, if it is a main-sequence star, also fixes its mass, which turns out to be $\sim 0.13\,M_\odot$, which would cause a much larger K_1 than observed, unless the inclination is low.

More recent theoretical work has revised HH1990's estimate a little to $\sim 0.15\,M_\odot$ for GD 552's orbital period (Kolb & Baraffe 1999), but the problem is qualitatively unchanged. However, this work also suggests a very different scenario. Cataclysmic variables at long orbital periods are thought to evolve towards shorter periods until they become degenerate at a period near 75 minutes. After this time, the mass donor increases in size as it loses mass and the orbital period lengthens (e.g. Howell, Nelson & Rappaport, 2001). Thus although if GD 552 is approaching the period minimum its donor mass must be $\sim 0.15\,M_\odot$, if it has already passed the minimum and is now evolving to longer periods, it would be about a factor of four times less massive, and there would be no need for HH1990's massive white dwarf, face-on model. Moreover, such a system would have an extremely low mass transfer rate, consistent with GD 552's lack of outbursts and probably low intrinsic luminosity. The evolution just described is the standard explanation for the observed minimum orbital periods of CVs, which however fails on two counts. First, the observed minimum around 80 mins is distinctly longer than the theoretical value of 70 min (Kolb & Baraffe 1999), and second while we expect most systems to have passed the period minimum there is not a single well-established example of such a system known. Therefore it is of considerable interest to establish whether GD 552 is a pre- or post-period-minimum system.

In this chapter I carry out a test to distinguish between these two models. If the pre-period-bounce model is correct, then we should be able to detect features from the M star. If, conversely, the post-period-bounce model is correct, the donor will

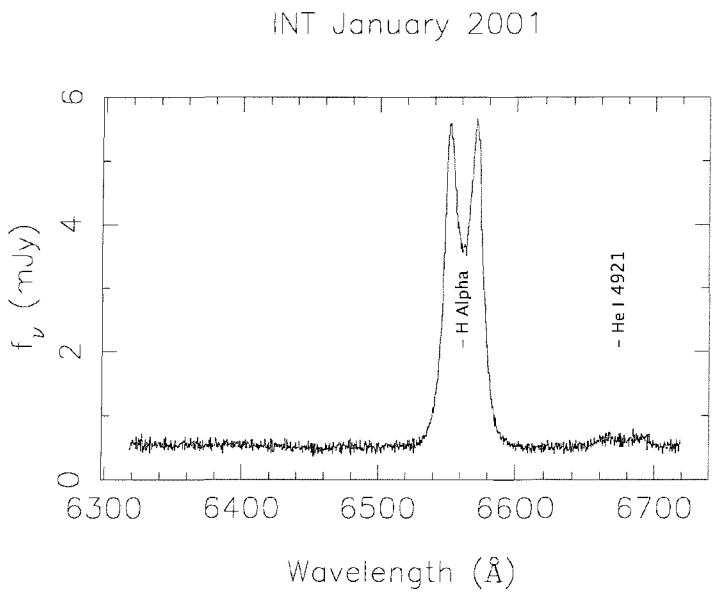

Figure 4.1: Average data.

be extremely faint and it should not be detectable. In summary, my task is to set the strongest possible limit upon the presence of a hypothetical M dwarf such that we can say that we would have seen it had GD 552 been a pre-bounce system.

4.2 Analysis

4.2.1 Average profiles and trailed spectra

Figures 4.1, 4.2, 4.3 and 4.4 display average spectra for my data. I observe double peaked profiles in all the detected lines: He I 4471.68 Å (hereafter He I 4471), He II 4685.750 Å (hereafter He II), He I 4921.93 Å (hereafter He I 4921), He I 6678.15 Å (hereafter He I 6678), O I 7773, O I 8446and the Paschen and Balmer series. For the red arm of the WHT August 2001 the complex of lines near $\sim$ 7600Å is my best attempt at tellurically correcting the data. In the general theory of CVs, the double peaked profiles are explained as the signature of a rotating accretion disc around a the accreting object in the system.

I measured the Balmer decrement from my averages, defined as the ratio of line intensities Hα : Hβ : Hγ. I did this by fitting a single gaussian to each profile after

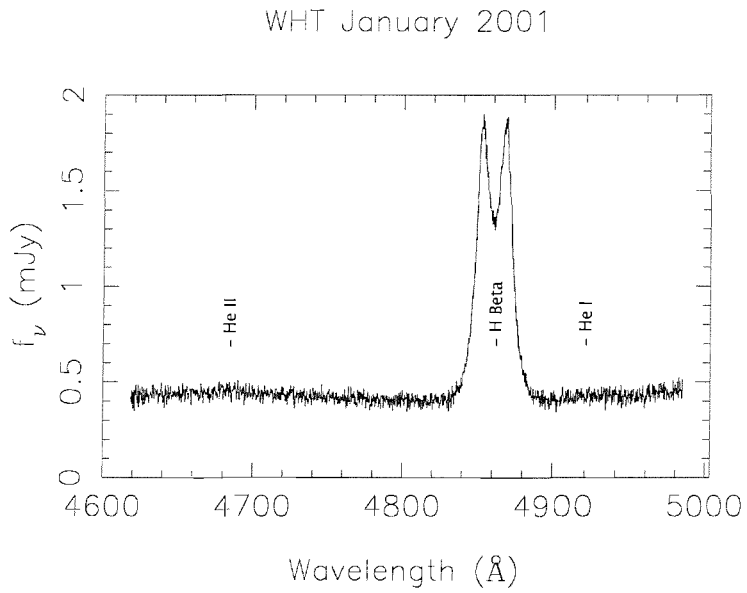

Figure 4.2: Average data.

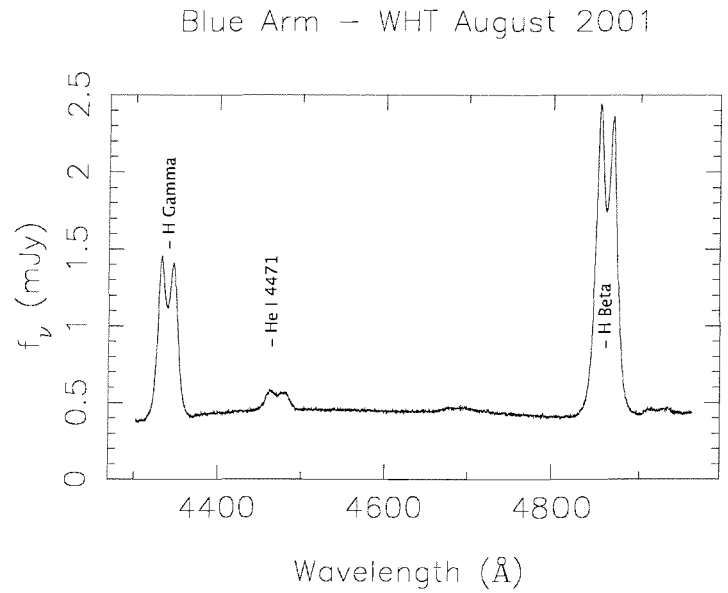

Figure 4.3: Average data.

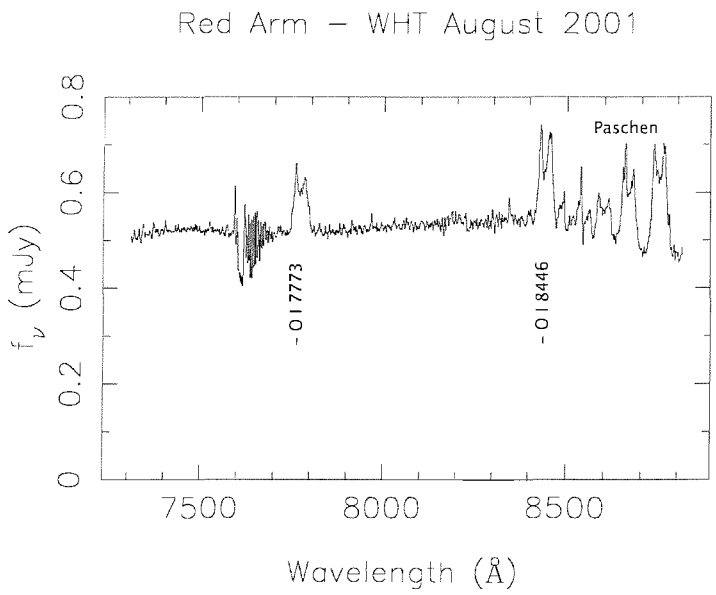

Figure 4.4: Average data.

subtracting a low order fit to the continua. Hβ is the only Balmer line for which I have two measurements (January and August 2001), and I find that my fits produce intensities that are not compatible with each other (1.296 ± 0.004 and 1.856 ± 0.002 mJy respectively). Therefore, assuming that the ratios remained constant, I decided to measure the Balmer decrement as two separated ratios, using the data that was acquired simultaneously. From January 2001 data I obtain Hα : Hβ = 3.4, while from August 2001 data I calculate Hβ : Hγ = 1.8. Combining both results I get Hα : Hβ : Hγ = 3.4 : 1.0 : 0.5. My values for the Balmer decrement differ noticeably from HH1990's. Part of the difference, especially for Hβ : Hγ, might be explained by better resolution in my spectra, but, after close inspection of HH1990's data (see Figure 1 in HH1990), their reported value for Hα : Hβ do not look realistic and the ratio seems to be closer to mine. Qualitatively, though, my conclusion is the same: the Balmer decrements suggest that the accretion disk is optically thin and cool by CV standards (see, for example, Williams & Shipman, 1988). This conclusion is strengthened by the detection of O I 7773 which, according to Friend et al. (1988) is a good indicator of the state of the disc, its emission indicating an optically thin accretion disc.

A second order polynomial was fitted to the continuum of each dataset and then the data were divided by these fits. The normalised continua were subtracted, and the datasets were binned in 20 phase bins before plotting Figures 4.5, 4.6, 4.7 and

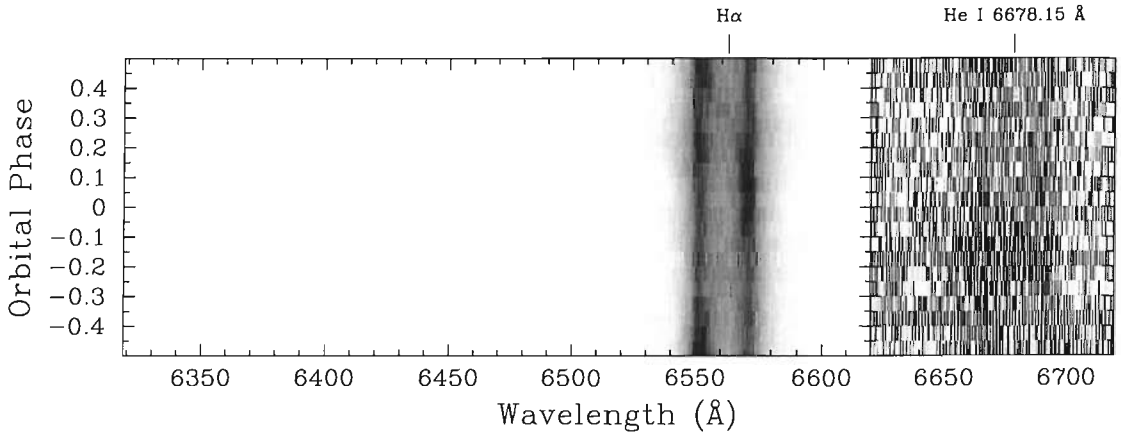

Figure 4.5: The data taken in January 2001 at the INT, binned into 20 bins of orbital phase. Per panel, from left to right, the maximum plotted levels are: 12.0 mJy (H α) and 0.3 mJy (He I 6678).

4.8. The features I detected show emission of very different strengths from one another, and thus it is not possible to find a suitable common scale to appreciate detail in all of them. Instead, when needed I divided the dataset producing one panel for each wavelength and then I normalised the colour scale from the continuum level to a maximum intensity in each panel. These trailed spectra display double peaked emission following a sinusoidal motion that varies with orbital phase. I interpret this as the rotating accretion disk, approximately tracking the emission of the white dwarf it surrounds. The other remarkable feature in these spectra is a higher-amplitude sinusoid also varying with orbital phase, but shifted with respect to the assumed zero phase. It can be seen very clearly, for instance, in O I 7773(Figure 4.8). This emission is produced in the stream/disc impact region, which is usually termed the bright spot.

4.2.2 The primary star

HH1990 measured a value of $17 \pm 4\,\mathrm{km\,s^{-1}}$ for K_1. I tried to check and refine this value by using Schneider & Young (1980)'s method. I convolve my data with a difference of gaussians equidistant from a candidate line centre, and say that the line centre is reached when the result of the convolution is zero. By increasing the separation of the gaussians I gather information from the wings of the profile, which is produced in regions of the disc closer to its centre (Horne & Marsh 1986). I assume

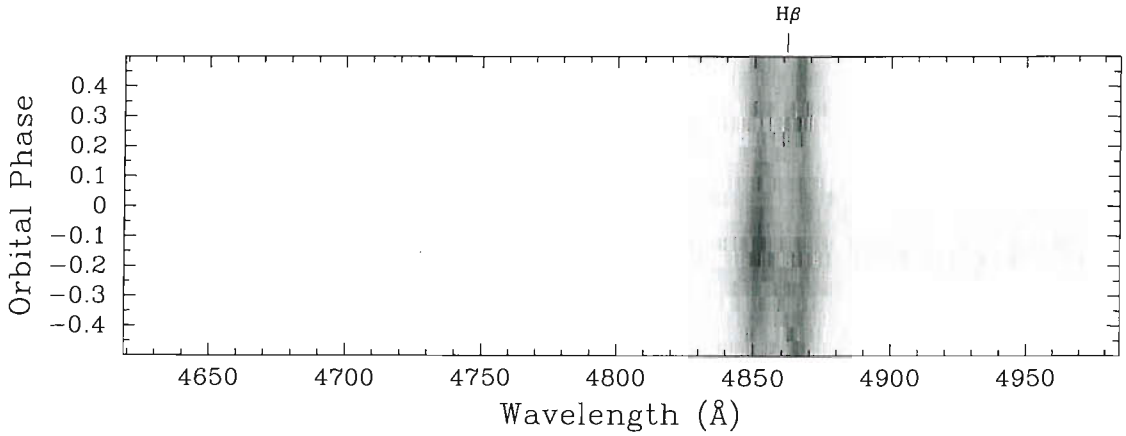

Figure 4.6: The data taken in January 2001 at the WHT, binned into 20 bins of orbital phase. The maximum plotted level is 6.0 mJy.

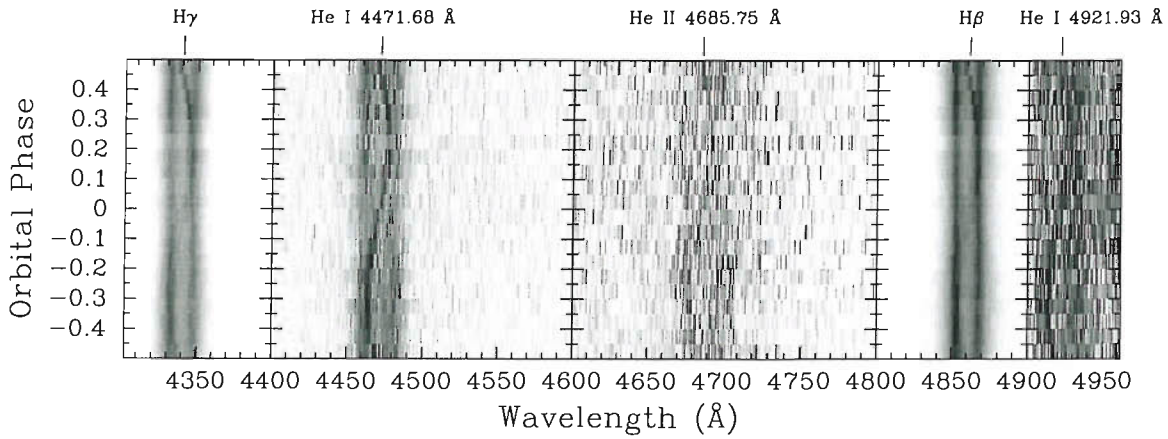

Figure 4.7: The blue data taken at the WHT in August 2001, binned into 20 bins of orbital phase. Per panel, and from left to right, the maximum plotted levels are: 4.0 mJy (H γ), 0.5 mJy (He I 4471), 0.2 mJy (He II), 6.0 mJy (H β) and 0.2 mJy (He I 4921).

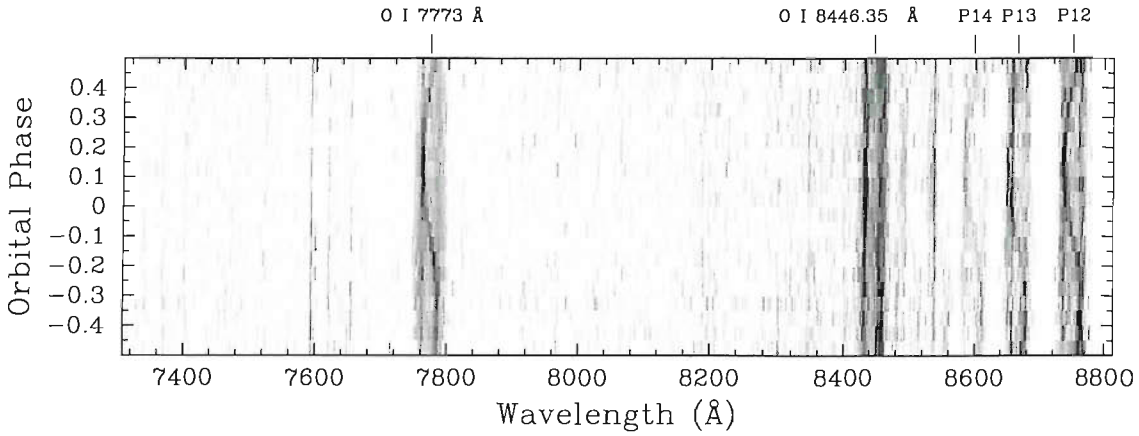

Figure 4.8: The red data taken at the WHT in August 2001, binned into 20 bins of orbital phase. The maximum plotted level is 0.5 mJy.

that the motion of these regions tracks the motion of the accreting object, so the further into the wings the measure is done, the better the estimate of the motion of the white dwarf. However, the process does not continue indefinitely because of the noise present at the continuum level.

The motion of each disc region is calculated by fitting the orbital solution:

$$V = \gamma - K \sin\left(\frac{2\pi(\phi - \phi_0)}{P}\right) \tag{4.1}$$

to the measurements. γ is the systemic velocity, K is the velocity of the source of the emission, ϕ_0 is the phase of conjunction, and P is the orbital period of the system. Further, I avail myself of a diagnostic diagram (Shafter, Szkody and Thorstensen 1986) to decide when the calculation is becoming dominated by noise as the separation of gaussians (a) increases. This should reveal itself as a sharp rising of the statistics σ_K/K. At the same time, I also expect to see convergence of the calculated parameters (K, γ) and a phasing appropriate to the white dwarf.

My diagnostic diagrams behave only partly as expected. I do not put a strong constraint on the phasing for reasons that I will explain later (see Section 4.2.3). On the other hand, the convergence of the parameters is not beyond question, although the diagnostic diagram for Hβ(Figure 4.10) looks qualitatively better than the one for Hα. For Hα, I could not make up my mind as to the value of a to choose as the last valid one. Convergence of K is not achieved, so any choice of a would seriously affect the conclusion about the value of K. For Hβ, K shows certain convergence on the same range where σ_K/K takes off, so the selection is not so critical. I decided

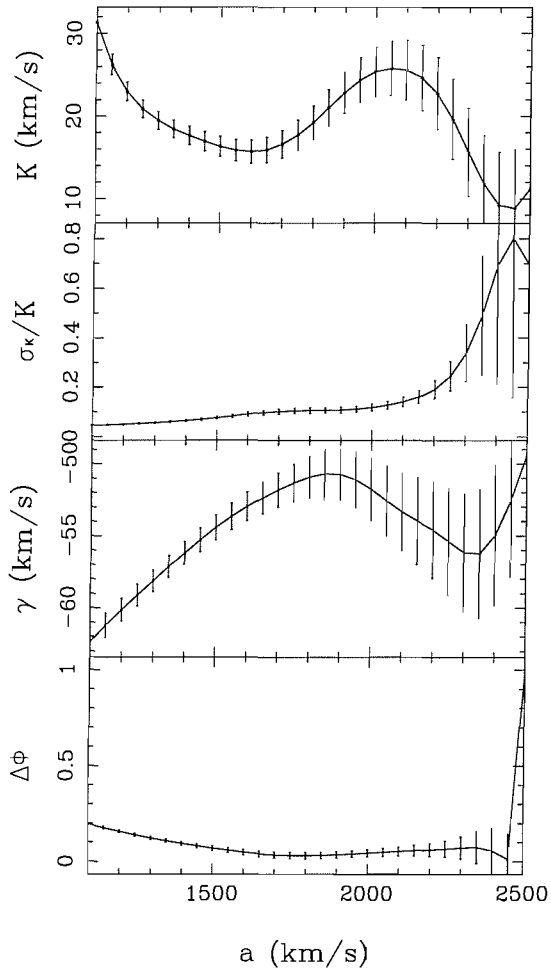

Figure 4.9: Diagnostic diagram for H α, using INT January 2001 data.

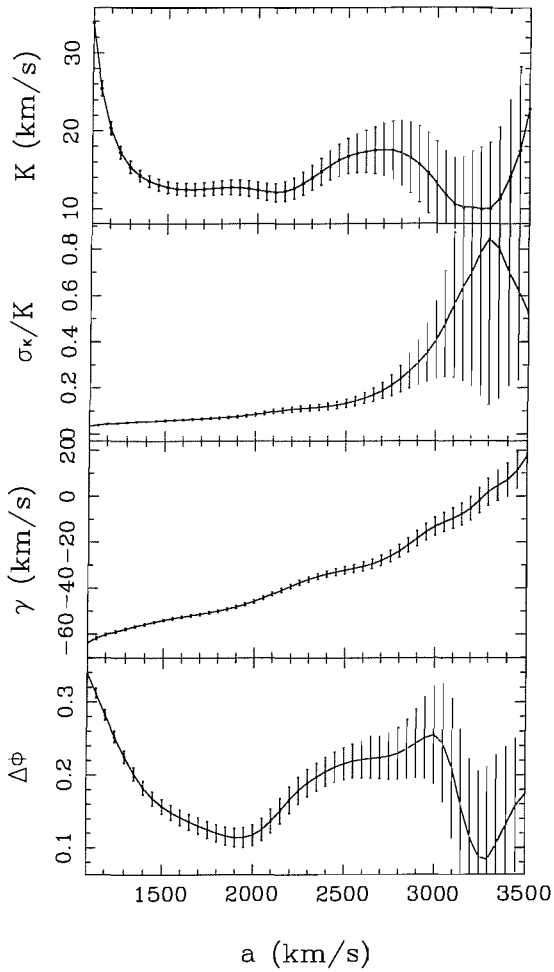

Figure 4.10: Diagnostic diagram for H β, using WHT August 2001 data.

that $a = 2600\,\mathrm{km\,s^{-1}}$ was a good choice. The value of K, which I take as K_1, the orbital velocity of the primary star, is then $17.4 \pm 2.7\,\mathrm{km\,s^{-1}}$, consistent with HH1990.

4.2.3 The secondary star

The presence of a secondary star (assumed to be an M dwarf since I am testing for the presence of a star of mass $0.15\,M_\odot$) is not obvious either in the average or in the trailed spectra. I attempted detection of it by means of a battery of techniques.

Firstly, I used the continuum-subtracted GD 552 data to produce Doppler maps

of the system by using Doppler tomography. This is a technique which allows us to combine all the information seen in trailed spectra, producing a 2-dimensional representation of the system in velocity coordinates. In a Doppler map, every point with coordinates (K_x, K_y) relates to a sinusoidal track in function of the orbital phase ϕ in the trailed spectra plots (see Equation 4.1). The velocity representation provided by the Doppler maps is not translated to position coordinates because the procedure to do this translation would be unreliable (several positions in the system could share the same velocity coordinates). Still, the velocity representation often is enough to separate the contributions from the main components of the system by using some simple assumptions. For details of the technique and its limitations see Marsh & Horne (1988). Figures 4.11, 4.12, 4.13 and 4.14 show the Doppler maps produced with my data. From top to bottom the rows show: 1) the Doppler tomograms, 2) the observed spectra from which the tomograms were computed, and 3) data computed from the tomograms. The ephemeris used for computing the tomograms is:

$$HJD = 2447365.5473(20) + 0.07134(11) \times E \tag{4.2}$$

taken from HH1990.

There are two obvious features present in all the maps: a ring structure, which I identify as the accretion disc, and a strong spot of emission. This spot marks the impact of the stream and disc. There is no sign of the mass donor which would be expected to be sited somewhat inside of the ring of emission from the disc.

The changes in position of the bright spot in my tomograms are due to the large uncertainty of the period used for setting the orbital phases. The period is only known to a precision of 1 part in $\sim$ 650, and thus the relative orientation after $\sim$ 650 orbital cycles apart ($\sim$ 46 d for GD 552) is arbitrary.

The second technique I used consisted in comparison of my GD 552 spectra with a set of M dwarf template spectra. These were provided by Kelle Cruz (personal communication) following the classification by Kirkpatrick, Henry & McCarthy (1991). The stars used are listed in Table 4.1.

The Na I doublet near 8200 Å is the fingerprint of a cool red star, as are broad molecular bands nearby. As I was not able to recognise any such features in the GD 552 data, I looked for a constraint upon its presence given that its features

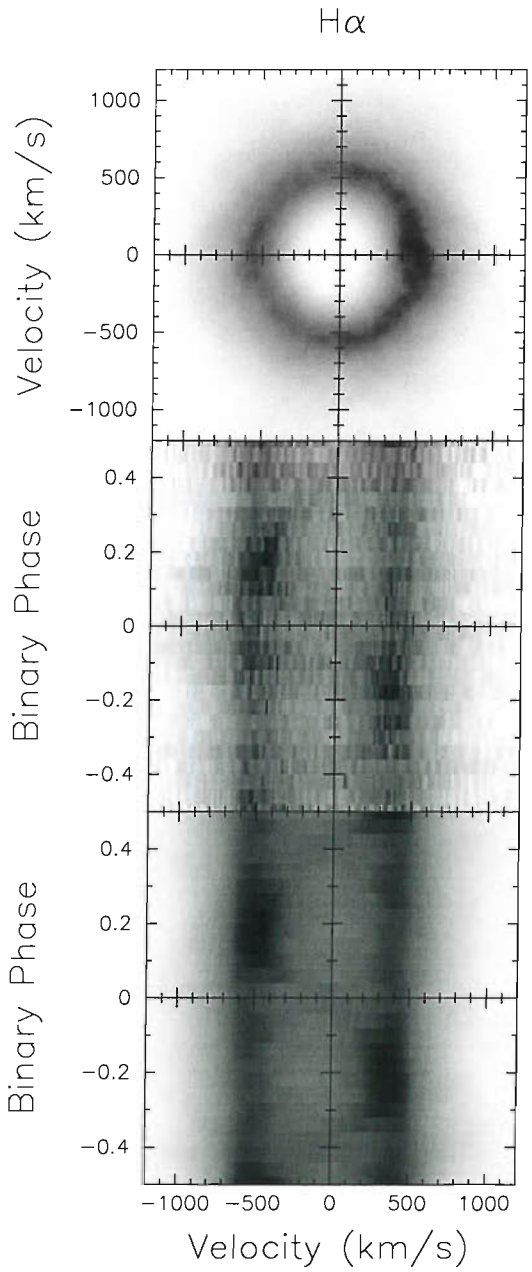

Figure 4.11: Doppler tomography for the INT January 2001 dataset.

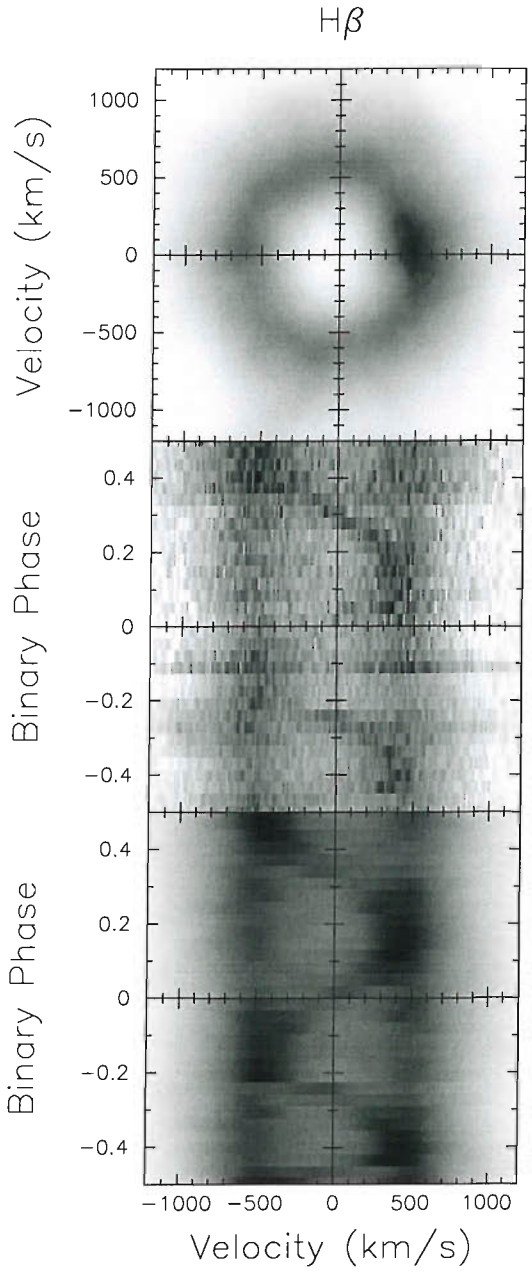

Figure 4.12: Doppler tomography for the WHT January 2001 dataset.

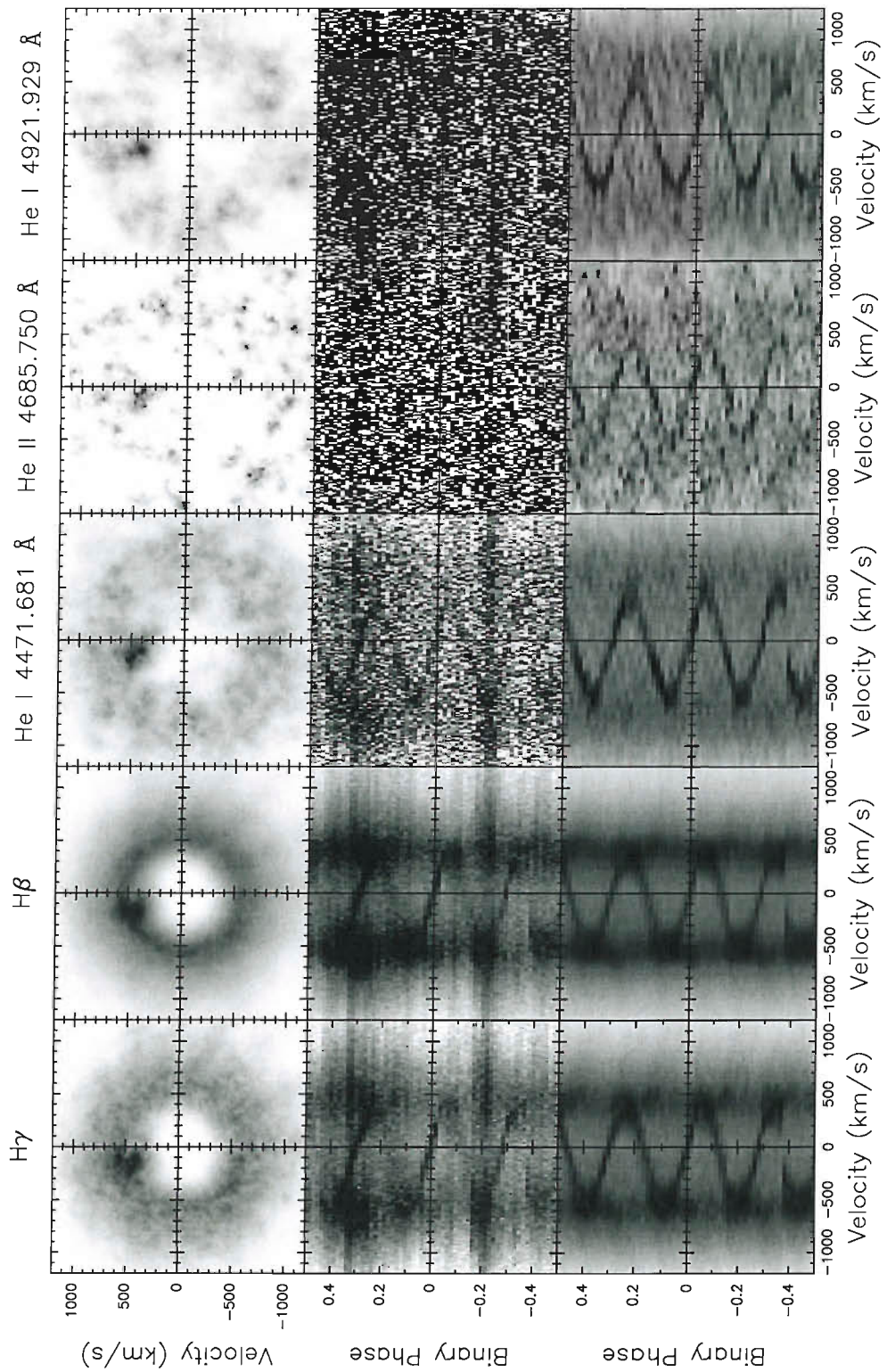

Figure 4.13: Doppler tomography for the WHT August 2001 dataset, blue arm.

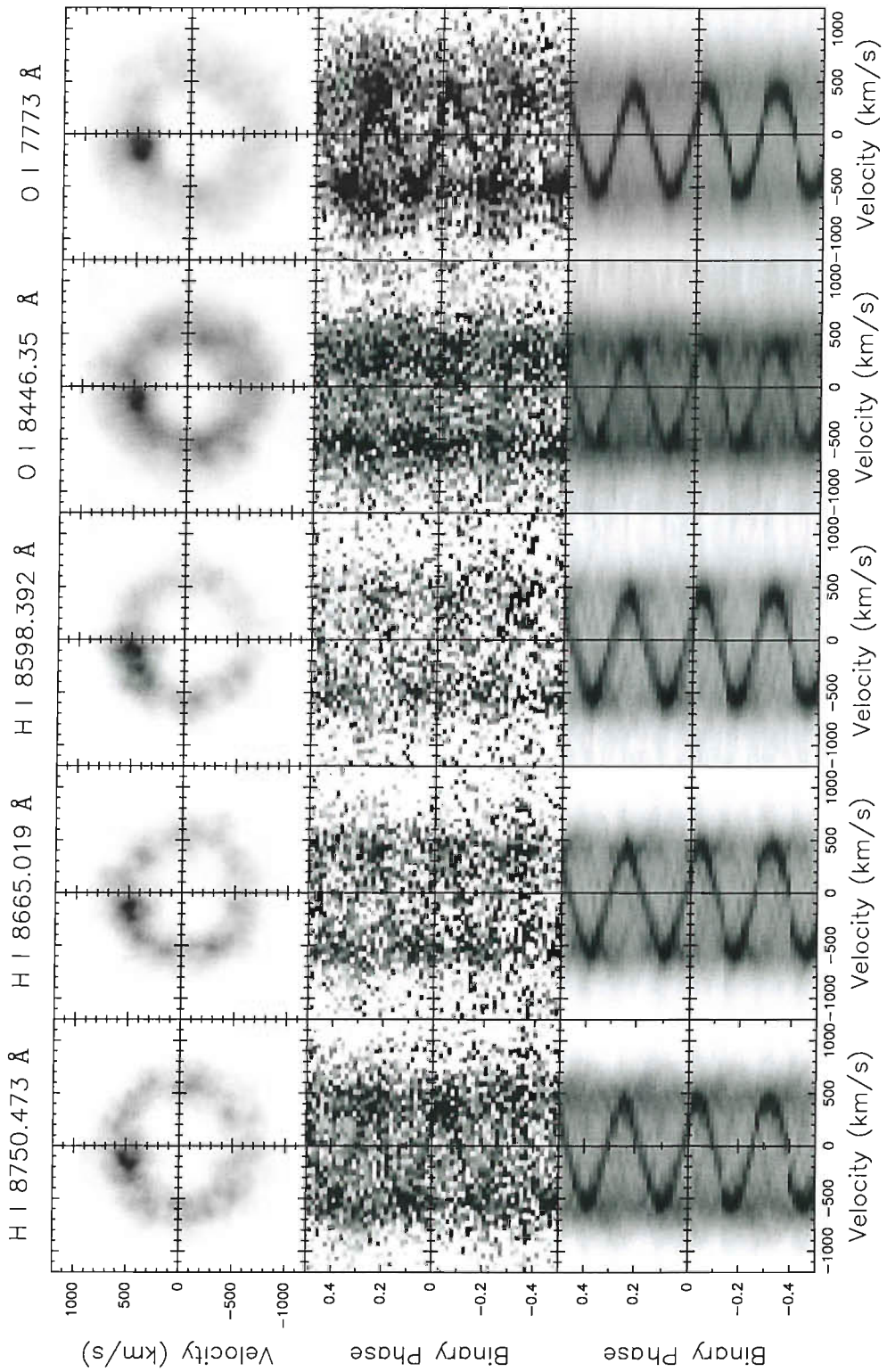

Figure 4.14: Doppler tomography for the WHT August 2001 dataset, red arm.

Table 4.1: List of M star templates used for estimating maximum contribution of an M star to the GD 552 profile.

Spectral Type	Star
M0.5	Gl 720A
M1	Gl 229
M1.5	Gl 205
M2.5	Gl 250B
M3	Gl 752A
M3.5	Gl 273
M4	Gl 213
M4.5	Gl 83.1
M5.5	Gl 65A
M6	Gl 406
M6.5	G 51-15
M7	VB 8
M8	VB 10
M9	LHS 2065

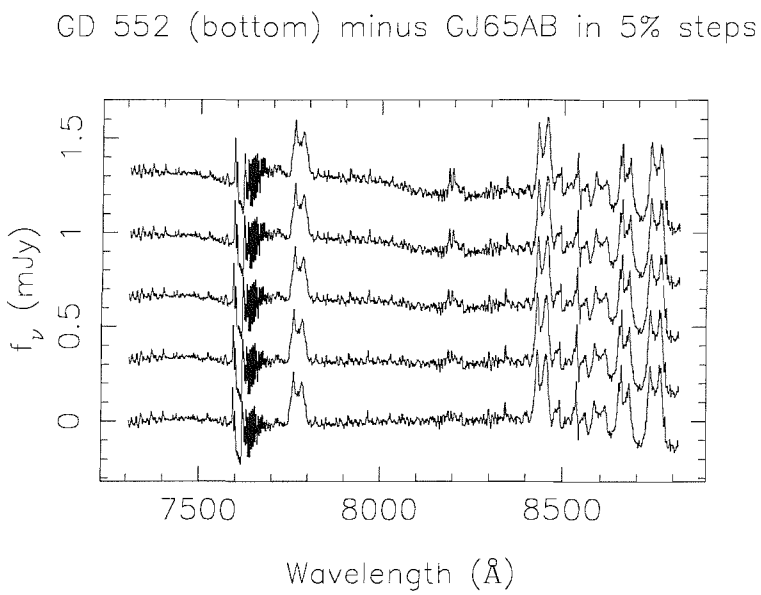

Figure 4.15: GD 552 data (bottom) minus a template star (Gl 65A) in 5% steps from bottom to top, starting from zero percent. When 10% Gl 65A is subtracted from GD 552 data, the presence of M star features is easily seen from the growing bump at 8200Å due to the NaI doublet.

are not detectable. First I normalised the spectra of GD 552 and of each template in Table 4.1. I did this dividing by a constant fit to the continuum in the range 8100-8400 Å, excluding the $\sim$ 8200 Å doublet. The I subtracted each normalised template from the GD 552 data in 5% steps. In Figure 4.15 I show an example of this procedure. GD 552 is at the bottom of the plot. Each profile above GD 552 increases the amount of template subtracted from the data by 5%. Consistently, I found that for all the templates the presence of M star features is obvious once we reach 10%.

A third, more sensitive, technique I employed for trying to detect the secondary star in my spectra star was skew mapping (e.g. Smith, Dhillon and Marsh 1998; Putte et al. 2003) with Gl 65A, an M5.5 star (Gliese & Jahreiss 1991). A skew map is produced by applying Doppler map techniques to the cross-correlation functions of the CV data with a suitable template. If there is a consistent cross-correlation between the template and a pattern following the orbital motion of the binary system, then the skew map will show a spot at the velocity coordinates of the source of the pattern.

For skew mapping I used the range 7850-8400 Å, which is devoid of emission lines.

First of all I fitted a constant to the continuum of both GD552 and Gl 65A data (for scaling). Then I fitted a 5-knot spline to both continua (the number of knots set due to the complex shape of Gl 65A's continuum). Dividing by these fits and subtracting unity, I obtained flattened continua. Then Gl 65A had to be prepared as a suitable template for an hypothetical secondary star present in the spectra of GD552, accounting for both instrumental and physical effects. First I smeared the average spectrum of Gl 65A to account for its orbital motion during the exposure. In:

$$V_{smear} = \frac{2\pi K T_{exp}}{P} \tag{4.3}$$

K is the velocity of the moving object ($200\,\mathrm{km\,s^{-1}}$ as a rough approximation, assuming HH1990's parameters for GD 552), T_{exp} is the exposure time (300 s in my case) and P is the period (0.07134 d for GD 552). From this I obtained $\sim 60\,\mathrm{km\,s^{-1}}$ for the smearing to be applied. Also, I rotationally broadened this spectrum by $75\,\mathrm{km\,s^{-1}}$, taking 75% of the typical value for an edge-on system ($100\,\mathrm{km\,s^{-1}}$). Finally, I shifted the Gl 65A spectrum by $29\,\mathrm{km\,s^{-1}}$ to account for its systemic radial velocity (Wilson 1953).

In Figure 4.16, the top left panel is the skew map produced by cross correlation of GD552 with the Gl 65A prepared as described above. There are no discernible peaks in this panel. I added percentages of Gl 65A to the original GD552 data, after applying a sinusoidal velocity factor to Gl 65A ($\gamma = -55\,\mathrm{km\,s^{-1}}$, $K_x = 0\,\mathrm{km\,s^{-1}}$, $K_y = 400\,\mathrm{km\,s^{-1}}$), using the orbital phases of the GD552 data. The top right panel of Figure 4.16 is the result of skew mapping the GD552 data + 10% Gl 65A; bottom-left panel with 20% Gl 65A and bottom-right panel with 30% Gl 65A.

I found that I could recover the position of the artificial secondary by adding 10% of Gl 65A to the GD552 data prior to cross-correlation and skew mapping. This is compatible with the conclusion reached by subtracting increasing amounts of Gl 65A to GD552 data until the features of the M star became distinguishable.

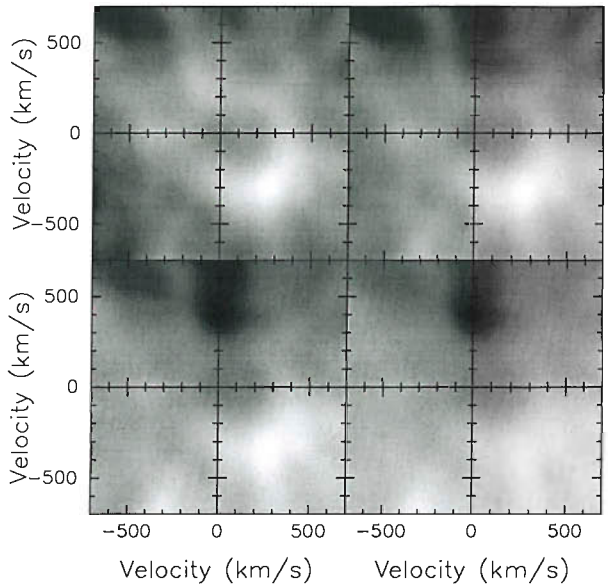

Figure 4.16: Skew mapping of GD 552 and a template M star. The top left panel uses only GD 552 data for cross correlation. The other panels use a mixture of GD 552 and increasing percentages of the template star. See text for details.

4.2.4 System parameters

In section 4.2.3 I placed an upper limit of 10% upon the contribution of an M star to the spectrum of GD 552 in the range 8100 to 8400Å. I now use this restriction to estimate the mass of this hypothetical star. This will allow us to compare directly to HH1990's M_2 value, and thus to test their model.

I first need to convert my constraint into one upon the I-band magnitude of the M star. I start from the relation between magnitudes and fluxes, including a colour correction to make my data match the profile of the I band:

$$m_{I,10\%MS} = m_{I,GD\ 552} - 2.5 \log \left(\frac{\int_{\lambda_i}^{\lambda_f} \epsilon_I(\lambda) f_{\lambda,10\%MS} d\lambda}{\int_{\lambda_i}^{\lambda_f} \epsilon_I(\lambda) f_{\lambda,GD\ 552} d\lambda} \right) \tag{4.4}$$

In this equation, $10\%MS$ stands for 10 percent of the template M star; ϵ_I is the transmission for the I Band; λ_i and λ_f are the limits of the observed range in wavelength. $f_{\lambda,10\%MS}$ is 10% the normalised flux density of the M star, obtained dividing by a constant fit to the 8100-8400 Å region (the Na I doublet at 8200 Å excluded) and multiplied by 0.10. Similarly, $f_{\lambda,GD\ 552}$ is the flux density of GD 552

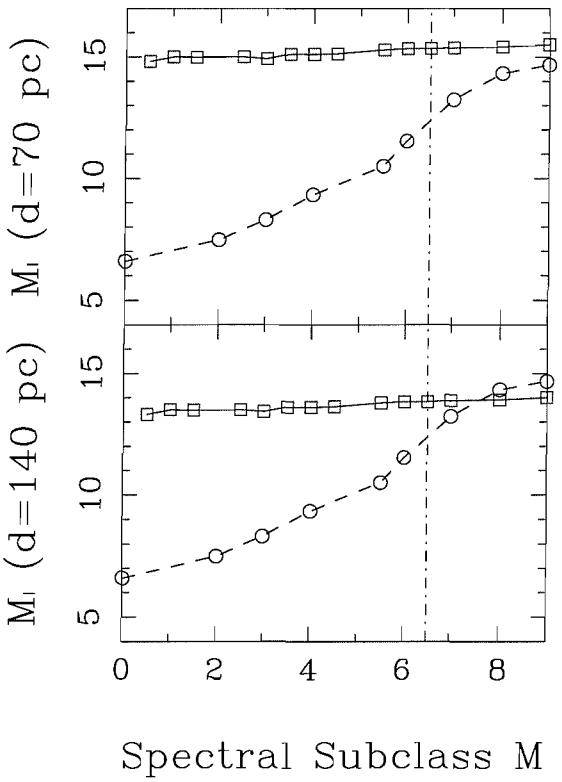

Figure 4.17: Comparison of computed M_I (solid line) for the mass donor in GD 552 versus tabulated M_I (dashed line, Leggett 1992) for the corresponding isolated star. The vertical line at M6.5 marks the limit set by Kirkpatrick & McCarthy (1994) for an hydrogen burning star. See text for details.

calculated dividing by a constant fit to its continuum. Assuming typical CV colours, I take $V - I = 0$ for GD 552, so $V = 16.5$ (Downes 1997). Then I use equation 4.4 with the M star templates listed in Table 4.1, obtaining $m_{I,10\%MS}$ for each case. (hereafter this will be referred to simply as m_I). The results are plotted in Figure 4.17. It must be noted that, while I am confident of the computed values, my data did not cover a small blueward tail of the I band, which affects the calculation according to Equation 4.4, although tests adding extrapolated points to estimate the difference with my result show the effect to be negligible.

In Figure 4.17 the dashed line marks the absolute M_I values published by Leggett (1992) as derived from a large sample of M dwarf stars. The vertical line, on the other hand, marks the spectral type for an hydrogen burning star with the lowest possible mass ($\sim 0.08\,M_\odot$, Kirkpatrick & McCarthy 1994). The difference between the top and bottom panels is the distance assumed in each case. In the top panel

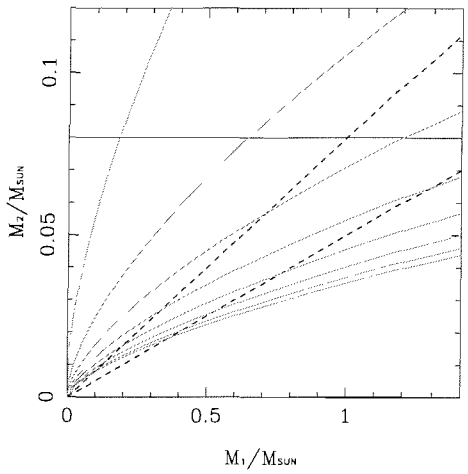

Figure 4.18: $M_1 - M_2$ plane, adopting $P_{orb} = 0.07134d$ and $K_1 = 17.4\,\mathrm{km\,s^{-1}}$. The horizontal solid line is the upper limit set upon M_2 in section 4.2.4. The dashed lines are the two extreme values for q, for an inviscid disc (above) and for a tidally limited one (below). The curved solid lines are lines of constant inclination angle. They start at 80° (bottom) increasing in steps of 10° towards the top, up to 10°.

I used the value $d \sim 70\,\mathrm{pc}$ from Greenstein & Giclas (1978); it is clear from it that the absolute magnitudes allowed by my data are inconsistent with the assumption that the mass donor in GD 552 is a main-sequence star. This implies that the mass of the companion star $M_2 < 0.08 M_\odot$, ruling out near main-sequence models such as that of HH1990. My conclusion remains unaltered even if GD 552 is twice as far as suggested by Greenstein & Giclas (1978), as shown in the bottom panel.

In Figure 4.18 I plot the constraint $M_2 < 0.08 M_\odot$ as a horizontal solid line. What other constraints can be reliably set upon the system parameters?

GD 552 is a non-eclipsing system. This implies that its inclination angle must be $< i_{max}$, with:

$$i_{max} = \cos^{-1}\left(\frac{R_{L,2}}{a}\right), \tag{4.5}$$

as approximated by Warner (1995). In this equation a is the binary separation, and $R_{L,2}$ is the volume radius of the Roche lobe of the secondary. $R_{L,2}/a$ is accurately approximated by Eggleton (1983)'s formula:

$$\frac{R_{L,2}}{a} = \frac{0.49 q^{2/3}}{0.6 q^{2/3} + \ln(1 + q^{1/3})} \tag{4.6}$$

where $q = M_2/M_1$. Thus, given a value for q, I can estimate i_{max}. q, on the other hand, can be reasonably constrained between two limits. One occurs for the case

when the disc is inviscid and so its outer radius, R_D, is given by:

$$\frac{R_D}{a} = 0.0859q^{-0.426}, \quad 0.05 \leq q \leq 1 \tag{4.7}$$

following the approximation by HH1990. The other limit occurs when the disc is tidally limited by gravitational action from the secondary star:

$$\frac{R_D}{a} = \frac{0.60}{1+q}, \quad 0.03 \leq q \leq 1 \tag{4.8}$$

(Warner 1995). I can combine Equation 4.7 or 4.8 with:

$$\frac{R_D}{a} = \frac{K_1^2}{v_D^2 \sin^2 i} \frac{1+q}{q^2} \tag{4.9}$$

to obtain q. In Equation 4.9 $v_D \sin i$ is the projected Keplerian velocity at R_D, which can be estimated from half the separation of the emission line double-peaks (Smak, 1981; Horne & Marsh, 1986). I made measurements of the separation of the peaks by fitting gaussians to them. The value changes appreciably depending on the line used for measurement. Eventually I decided to use the average of the results from Balmer lines in both January and August 2001. Half the separation of the peaks is then: $450 \pm 30\,\mathrm{km\,s^{-1}}$. Using this value in Equation 4.9 I can solve Equations 4.9 and 4.8 by iteration to obtain $q_{min} = 0.0523$. Analogously, I can solve Equations 4.9 and 4.7 to obtain $q_{max} = 0.0727$. These two restrictions are plotted with dashed lines in Figure 4.18. I expect the actual system parameters to lie between those two dashed lines.

Now, for both values of q I can calculate i_{max} by using Equations 4.6 and 4.5. I obtain 80.18° (tidally limited disk) and 79.15° (inviscid disk). In Figure 4.18 the curved solid lines are the loci of masses for a given inclination angle. They start (bottom) at 80° ($\sim i_{max}$) and decrease to 10° in steps of 10°.

These are all the constraints I can place upon the masses of the system without resourcing to speculative ideas. As an extra hint, I can consult the theoretical predictions by Howell, Nelson and Rappaport (2001). For the P_{orb} I have adopted, they predict that the mass of the secondary star is either $\sim 0.16 M_\odot$ (pre-bounce-period) or $\sim 0.04 M_\odot$ (post-bounce-period). I have already shown that the former is not realistic according to my observations. The latter, on the other hand, goes right through the middle of my constraints.

4.3 Summary of my findings

I have shown that the absence of any detectable contribution from the mass donor in the low-luminosity system GD 552 rules out the presence of a near-main-sequence dwarf in this system. This shows that HH1990's model for GD 552 is not correct. Instead I believe that GD 552 has a brown dwarf secondary star, suggesting that it is a post-period-minimum system. This explains the low orbital velocity of the white dwarf combined with the widely separated double-peaks of the emission lines from the disc, and also why this system shows several signs of very low luminosity. Evolutionary models suggest that the donor now has a mass of order $M_2 \sim 0.04\,M_\odot$, but otherwise the parameters of the system are ordinary, with $M_1 \sim 0.6\,M_\odot$ and an orbital inclination $i \sim 40°$. GD 552 appears to be a key system for understanding the late evolution of CVs.

Chapter 5

GY Cnc

5.1 Introduction

GY Cnc was discovered by Gänsicke et al. (2000) as part of a search for new CVs from a list of candidates published by Bade et al. (1998). This list was a subset of the Hamburg Schmidt objective prism survey (Hagen et al., 1995), selected on the basis of spectroscopic properties. Gänsicke et al. (2000) carried out primarily a photometric detection, their spectroscopy limited to just two identification spectra. They concluded that GY Cnc is an eclipsing dwarf nova, above the period gap ($P_{orb} = 4.2$ hours), varying between $V \approx 12.5$ during outburst and $V \approx 16$ during quiescence.

Thorstensen (2000) carried out a spectroscopic study of this system, calculating the parameters reported in Table 5.1. In this table I include a column with the same parameters for U Gem, to illustrate the striking similarities between both systems. This made GY Cnc a natural choice of system to compare some of the spectroscopic findings I have presented for U Gem. Furthermore, Thorstensen's data was low resolution so he could not be sure of detecting the spectral signature of some of the system's standard components. My higher resolution allows me to do so, but several thought-provoking surprises were to be found in this process.

Table 5.1: Comparison of parameters for U Gem and GY Cnc. Sources: [1] Friend et al. 1990, [2] Long & Gilliland 1999, [3] Thorstensen (2000), [4] Wade 1981, [5] this thesis.

Parameter	GY Cnc	U Gem
K_1 ($\mathrm{km\,s^{-1}}$)	115 ± 7 [3]	107.1 [2]
K_2 ($\mathrm{km\,s^{-1}}$)	297 ± 15 [3]	294.7 [1, 4]
i (°)	77.3 ± 0.9 [3]	72 [5]
P_{orb} (s)	15158 [3]	15285 [2]

5.2 Results

5.2.1 Average spectra

Figures 5.1 and 5.2 are average spectra for the blue and red datasets. Broad Balmer lines (Hα and Hβ), Fe II 4923.92 Å (hereafter Fe II), He I 6678.149 Å (hereafter He I) and He II 4685.750 Å (hereafter He II) are present in these profiles. The broadness of the profiles calls for attention when analysing pairs of lines close to one another (Hα and He I , Hβ and Fe II), because contamination can be present towards the wings.

The profiles show the common double-peaked structure, characteristic of emission by a rotating accretion disc surrounding the white dwarf in a CV. The double-peak in Hα, however, is less pronounced than the one in Hβ, for instance. Thorstensen (2000) suggested the presence of a rotating, sub-Keplerian disc wind, or of flares, to explain the seemingly poor rotational disturbance observed in Hα. In addition to that, I believe this partial filling of the double-peak valley to be related to the presence of weak emission at a low velocity amplitude (see Section 5.2.3).

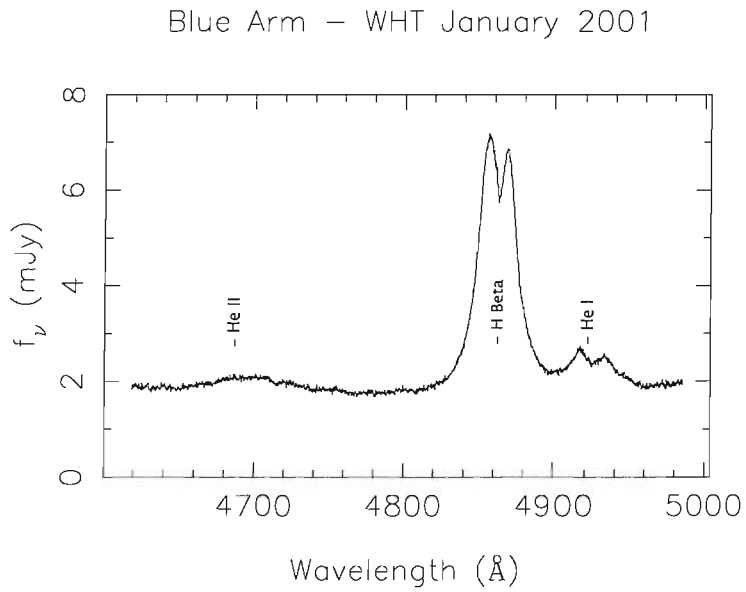

Figure 5.1: Average data.

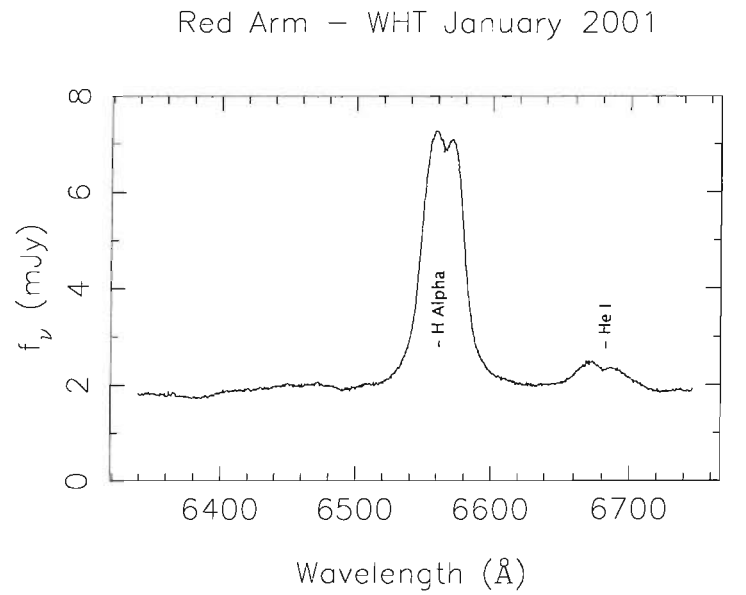

Figure 5.2: Average data.

5.2.2 Trailed spectra

Figures 5.3 and 5.4 show average trailed spectra corresponding to my datasets. I fitted a second order polynomial to the continuum of each dataset. I subtracted these fits from the datasets, later binning the spectra in 30 phase bins (blue arm) and 70 phase bins (red arm). There were some bins for which our data had no phase coverage. I set them to zero flux, which in Figures 5.3 and 5.4 appear as horizontal white bands. The observable features in the trailed spectra peak at very different flux levels, so, as with U Gem, I divided the dataset in panels. I produced one panel for each wavelength, highlighting the structure of the matching emission by normalising the colour scale from the flux level in the continuum to the flux level at some maximum intensity in the panel. A region of dead pixels in the detector is observed as a column centred on $\sim$ 6363Å. Another region of dead pixels was detectable right in the He I profile ($\sim$ 6670Å), but this time I applied a mask to it, so that the column was ignored during the analysis.

As in U Gem (see Section 3.2.3), emission lines of He II, Hβ and Fe II, Hα and He I are visible. The trailed spectra display double peaked emission, although it is less obvious in this case than in U Gem and GD 552. Still, it is obvious that the double peaks follow a low amplitude sinusoidal motion, perhaps more noticeable in the blue data, shifted according to orbital phase. I understand the double peaks as being produced by the rotating accretion disc, as explained in Section 1.4.1. The sinusoidal motion should be tracking the motion of the white dwarf.

No emission from the bright spot or from the mass donor is immediately discernible in the trailed spectra. Perhaps the only clear s-waves in the spectra are those peaking slightly above the continuum level (see left panel in Figure 5.4). I repeated the procedure described in Section 3.2.3.3. The skew-map (Smith, Dhillon & Marsh 1998) suggests that the emission comes from a region located at (0, 270) km s^{-1}. Considering that Thorstensen (2000) quotes (0, 297) km s^{-1} as the velocity centre of the secondary star, it seems fairly reasonable to assume that this emission is produced on the surface of the irradiated face of the mass donor, just as found in U Gem.

The eclipse is observable as a well defined region around phase 0, taking place first on the blueward side of the data (i.e. the preceding region of the accretion disc)

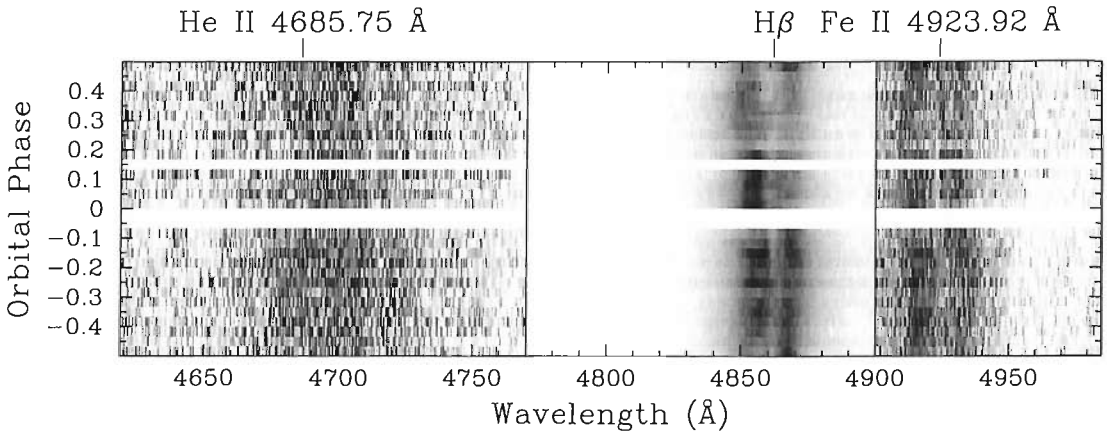

Figure 5.3: The blue data taken at the WHT in January 2001, binned into 20 bins of orbital phase. Per panel, and from left to right, the maximum plotted levels are: 0.5 mJy (He II), 7.0 mJy (H β) and 1.0 mJy (Fe II).

and then on the redward side (i.e. the receding region of the accretion disc) in good agreement with the theory. For setting the orbital phases I used the ephemeris as reported by Kato et al. (2002):

$$BJD = 2451586.21271(8) + 0.17544251(5) \times E \tag{5.1}$$

in which BJD stands for Barycentric Julian Date. Using tables provided by Taichi Kato (personal communication) I converted the eclipse data summarised in Kato et al. (2002) to HJD format. Then I refitted the ephemeris as:

$$HJD = 2451586.21265(5) + 0.17544573(5) \times E \tag{5.2}$$

which I used in the calculation of Doppler tomograms and trailed spectra. After some testing I decided not to include my own GY Cnc eclipse in this fitting because, being too poor time-resolution data, the determination of the middle point of the eclipse became strongly dependent on the method used and the points considered for the calculation. Kato's data, obtained in November 2001, provides a better constraint on the period anyway.

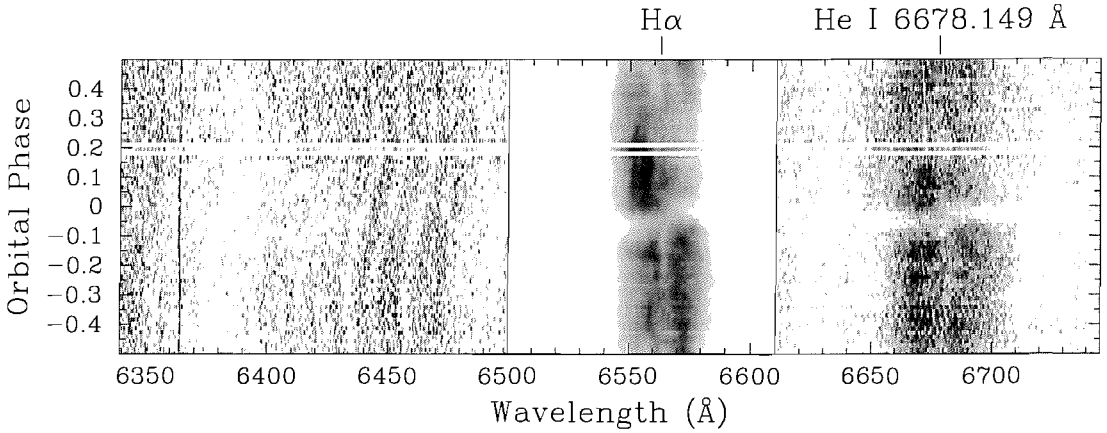

Figure 5.4: The red data taken at the WHT in January 2001, binned into 60 bins of orbital phase. Per panel, and from left to right, the maximum plotted levels are: 0.3 mJy (continuum), 8.0 mJy (H α), and 0.7 mJy (He I 6678).

5.2.3 Doppler tomography

Once again I used Doppler tomography (Marsh & Horne, 1988) to produce a picture of the system in velocity space, and in several different wavelengths. Figure 5.5 shows the result of this procedure. From top to bottom the rows show the Doppler tomograms, the observed spectra from which the tomograms were computed (actually, the phases not covered by my data were excluded), and data computed from the tomograms.

As usual, the velocity scales are relative to the line centres. The grey scales go from zero to 90% of the peak flux in the tomograms for the top row. The bottom row has a scale from 0 to 100% of the peak flux. The middle row uses a grey scale starting at zero but requiring different maximum levels in each panel to enhance visualization of details; from left to right, the scale is saturated at 30%, 90%, 70%, 90% and 70% of the peak flux.

Some features revealed by the tomograms are rather puzzling. The accretion disc is clearly seen in H α, H β and Fe II, and with less clarity in He I . The mass donor is reasonably well resolved in H α and H β, being also strongly hinted in He I , although at an unexpectedly high velocity. The bright spot, present in He II, Fe II and possibly He I , is surprisingly absent from H α and H β. As in U Gem but less strongly, some low velocity emission seems to be present in H α. Also in H α, but to

some degree visible in Hβ and He I , a sort of "comma" connects the low velocity material with the disc in the bottom right quadrant of the tomogram.

The secondary, as seen in Hα seems to be emitting from the whole Roche lobe, not just as result of irradiation from the white dwarf. The alternative, that its size is much larger than expected from Thorstensen's calculations, and thus what we see emitting is just a portion of the elongated face of the Roche lobe, does not seem realistic because K_1 and K_2 should then be off by much more than their current uncertainties (see Figure 5.6).

5.3 Discussion

These data give an exciting first view of a system for which much remains to be done. My spectroscopic analyses suggest that dedicated observing sessions spanning long intervals of time are needed, to check whether the uncommon features present in these data are permanent and, if so, to shed light on how they evolve.

Perhaps the most unusual feature is the absence of any bright spot signature in the Balmer lines. Due to the energy liberated by the stream/disc impact, this is not easily understood. Furthermore, if, as I think, the bright spot is detected in He II and Fe II, then we cannot argue that the system lacks the impact region. Instead, I think that this selectiveness can be understood in terms of the structure of the impact, which could render the mental picture of a blob of emitting matter as a rather naive image. I think the surroundings of the bright spot could become quite complex, producing an array of irradiated regions as well as zones with varying optical densities. It is possible, then, that a modified environment is installed around the bright spot, filtering out its emissions at some wavelengths. Detailed modelling of this idea would be required before proceeding further.

Although Doppler tomograms are a representation of CVs in velocity space, and thus the configuration of a system as seen in a tomogram cannot be taken as more than as a suggestion of what takes place in position space, it is tempting to imagine the "comma"-shaped structure (Section 5.2.3, see also Figure 5.6) as a connection between the secondary star and the accretion disc in position space. However, it is not clear how this configuration could take place. Preliminary simulations using

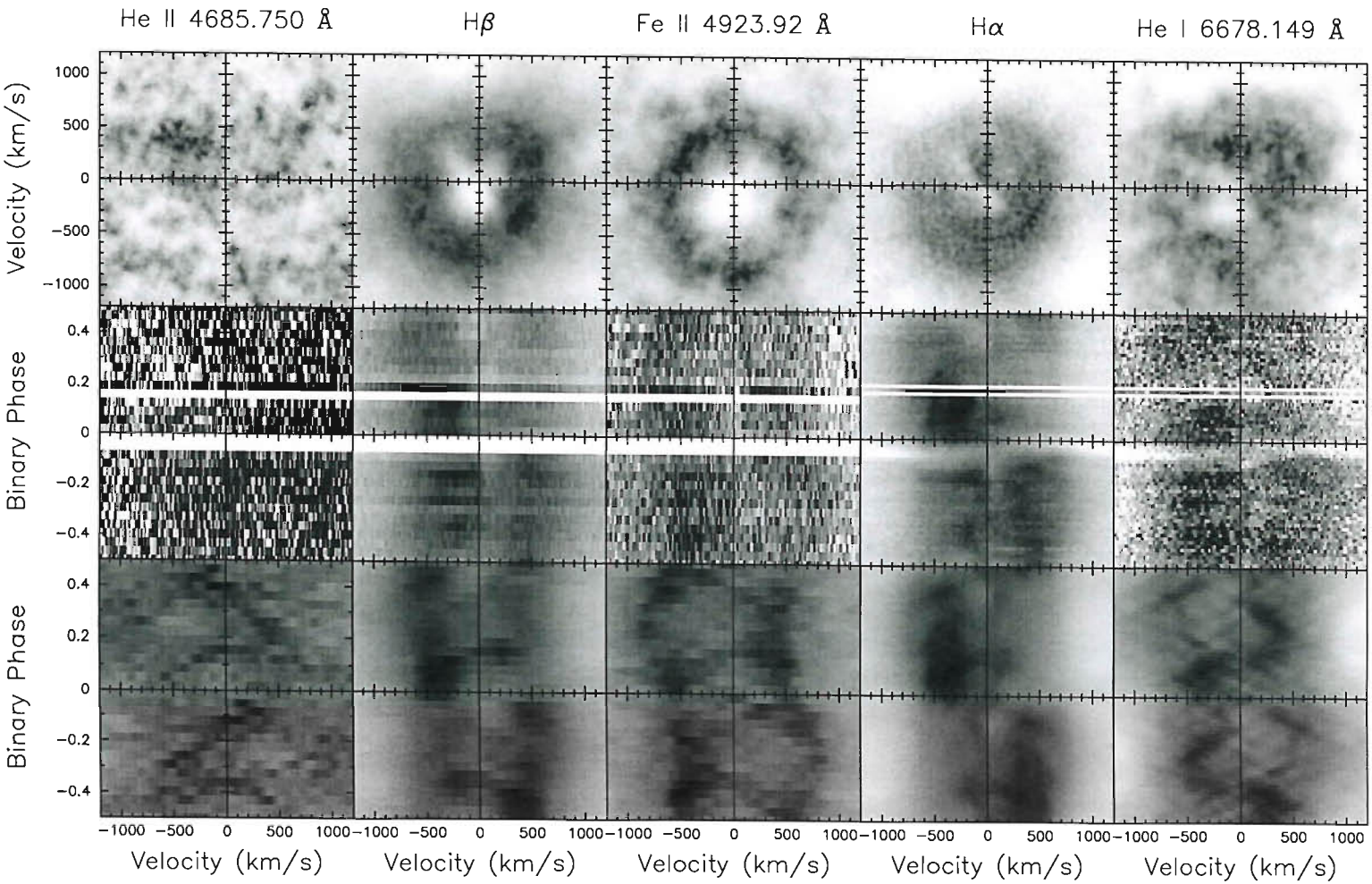

Figure 5.5: Doppler tomography for GY Cnc.

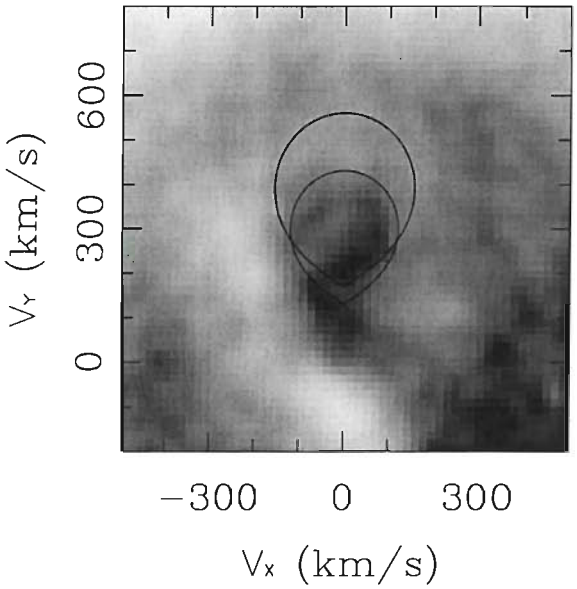

Figure 5.6: Hα emission with two superimposed Roche lobes. The smallest one was calculated using Thorstensen's values for K_1 and K_2. The largest one was computed by multiplying Thorstensen's values by 1.3.

Thorstensen's values for K_1 and K_2 suggest a stream trajectory that does not match the path suggested by this structure, neither for the disc's velocities nor for the ballistic stream's ones. One possibility, already discussed in Section 3.2.4.2 is that we are in the presence of a "slingshot prominence" (Steeghs et al., 1996). In this case, in addition to observe the structure irradiated by the white dwarf and the accretion disc, the "comma" might indicate that the prominence is large enough to touch the accretion disc and produce a region in which matter makes a transition from moving as a rigid body to acquire the velocities of the accretion disc, similar to what happens in the bright spot, as evidenced by my U Gem data (see Section 3.2.4.1, and see also Marsh et al. (1990)).

The detection of the secondary star in what seems to be emission from its whole surface (Hα) is intriguing in a system like this. There have been detections of warmer secondary stars in other systems (e.g. QZ Ser, Thorstensen et al, 2002), explained thanks to Helium enriched models, but in those cases the spectral type of the secondary star was identified as $\sim K$. In the case of GY Cnc, both Thorstensen (2000) and Gänsicke et al. (2000) identify the spectral type of the secondary star as $\sim M3$. One possibility is that the mass donor had its surface significantly spotted during the observing run, which could be related to the formation of the prominence

mentioned earlier. This would be a transient feature and thus I would not expect it to be detectable in a consistent fashion. This opens a chance for testing this idea in further observations.

Chapter 6

Conclusions and future work

6.1 U Gem

The radial velocity semi-amplitudes ("K-velocity") of the component stars in cataclysmic variable stars are fundamental to measuring their masses, and hence for studies of the evolution of these stars. A large number of measurements hinge on the assumption that the emission lines from the accreting matter in these systems, visible through optical line emission, tracks the accreting object, i.e. the white dwarf.

My analysis of U Gem data was aimed mainly at testing our ability to measure K_1 by indirect methods, using U Gem as a system in which the answer is known by direct measurement of the K-velocity of its white dwarf from *HST* spectra ($K_1 = 107 \pm 2\,\mathrm{km\,s^{-1}}$, Long et al. 1999). The latter is rarely achievable, mainly due to time allocation policies in space telescopes, so most of our knowledge on this aspect of CVs, which is statistical in nature, might be suffering from a bias produced by the ineffectiveness of current techniques to accurately recover this value. Sadly, though, my high-resolution datasets and the battery of techniques I applied failed to reproduce the value to better than $\sim$ 20%. In this, the weak spiral structure (Section 3.2.4.5) and emission from the bright spot, extending itself to high velocity regions in the CV, could be a main factor. The reason for the latter phenomena to take place is unclear and calls for improved modelling of the gas stream/disc impact

region.

Future models for the bright spot should also take into account the complex structure my observations have revealed, supporting the existence of a region in which the velocities appropriate for a ballistic stream adjust themselves to the velocities of the disc, producing an extended region of emission between both sets of velocities. This emission extends both to very high and very low velocities in the maps, for reasons that are unclear. Most surprising of all perhaps was the discovery of an exceedingly narrow component of the bright-spot, in the light of HeII 4686 which appears to be unresolved even at $R \approx 10{,}000$. The narrow spot appears to come from the disc rather than the stream, but seems to require a slightly larger value of radial velocity amplitude for the secondary star than has been measured to date.

I detected low velocity absorption and emission in my datasets, which might be explained by the presence of a prominence-like structure attached to the mass donor. Further observations of U Gem are required to decide if this suggestion is enough to account for the observed features, or if a new, more stable structure must be somehow included in the current model of CVs. If my idea of a temporary prominence is supported by observation (i.e. the features are not systematically detected in any future high-resolution observations), new data could provide a clue about how often do they appear in the system and what triggers their occurrence.

While I did find asymmetries at high-velocity, they do not appear to be evidence of stream overflow. The data should have been highly sensitive to any such phenomenon, but I could find no evidence of it. It seems that in U Gem the stream is completely stopped at the edge of the disc.

I found evidence for a weak spiral asymmetry in the disc, similar in nature to those seen in outburst. This might provide support for Ogilvie's and Smak's explanation for spiral structure based upon 3-body effects. The question arises then of whether spiral structure implies spiral "shocks". Spiral shocks are hydrodynamically predicted for low Mach numbers, like the ones that are achieved in systems with hot discs. Alternatively, they are expected in very large discs at reasonable temperatures. Most of the time a cataclysmic variable is characterized by a cool and small disc with a high Mach number (the exception being the state of outburst), therefore the phenomenon is hard to catch and consequently to study. Further observation of U Gem, perhaps in the form of a long term spectroscopic monitoring of

the system, could provide invaluable clues about the evolution of the phenomenon from quiescence to outburst, and help to settle the question posed above.

6.2 GD 552

My model of GD 552 is radically different from that of HH1990. Where they have a very high mass white dwarf in an almost face-on system, with an M dwarf donor of mass $\sim 0.15\,M_{\odot}$, my failure to detect the mass donor requires that it is a brown dwarf with $M_2 < 0.08\,M_{\odot}$. This makes GD 552 an excellent candidate for a post-period-bounce system. Evolutionary models suggest a mass of around $0.04\,M_{\odot}$ for the donor, and given the mass ratio constraints from above, I would expect the white dwarf's mass to lie in the range 0.55 to $0.75\,M_{\odot}$. My explanation of the low K_1 is therefore simply a case of extreme mass ratio, and I do not require a particularly low orbital inclination. There is a key point about my analysis that is worth emphasizing: I have managed to derive particularly strong constraints because of the GD 552's relatively long orbital period which maximises the difference between the pre- and post-period-bounce systems. In particular it means that the mass donor in the pre-bounce model is relatively easy to detect, so that failure to detect it is a clear indication of the post-bounce alternative.

Some aspects of my analysis can be improved. Most obviously, as a high proper motion system, a parallax for GD 552 would be of great interest. If GD 552 is truly of very low luminosity as I suspect, then I would expect its white dwarf to be amongst the coolest of any CV (Townsley & Bildsten 2003). Indeed its temperature now may reflect its age rather than accretion history. An interesting aspect of the optical spectra of GD 552 is the absence of any very obvious broad absorption lines from the white dwarf. If my model is right, I would expect the white dwarf to dominate. The two apparently contradictory facts may be compatible if the white dwarf is very cool because the Balmer lines from white dwarfs narrow considerably below 10,000 K, and could be lost under the broad lines from the disc. Further work to detect the white dwarf in the UV would be worthwhile.

6.3 GY Cnc

For GY Cnc I have presented the first available set of high-resolution spectroscopic data. My preliminary analysis is far from exhausting the many venues of research that can be exploited in this system. Some work is due in refining the system's orbital parameters, but more importantly so in constructing a reasonably simple and effective model to account for several of its spectroscopic features.

I have shown GY Cnc to be a CV which, while a kinematical twin of U Gem, differs considerably on the detectability of its components. The bright spot, which is consistently detected at every wavelength in U Gem, in GY Cnc is intriguingly absent from the Balmer lines and an inconspicuous feature in other lines. This calls for future work carrying out a careful modelling of the spatial and thermal structure of the bright spot.

The secondary star in GY Cnc shows a pattern of emission which makes me doubt that it is produced entirely by irradiation as was clearly the case in U Gem. I favour the idea of magnetic phenomena that transiently increase the mass donor's surface temperature, but this idea requires testing. A long term study of GY Cnc in Hα would be interesting to know whether this is, as I think, a feature observable by chance, or a constant feature of the mass donor. If not a permanent feature, such a study could reveal what triggers the enhanced emission.

Both U Gem and GY Cnc show evidence of the presence of prominences, whose physics in the context of CVs is yet largely unknown. It would be of much interest to study how long do these prominence-like structures last and how their appearance correlates with other phenomena.

Further comparative studies of both systems would be very valuable to increase our understanding of the thermal dynamics of CVs and their spatial makeup.

Appendix A

Ellipse fitting of Doppler map isophotes

In a Doppler tomogram it is normally possible to find at least two closed contours at a particular flux level. This happens because the tomogram is usually dominated by the disc continuum, in such a way that the flux increases from the centre of the map towards a ring of maximum intensity, the flux then decreasing from this ring outwards. This scenario makes the traditional methods to fit ellipses from the field of galactic surface photometry unstable (e.g. Kent 1983, Jedrzejewski 1987), because in them most levels occur only once. On the other hand, the techniques employed in computer vision, for the characterization of conics in an image, are very suitable for application here. I devised a new strategy by dividing the problem in two stages:

1. Selection of points pertaining to a closed contour, at a given level of flux.
2. Fitting of an ellipse to such points.

A.1 First stage

It must be noted that tracing the contours at a certain level and extracting the points pertaining to a single closed contour at the same level are two completely

different problems. The former is readily solved in a purely graphical manner (e.g. Burke 1987), while the latter (mine) is non-trivial and, as far as I know, not certainly solvable without human assistance. Consequently the first stage admits several approaches varying in efficiency, the following being just one possible implementation: After masking undesired regions (e.g. bright spot), a radius was measured from a centre defined by the user and then a number of angular directions were calculated according to the resolution of the image and the size of the radius. Zero or one pixel was then picked from each angular direction. The criteria used for the selection were the following:

1. No pixel was chosen in a masked region.
2. No pixel was chosen if it produced two contours crossing each other.
3. In the case of multiple instances of the level: the pixel closest to the centre and closest to the pixel selected in the previous angular direction was chosen. If no pixel had been selected in the previous angular direction, the pixel closest to the centre and to the original radius was chosen.

The procedure could be carried out almost on its own in the case of a smooth continuum, but it required close supervision when dealing with finely detailed (or noisy) structure. The main danger is for the algorithm not to close the contour or to take a wrong detour before coming back to the expected path.

A.2 Second stage

Once all the points for a particular level were chosen, I fitted them with ellipses according to an analytical ellipse-specific method proposed by Fitzgibbon, Pilu & Fischer (1999). The task is accomplished via a very efficient matrix procedure. In a non-matrix form I can explain the procedure as the fitting of a general conic of the form:

$$Ax^2 + Bxy + Cy^2 + Dx + Ey + F = 0 \tag{A.1}$$

but adding the constraint:

$$4AC - B^2 = 1 \tag{A.2}$$

so that the result will specifically be an ellipse. The constraint adds an arbitrary factor of scaling to the solution, but the algorithm provides for the removal of the effect at a later stage. The resulting general coefficients A,B,C,D,E,F were converted to the more meaningful values V_{xc},V_{yc} (coordinates of the centre of the ellipse), a, b (size of the two semiaxes), e (eccentricity) and θ (angle of rotation). Uncertainty bars were estimated by a bootstrap procedure over the points.

The solution given by the method of Fitzgibbon et al. (1999) has been proved to be unique, but it must be noted that it has a certain bias to low eccentricities, specially if only a few points are fed to the algorithm. This is fine for my purposes because I use many points for the fitting (basically limited by the resolution of the map) and also I do not want unrealistically high values for e (which for an accretion disc I expect to be close to 0 for most isophotes). If this was a problem, the bias could be removed by another bootstrap procedure at the cost of computing time (see, for instance, Cabrera & Meer 1996).

A.3 Application: Subtraction of elliptical continuum

By subtracting the disk continuum from the original Doppler map I can greatly improve the appearance of enhanced-emission features. Although I expect disc isophotes to have low values of e, this value will generally not be exactly 0. A subtraction based on assuming a perfect circular symmetry on the disc is therefore not recommended. I used the results from the ellipse-fitting process described above to subtract an interpolated elliptic continuum. To do this, I found for every point the two closest ellipses and then I linearly interpolated their fluxes according to the distance of the point to both ellipses. Special cases were: a point exactly in the path of an ellipse (its flux was used), and points beyond the region fitted (no flux was assigned).

In Figure (A.1) I show an example of the performance of the method by using a synthetic Doppler map.

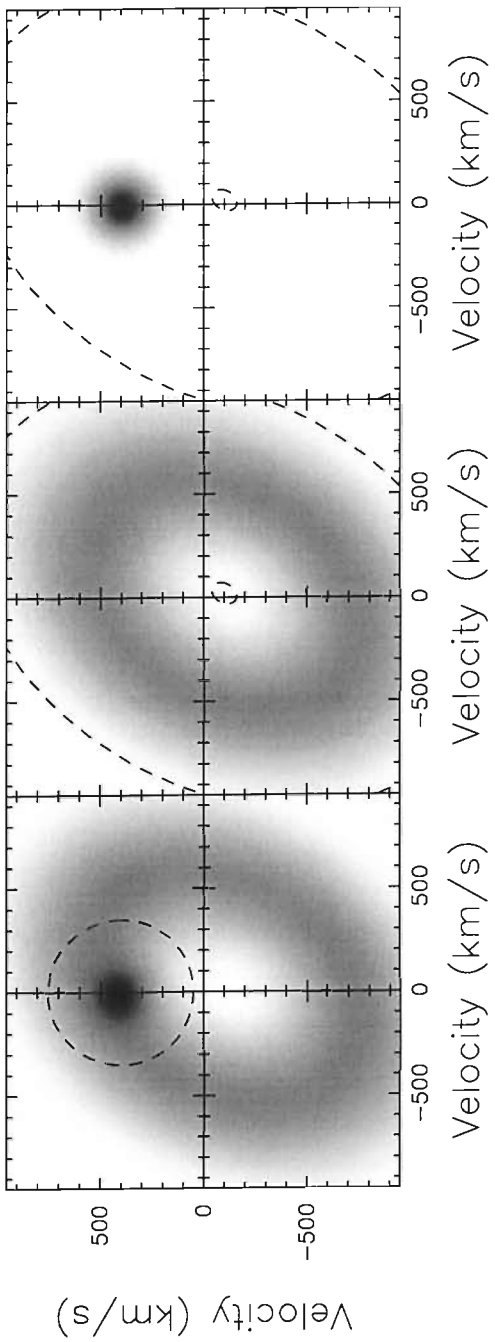

Figure A.1: Performance of the continuum subtraction. The left panel shows a synthetic tomogram with an elliptical continuum and a spot of enhanced emission. The region inside the dashed circle was masked during the fitting of ellipses. The middle panel shows the continuum interpolated from the fitted ellipses. In both the middle and right panel the dashed ellipses are the innermost and outermost fitted ones. The right panel shows the result of subtracting the middle panel from the left one. The (correct) 2-dimensional gaussian nature of the synthetic spot is made more evident in the right panel than it was in the original figure, in which it seemed to be elongated along the curvature of the disc.

Appendix B

Calculation of i using a spherical approximation

For this calculation I am using the following assumptions:

1. Tidal distortions affecting the shape of the mass donor are ignored, so the mass donor is treated as a sphere.
2. The disc follows a Keplerian regime.

I use an inertial coordinate system so that the plane xy is where the accretion disc lies, and the x axis points from the centre of the white dwarf to the centre of the mass donor when the mass donor is closest to the Earth. As seen from the Earth, the mass donor will eclipse an elliptical region over the disc, and the edge of the eclipsed region can be written as:

$$\frac{(x-\cos\alpha)^2}{A}+\frac{(y-\sin\alpha)^2}{B}=1 \tag{B.1}$$

where:

$$A=\left(\frac{R_2}{\cos i}\right)^2 \tag{B.2}$$

$$B=R_2^2 \tag{B.3}$$

α is the angle tended by the centre of the mass donor, measured anti-clockwise from the positive x-axis; and R_2 is the radius of the mass donor in units of a as

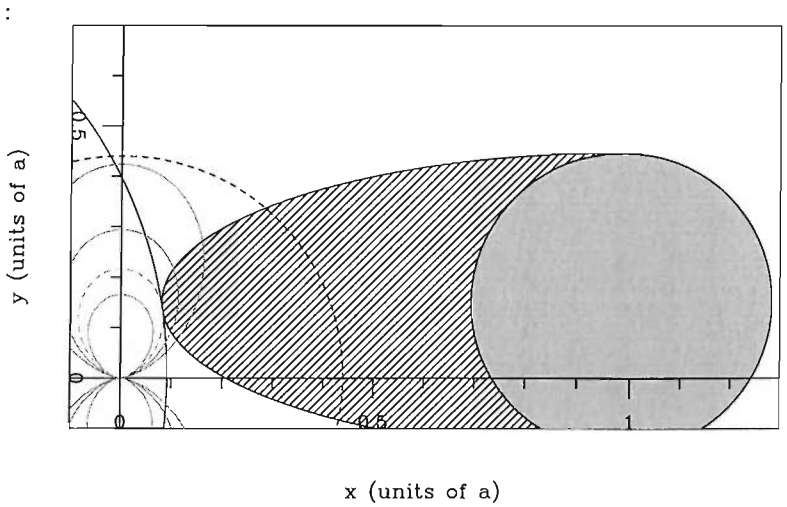

Figure B.1: The scenario for U Gem when $i = 71°$ (value obtained using this approximate method). The continuous grey curves close to the origin are Keplerian isovelocities. The dashed curve in this set is the isovelocity tangent to the threshold-point (see text) at 700 km s^{-1}. The remaining isovelocities are at 500, 600, 700 and 800 km s^{-1}. The solid black line crossing the abscisa at $x \sim 0.15$ is the envelope of the mass donor "shadow". The mass donor is plotted as a circle of radius R_2 eclipsing the semi-elliptical hatched area over the disc. The radius of a tidally limited accretion disc is plotted as a dashed circumference crossing the abscisa at $x \sim 0.42$.

predicted by Eggleton (1983). As I am interested in angles, which are invariant to changes of scale, the separation of the two stars originally appearing in my equations has been set to 1. Using (B.1) I can calculate the envelope of the sequence of "shadows" casted by the mass donor on the disc during its orbit around the white dwarf. This is done in a parametrical way, so the solution, once the inclination angle i is known, is in terms of α alone (see Figure B.1):

$$x = \cos\alpha - \frac{A\cos\alpha}{\sqrt{A\cos^2\alpha + B\sin^2\alpha}} \tag{B.4}$$

$$y = \sin\alpha - \frac{B\sin\alpha}{\sqrt{A\cos^2\alpha + B\sin^2\alpha}} \tag{B.5}$$

On the other hand, from the third assumption above, I can write the Keplerian velocities on the disc surface as:

$$V_D = \frac{Cy}{(x^2+y^2)^{\frac{3}{4}}} \tag{B.6}$$

with:

$$C = \sqrt{K_2(K_1+K_2)} \tag{B.7}$$

K_1 and K_2 are the projected orbital velocities of the white dwarf and the mass donor respectively. If I subtract the motion of the white dwarf from my data and then analyse lightcurves of the spectral profile from different bins of velocity, ideally I will find that at certain critical value of velocity, V_C, the eclipse will no longer be detectable. Spatially it happens that the envelope given by (B.4) and (B.5) is tangent to the curve of isovelocity on the disc given by setting (B.6) equal to the constant V_C. The spatial point where this happens will be called in what follows the *threshold-point*. One expects that V_C will be symmetrical for positive and negative velocities, so the remaining calculations are carried out only for the positive case.

In order to calculate i from the information above, I need to arrange it as a solvable system of equations. We know that the threshold-point is reached when the right member of (B.6) is made equal to V_C, at the same time that the derivative of this isovelocity with respect to x is made equal to the derivative of the envelope (B.4) and (B.5) with respect to x. Eventually the following non-linear system of equations is obtained:

$$f(i,\alpha) = V_{D,Exp} - \frac{Cy}{(x^2+y^2)^{\frac{3}{4}}} = 0 \tag{B.8}$$

$$g(i,\alpha) = \frac{3xy}{2x^2-y^2} + \frac{\cos\alpha}{\sin\alpha} = 0 \tag{B.9}$$

In the threshold-point it is possible to extend (B.4) and (B.5) to the equations (B.8) and (B.9), so the two only remaining unknowns are i and α, which can be calculated from the set of two equations (B.8) and (B.9) within the ranges $0° < i < 90°$. This system of equations is solved by using numerical techniques. For U Gem this gives $i = 71°$.

For U Gem, Figure B.3 is a sketch of the system on the plane $y = 0$ (x pointing from the centre of the white dwarf to the centre of the mass donor, and y pointing in the direction of the mass donor's velocity). In grey I display the mass donor as spherically approximated by Eggleton (1983). Outlined I display the Roche lobe of the mass donor. In $z = 0$ I plot the extension of a tidally-limited accretion disc, while the disc shielding is represented geometrically by a wall at the disc's rim (see Section 3.2.4.6). The small cross marks the centre of the mass donor. The dotted and the continuous line converging in the same point of the accretion disc are the lines of sight, tangent to the approximated and real mass donor respectively. To

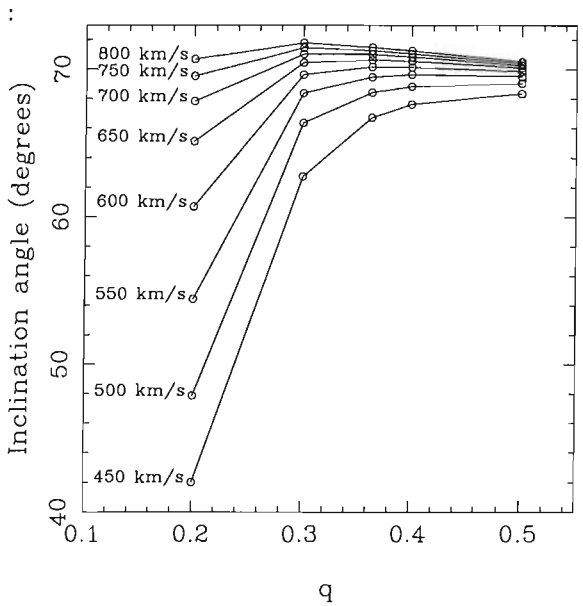

Figure B.2: These are the angles predicted by my method for a range of critical velocities and mass-ratios. The third column of points was calculated for the currently accepted mass-ratio 0.3634 in the case of U Gem.

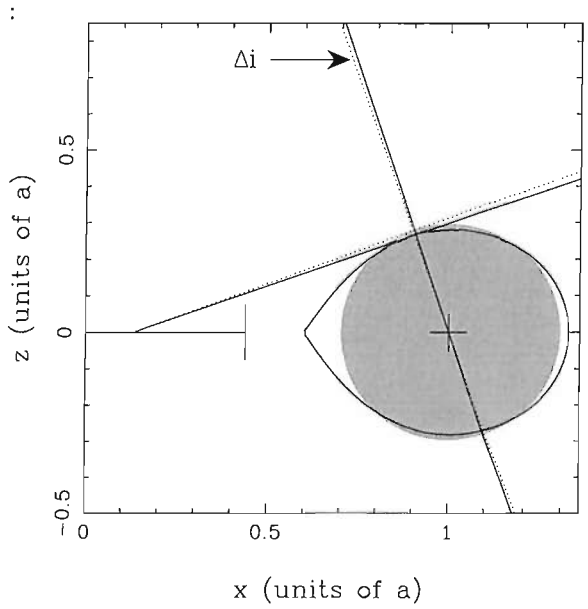

Figure B.3: Sketch of U Gem in the plane $y = 0$. See text for details.

these lines of sight correspond different i, which are signalled by the lines going through the centre of the mass donor, perpendicular to the lines of sight on each case (dotted line relates to dotted line, continuous line to continuous line).

My procedure uses the correlation by Eggleton (1983) to approximate the mass donor by a sphere, so I plotted both this approximation and the Roche lobe of the mass donor set by K_1 and K_2. I found that at these inclinations Eggleton will overestimate the radius of the mass donor. In velocity coordinates, the extension of the eclipse is related to a point on the disc's surface with the maximum eclipsed velocity (threshold velocity). This velocity is measured from the trailed spectra, so the use of Eggleton's approximation has no effect on its value. On the other hand, for the same threshold velocity (i.e. for the same point on the disc) a larger estimation of the radius of the mass donor implies a smaller estimation of the value of i.

Appendix C

A modified method to calculate K_1

The current standard procedure to estimate K_1 consists of two stages. The first one is to measure the radial velocities from the accretion disc. This is done by measuring the Doppler shifts of the line centres using a method by Schneider & Young(1980) (from now on SY1980) and then fitting an orbital solution to the results. This method assumes that the disc motion matches the white dwarf motion by being centred on the star. As the information about central areas of the disc is contained in the wings of the spectral profile, and as any perturbation to the disc symmetry is supposed to be confined to its outer regions, the further in the wings the analysis is done the better the approximation should be. Alas, the noise increases in the wings, so the second stage of the procedure is to use a diagnostic diagram (Shafter, Szkody & Thorstensen 1986) to decide how far in the wings the analysis can be done before noise overwhelms the signal (hoping for convergence towards K_1 before noise takes over).

A problem with this approach is that there are several cases in which Doppler tomography reveals a departure from symmetry even when working well into the profile wings, so no clear convergence is achieved in the diagnostic diagram. Also, SY1980 finds a line centre by filtering the profile with a difference of gaussians and then finding a balance of positive and negative filtered flux. Consequently, another problem is that any disc assymetry that is visible only at certain orbital phases will shift the calculation away from the actual centre, affecting later the fitting of parameters. This should not necessarily be the case if the second stage were not

blind to the first one. A further problem is posed by the common scenario of having a set of spectra in which the velocity of a single spectrum is difficult to measure, but the trend of the centres is still recognisable when looking at the whole set.

I modified the above procedure by combining the two stages into one multidimensional minimization. In what follows I assume that the data is prepared in this way: there are N spectral profiles of P pixels each. The profiles are denoted by the subscript j, and the pixels in each profile by the subscript i. The orbital phase corresponding to each profile, ϕ_j, is known. The abscissas of each pixel are all in velocity units, measured as the Doppler shift with respect to the central line of the profile at rest. For the profile j each pixel consists of v_{ji} (velocity abscissa), f_{ji} (flux) and σ_{ji} (uncertainty in flux). As in SY1980, I use a pair of gaussians to filter the flux; the centre of the gaussians are separated by a_G and their standard deviations are equal to each other with value σ_G. If I define the variable:

$$\mathcal{V}_{ji} = v_{ji} - U_j, \tag{C.1}$$

the merit function to minimize is then:

$$\chi^2(\mathcal{V}_{ji}) = \sum_{j=1}^{N} w_j(\mathcal{V}_{ji}) \left[\sum_{j=1}^{P} f_{ji} g_{ji}(\mathcal{V}_{ji}) \right]^2 \tag{C.2}$$

where:

$$w_j(\mathcal{V}_{ji}) = \frac{1}{\sum_{j=1}^{P} \sigma_{ji}^2 g_{ji}^2(\mathcal{V}_{ji})} \tag{C.3}$$

$$g_{ji}(\mathcal{V}_{ji}) = \exp\left(-\frac{\left(\mathcal{V}_{ji} - \frac{1}{2}a_G\right)^2}{2\sigma_G^2} \right) - \exp\left(-\frac{\left(\mathcal{V}_{ji} + \frac{1}{2}a_G\right)^2}{2\sigma_G^2} \right) \tag{C.4}$$

$$U_j = \gamma - K_x \cos(2\pi\phi_j) + K_y \sin(2\pi\phi_j) \tag{C.5}$$

The procedure actually works from bottom to top. For the dataset I expect to fit an orbital solution with parameters γ, K_x and K_y, so a vector with start values is used. For each profile a candidate centre, U_j, is then calculated. The remaining operations are all centred on the U_j for the particular profile, hence the $(\mathcal{V}_{ji})$ functionality. $g_{ji}(\mathcal{V}_{ji})$ is the filter applied to the data. Note that by incorporating U_j the filter takes into account the proposed orbital solution. $w_j(\mathcal{V}_{ji})$ is a weight given to a profile according to the quality of its data (smaller σ_{ji} produce a larger weight). $\chi^2(\mathcal{V}_{ji})$ is a sum over the whole dataset, incorporating the weigth for each profile and the flux filtered by $g_{ji}(\mathcal{V}_{ji})$. I must remark that, though similar, $\chi^2(\mathcal{V}_{ji})$ does not strictly have the usual statistical meaning of χ^2.

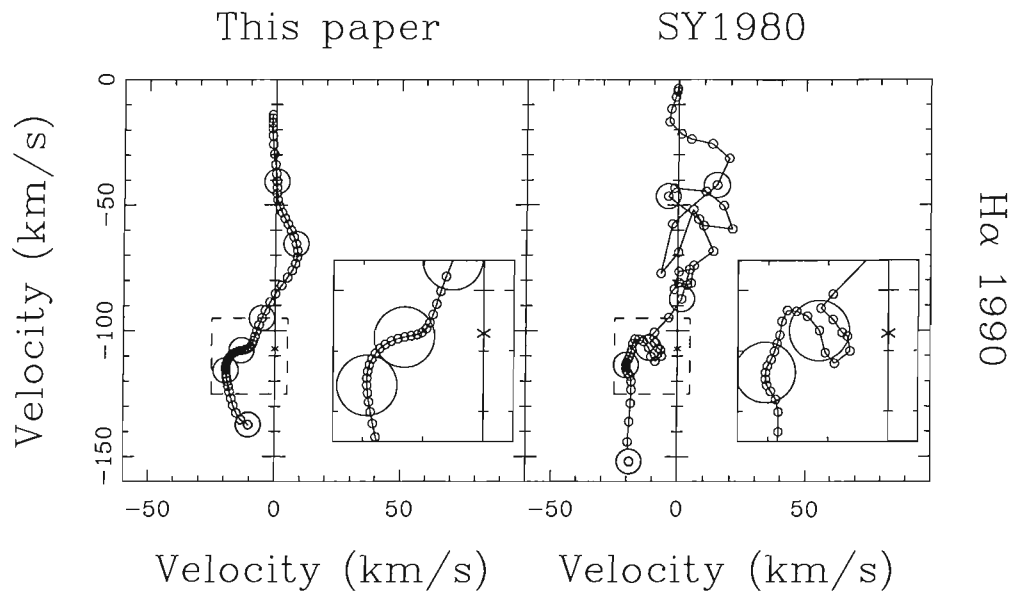

Figure C.1: My low-resolution 1990 dataset is used for this test. The small points are plotted at intervals of 50 km s^{-1}, from 1200 to 4150 km s^{-1}. The big circles are centred in points separated 500 km s^{-1}, the grey circle being centred around 1200 km s^{-1}. Uncertainty bars are omitted for the sake of clarity. The inset in the left panel reveals that my method is capable of extracting a good trend between ~1900 and 2400 km s^{-1}. SY1980 shows only an erratic path, not suggesting at any moment the correct trend.

$\chi^2(\mathcal{V}_{ji})$ cannot be minimised analytically, so resource to a numerical method is required. I found that the algorithm best suited to solve this problem was the BFGS variable metric method (e.g. see Shanno & Phua 1980). Uncertainty bars were estimated by a boostrap procedure (Diaconis & Efron 1983), with 1000 bootstrap samples being chosen from the original set of spectra.

This procedure is suitable for one value of a_G and σ_G. There is no clear prescription for choosing the value of σ_G, so some experimentation is required. A small value allows a finer sampling of the disc regions, but too small a value will be highly affected by noise. Once a σ_G is chosen, the calculation should be repeated for many values of a_G, pushing the separation of gaussians as much as possible (the rationale being the same as for SY1980). K_x, K_y are then plotted in a light-centre diagram (Marsh 1988), in the hope that the trend of K_x, K_y will point to the location of K_1 before the noise dominates. Figure (C.1) is an example of the application of this method, performing better than SY1980. However, I remark that this is a method to overcome noise, being as affected by systematic trends as any other.

Bibliography

Cox, A. (ed.), 2000, Allen's Astrophysical Quantities. AIP Press, USA.

Armitage, P., Livio, M., 1998, ApJ, 493, 898

Bade, N. et al., 1998, A&AS 127, 145

Bessell, M., 1999, PASP, 111, 1426

Boffin, H., Steeghs, D., Cuypers, J. (eds.), 2001, Astrotomography, Indirect Imaging Methods in Observational Astronomy. Lecture Notes in Physics, v. 573, Springer.

Burke, P., 1987, Byte Magazine (July)

Cabrera, J., Meer, P., 1996, IEEE Trans. PAMI, 18, 752

Collier Cameron, A. et al., 1999, MNRAS, 308, 493

Collier Cameron, A. et al., 1989, MNRAS, 238, 657

Diaconis, P., Efron, B., 1983, Sci. Am., v. 248, n. 5, 96

Downes, R., Webbink, R., Shara, M., 1997, PASP, 109, 345

Eggleton, P., 1983, ApJ, 268, 368

Fitzgibbon, A., Pilu, M., Fischer, R., 1999, IEEE Trans. PAMI, 21, 476

Friend, M., Martin, J., Smith, R., Jones, D., 1990, MNRAS, 246, 637

Gawryszczak,A., Rozyczka,M., 2003, Acta Astronomica, 53, 73

Gänsicke, B. et al., 1998, A&A, 338, 933

Gänsicke, B. et al., 2000, A&A, 356, L79

Giclas, H., Burnham, R., Thomas, N., 1970, Lowell Obs. Bull. 153

Godon, P., Livio, M., Lubow, S., 1998, MNRAS, 295, L11

Greenstein, J., Giclas, H., 1978, PASP, 90, 460

Greenstein, J., Kraft, R., 1959, ApJ, 130, 99

Groot, P., 2001, ApJ, 551, L89

Hagen, H. et al., 1995, A&AS, 111, 195

Harlaftis, E., 1999, A&A, 346, L73

Hellier, C., 2001, Cataclysmic Variable Stars. Praxis Pub. Ltd., Chichester.

Hessman, F., Hopp, U., 1990, A&A, 228, 387

Hirose,M., Osaki,Y., Mineshige,S., 1991, PASJ, 43, 809

Horne, K., Marsh, T., 1986, MNRAS, 218, 761

Horne, K., 1986, PASP, 98, 609

Howell, S., 2000, Handbook of CCD Astronomy. Cambridge Univ. Press, Cambridge.

Howell, S., Nelson, L., Rappaport, S., 2001, ApJ, 550, 897

Jedrzejewski, R., 1987, MNRAS, 226, 747

Kato, T., Ishioka,R., Uemura,M., PASJ, 54, 1023

Kent, S., 1983, MNRAS, 266, 562

King, A., Regev, O., Wynn, G., 1991, MNRAS, 251, 30

Kirkpatrick, J., McCarthy, D., 1994, AJ, 107, 333

Kunze, S., Speith, R., Hessman, F., 2001, MNRAS, 322, 499

Leggett, S., 1992, ApJS, 82, 351

Livio, M., Soker, N., Dgani, R., 1986, ApJ, 305, 267

Livio, M., Truran, J., 1992, ApJ, 389, 695

Long, K., Gilliland, R., 1999, ApJ, 511, 916

Lubow, S., 1989, ApJ, 340, 1064

Makita,M., Miyawaki,K., Matsuda,T., 2000, MNRAS 316, 906

Marsh, T., 1988, MNRAS, 231, 1117

Marsh, T., 1989, PASP, 101, 1032

Marsh, T., et al., 1990, ApJ, 364, 637

Marsh, T., Horne, K., 1988, MNRAS, 235, 269

Matsuda, T., et al., 2000, Ap&SS, 274, 259

Morales-Rueda, L. et al., 2000, MNRAS, 313, 454

Neustroev, V.V, Borisov, N.V., 1998, A&A, 336, L73

Ogilvie, G., 2002, MNRAS, 330, 937

Osaki, Y., 1996, PASP, 108, 39

Paczynski, B., 1977, ApJ, 216, 822

Putte, D., Smith, R., Hawkins, N., Martin, J., 2003, MNRAS, 342, 151

Ritter, H., Kolb, U., 1998, A&A Suppl., 129, 83

Schneider, D., Young, P., 1980, ApJ, 238, 946

Shafter, A., Szkody, P., Thorstensen, J., 1986, MNRAS, 308, 765

Shanno, D., Phua, K., 1980, ACM Tran. on Mathematical Software, 6, 618

Smak, J., 1981, Acta Astron., 31, 395

Smak, J., 2001, Acta Astron., 51, 279

Smak, J., 2001, Acta Astron., 51, 295

Smith, M., Dhillon, V., Marsh, T., 1998, MNRAS, 296, 465

Smith, M. et al., 1998, ApJ, 507, 94

Steeghs, D., Harlaftis, E., Horne, K., 1998, MNRAS, 296, 463

Steeghs, D., Horne, K., Marsh, T., Donati, J., 1996, MNRAS, 281, 626

Steeghs, D., Stehle, R., 1999, MNRAS, 307, 99

Stover, R, 1981, ApJ, 248, 684

Thorstensen, R., 2000, PASP, 112, 1269

Thorstensen, R. et al., 2002, PASP, 114, 1117

Wade, R. et al., 1981, ApJ, 246, 215

Warner, B., 1995, Cataclysmic Variable Stars. Cambridge Univ. Press, Cambridge.

Watson, C., Dhillon, V., Rutten, R., Shcwope, A., 2003, MNRAS, 341, 129

Welsh, R., Horne, K., Gomer, R., 1995, MNRAS, 275, 649

Wilson, R., 1953, Carnegie Inst. Washington D.C. Publ., 601.

Zhang, E., Robinson, E., 1987, ApJ, 321, 813